A Fresh Look at Classical Theory of Light with Applications to Quantum Interferometry

by

Simanraj Sadana

A thesis submitted to
Jawaharlal Nehru University
for the degree of
Doctor of Philosophy

Raman Research Institute, Bangalore

August, 2019.

Declaration

This thesis is a presentation of my original research work. Wherever contributions of others are involved, every effort is made to indicate this clearly, with due reference to the literature, and acknowledgement of collaborative research and discussions. The thesis has not been submitted for any other degree of this University or any other university. The work was done under the supervision of Professor Urbasi Sinha and co-supervision of Professor Barry C. Sanders, at the Raman Research Institute, Bangalore. This thesis has been passed through the *Turnitin* software to check for plagiarism.

Supervisor: Professor Urbasi Sinha

Light and Matter Physics,
Raman Research Institute,
Bangalore - 560080,

India.

Simanraj Sadana

Light and Matter Physics,
Raman Research Institute,
Bangalore - 560080,

India.

Certificate

This is to cerify that the thesis entitled "**A Fresh Look at Classical Theory of Light with Applications to Quantum Interferometry**" submitted by Simanraj Sadana for the award of the degree of Doctor of Philosophy from Jawaharlal Nehru University is his original work. This has not been published or submitted to any other University for any other degree or diploma.

Professor Ravi Subrahmanyam

(Center Chairperson)

Director
Raman Research Institute,
Bangalore - 560080,

India.

Professor Urbasi Sinha

(Thesis supervisor)

Light and Matter Physics,
Raman Research Institute,
Bangalore - 560080,

India.

Acknowledgements

I am grateful to my thesis supervisor Professor Urbasi Sinha and co-supervisor Professor Barry C. Sanders, for their guidance. I thank the members of my thesis advisory committee, Professor Aninda Sinha and Professor Gautam V. Soni, for being a constant source of encouragement. I am fortunate to have friends who not only gave me a home away from home but also kept me intellectually stimulated throughout my graduate studies. Lastly, and most importantly, I am indebted to my parents and brother for their unwavering belief in me and their constant support.

Contents

List of Figures

List of Tables

Synopsis

Aim and motivation

The status of quantum physics as the standard model for light and matter was consolidated when it explained all physical phenomena, known at the time of its formulation, which classical physics failed to aptly describe. Since then, its success has been undisputed. It has, with tremendous accuracy, described all the physical events in nature that are known to humans. This overwhelming triumph of quantum physics has overshadowed classical physics in the microscopic world.

This thesis is a step towards studying the application of classical physics to seemingly "quantum" effects. Such an endeavour, apart from testing the strength of classical theories, addresses a larger question that is gaining popularity in the physics community, that is

"Wherein lies the boundary between the classical and the quantum?"

A better answer to this question has applications beyond intellectual satiation. The field of quantum information and computing is rapidly growing owing to the predicted advantages it has over classical computation. However, it can't be asserted whether a quantum computer will have a significant advantage, partly because there may be a classical algorithm that we haven't found. Mostly, the confidence in a quantum algorithm comes from the fact that it uses one or more effects that are signatures of quantum behaviour and have no counterparts in the classical regime. Therefore, it is necessary to refine the boundary between classical and quantum behaviour.

Subjects of study

Hong-Ou-Mandel effect using classical pulses

The Hong-Ou-Mandel effect which is considered a signature of the quantum behaviour of light is described using the semi-classical theory of photo-detection. Briefly, when two indistinguishable photons are inputs of a 50:50 beam-splitter, the output is always a biphoton from one of the output ports. Such effect is considered to be a signature of the quantum behaviour of light. On the other hand, it has been always believed that if one uses the classical description of light, the predicted dip in the coincidence probability has an upper bound of 50%. It is demonstrated, in theory and experiment, that with proper phase control, the classical pulses can be setup to bring about a 100% dip in the coincidence probability. Furthermore, it is shown that the true signature of quantum behaviour is complementarity. While the photons show particle-like nature in one part of the experiment and behave wave-like in another part without any change in the source settings, the classical pulse fails to show both the behaviours. If the classical pulses are setup to show the 100% dip in coincidence probability (particle-like), it does not show interference (wave-like) and vice-versa.

Unitary description of diffraction

Unitary operators form the machinery of quantum information processing and computation. The rich unitary description of optical interferometers has catapulted them to become one of the most common platforms for quantum information implementation. One of the first interferometers is the double-slit setup. Using this simple setup, Young demonstrated the wave-like behaviour of light. On the other hand the double-slit setup was also used to demonstrate the wave-like nature of matter particles. Many variations of this experiment like “delayed choice” and “quantum eraser” have been used to study wave-particle duality and complementarity. Recently, a triple slit experiment has brought forward the naive application of the

superposition principle in quantum mechanics. Another work has demonstrated that a triple slit can be used to make spatially encoded qutrits. Therefore, there is no doubt that slit-diffraction is one of the simplest yet one of the most powerful experiments to test boundary between classical and quantum physics. However, although diffraction-based interferometry has been studied extensively using Maxwell's equation and even Feynman's path integrals, a unitary description of diffraction is not available. In this thesis, a post-selected unitary description of slit-diffraction is developed. Post-selection is important to take into account the losses that are intrinsic to slit-diffraction.

As a first step, it is shown that a double-slit setup can be used as a lossy beam-splitter. The reason to focus on a beam-splitter is that any N dimensional unitary operator can be realized in an optical experiment with the use of just beam-splitters and phase-shifters. All the calculations and simulations have been done using classical electromagnetic theory.

Methods

Hong-Ou-Mandel effect using classical pulses

According to the semi-classical theory of photo-detection the probability of coincidence is proportional to the cross-correlation of the integrated intensities falling on the two detectors. With no control over the relative phase of the input pulses, the phase is uniformly random over the interval $[0, 2\pi)$ as a result of which the upper of of 50% comes directly out of the semi-classical theory. However, it is noticed theoretically, that this upper-bound depends on the distribution over which the phase is randomized. Specifically, if the distribution is the sum of two Dirac-Delta functions $\frac{1}{2}\left(\delta(\varphi) + \delta(\varphi - \pi)\right)$, the upper-bound becomes 100%. For the experimental demonstration of this phenomenon, an electronic circuit is used instead of an optical one. This version of the experiment enables one to generate classical pulses with complete control over the relative phase hence over its distribution. A power-splitter

that functions as a 50:50 beam-splitter for electrical signals with frequency in the microwave range is used to create an interferometer. The cross-correlation of the outputs is then calculated to confirm that the dip in the coincidence probability is 100%.

For the complementarity part of the experiment, the output of the first power-splitter is passed through another 50:50 power-splitter (creating a Mach-Zehnder interferometer(MZI)), and the cross-correlation of the outputs is calculated for two cases. In one case, none of the arms of the MZI is blocked, and in the other, one of the arms is blocked. The results are compared with those of the standard quantum version of same experiment with optics using photons (with frequency in the infrared range) as inputs.

Unitary description of diffraction

To cast diffraction optics in framework of unitary transformation, the solutions of the time-independent wave equation, i.e., the Helmholtz equation are represented in terms of slice modes. A slice mode is a projection of an orthogonal mode of the 3 dimensional Helmholtz equation onto a sequence of 2 dimensional slices all parallel to each other. The propagation of these slices is captured through sequential mappings which depends on the Green's function of the Helmholtz equation with the chosen boundary conditions. Furthermore, diffraction is modelled as a transformation that a slice undergoes as it passes through slits. The transfer matrix for such a transformation is found. The entire process is depicted by a flow-chart that follows.

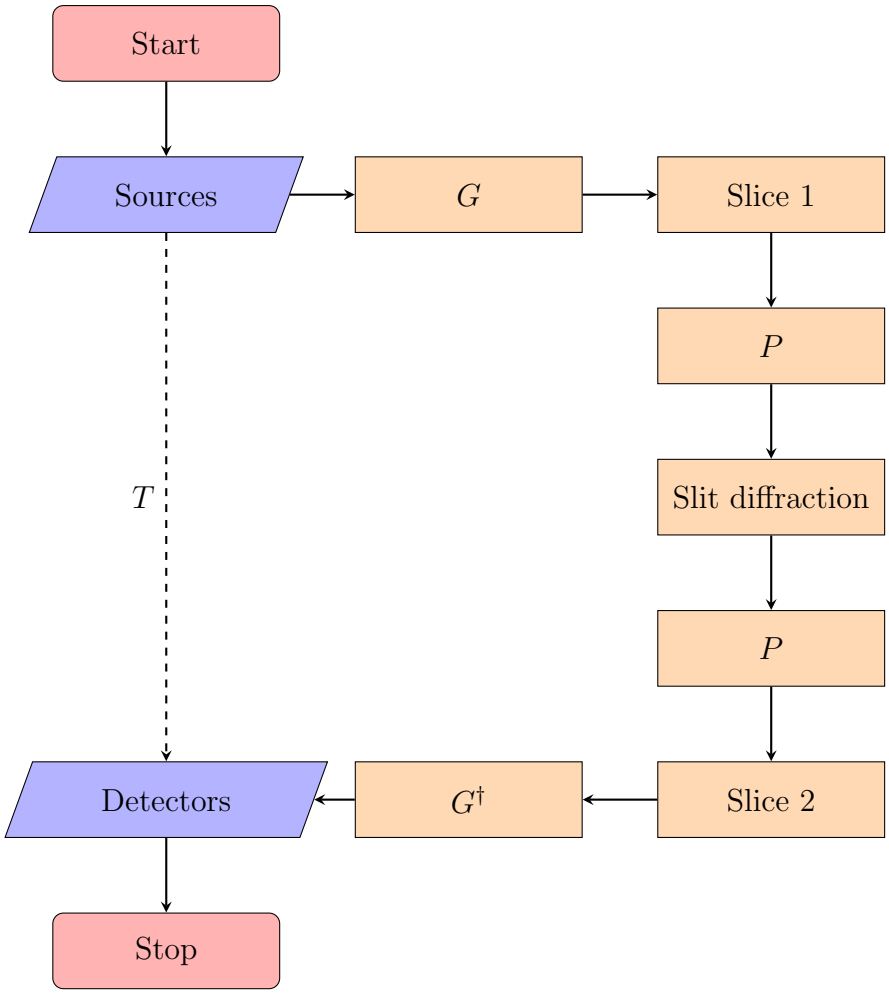

The solutions from N sources is projected onto the first slice using the Green's function G. This projection has an infinite dimensional vector representation. The propagator P which maps the solution between successive slices propagates the slice modes to the slits where they undergo diffraction. The propagator then maps the transformed slice modes onto the second slice. $G^{\dagger}$ then reverse propagates the projection on the second slice to the detectors where they are truncated from an infinite dimensional vector to N detector modes. The net transformation T has an $N \times N$ representation as a result of this truncation.

Since slit-diffraction has intrinsic losses, post-selection is employed to ignore the lossy part of the transfer matrix T. Mathematically, this process involves a singular-value-decomposition (SVD) which separates the unitary part of the transfer matrix from the lossy part, resulting in a post-selected unitary representation of slit-diffraction.

Importance and future research

This thesis is a step towards understanding how far classical description can take us, and where it hits a wall beyond which the quantum theory becomes indispensable.

List of Publications

1. S. Sadana, D. Ghosh, K. Joarder, A. N. Lakshmi, B. C. Sanders, and U. Sinha. Near-100% two-photon-like coincidence-visibility dip with classical light and the role of complementarity. *Phy. Rev. A*, 100(1):013839, 2019.

2. S. Sadana, B. C. Sanders, and U. Sinha. Double-slit interferometry as a lossy beam splitter. *arXiv preprint arXiv:1906.07450*, 2019.

Chapter 1

Introduction

This work aims to develop a framework in which slit diffraction can be represented using unitary operations on a Hilbert space. Specifically, we want a finite-dimensional discrete representation to express slit diffraction as a transfer matrix. The motivation is to use slit diffraction as a platform for linear optics quantum information processing. Linear optical quantum information processing (QIP) [1, 2] has a mathematical representation in the form of finite-dimensional unitary transfer matrices operating on a Hilbert space of vectors that represent qubits/qudits [3, 4]. The qubits are usually encoded in the polarization degree of freedom of a single photon, and optical components like beam splitters [5, 6, 7] and phase-shifters are used to implement the unitary transformations on them. For higher-dimensional QIP, systems such as orbital angular momentum [7, 8, 9, 10, 11] of photons are used. We map diffraction optics over a finite-dimensional unitary representation to connect it to qubit or qudit processing.

It has been shown that a triple slit system can be used to encode a qutrit [12, 13]. The novel interpretation of slit-diffraction that we present here sets the stage for extending the scope of application of diffraction interferometry to modern problems like higher-dimensional information processing. An example of alternative platforms that are used for higher-dimensional QIP in the optical regime is the orbital angular momentum of light in which information is encoded in the orbital angular momentum of light and manipulated [7]. But OAM based QIP is practically challenging and

poses problems like state preparation and state readability. Slit diffraction will be a more robust alternative to OAM based platforms as a diffraction interferometer has less moving components and can be miniaturized to construct sophisticated interferometers at small scales. Moreover, a finite-dimensional unitary description of diffraction also has applications in the field of matter-wave interferometry [14, 15, 16, 17, 18, 19].

The first step towards achieving this is to get the classical treatment right, and that is what we will do here. We have a plethora of literature on the classical treatment of diffraction, and we will use it to our advantage. However, to connect to the unitary representation of quantum gates, we need tools to test the diffraction-based gates. Linear quantum interferometers are characterized using one- and two-photon interference, i.e., single count and coincidence count [20]. We need the classical equivalent of such characterization tools and therefore require a bridge between the classical and the quantum.

The Hong-Ou-Mandel effect is one example of such a diagnostic [21]. We connect the coincidence probability of photons to the correlation of classical fields and show that a quantum phenomenon such as HOM can be simulated using classical light. Such a bridge between the classical and quantum gives us the necessary tool to test our slit diffraction interferometers to connect them with quantum gates.

1.1 Overview

We deal with the diffraction of classical fields and show a formalism in which slit-diffraction is represented as a finite-dimensional unitary transfer matrix [22] (in the postselected sense). We project the three-dimensional solutions of the Helmholtz equation [22, 23] on two-dimensional imaginary planes and call these projections slices. The propagation and diffraction of the fields are expressed as a slice-to-slice map as one goes from one slice to another from the sources to the detectors through the slits. By choosing an appropriate basis for the slices, we get an infinite-dimensional transfer matrix representation of such a map. Postselecting a finite

number of basis elements on the slices, reduces the transfer matrix to an effective finite-dimensional matrix. We show that such a truncated matrix is in general not unitary because of the losses in diffraction and that the polar decomposition [24] of the effective transfer matrix reveals the underlying unitary transfer matrix along with the lossy component.

Using the postselected unitary transfer matrix formalism of diffraction, we show that a customized double-slit setup is effectively a lossy beam splitter in the classical regime. A cubic beam splitter is a two-input-two-output optical device that has a 2×2 unitary transfer matrix that transforms the fields entering its input ports to the fields exiting its output ports [5, 6]. This 4-port device, along with phase shifters, serves as the building blocks of any N-channel interferometer [25, 26, 27, 28, 29]. The novelty and importance of our work lie in connecting one of the most elegant and fundamental experiments in scientific history, i.e., double-slit-diffraction with other types of interferometry which are used to solve some of the most critical problems in modern physics, like QIP.

To verify the beam splitter like behaviour of the double-slit setup, we compare the correlation of the classical outputs with that of the cubic beam splitter. We connect the classical correlation of the classical fields with the probability of photon coincidence counts through the semiclassical theory of photoelectric detection. As a part of that, we also show that the Hong-Ou-Mandel effect, which is considered to be a signature of the quantum behaviour of light, can be simulated using the classical description of light. Moreover, we show that it is the wave-particle complementarity that is the actual boundary between the classical and quantum behaviour of light. The connection between the classical and quantum correlations gives us the necessary tool to test our slit diffraction interferometers to connect them with quantum gates. We then verify the beam splitter further by concatenating two double-slit based beam splitters and adding a phase-shifter to construct an effective Mach-Zehnder interferometer [30].

The two-dimensional transfer matrix representation of double-slit-diffraction val-

idates the formalism and allows us to extend to a higher-dimensional system and find a transfer matrix representation for the same. Here we show such an application by finding the transfer matrix for a triple-slit system, demonstrating the way to extend the formalism from two slits to a higher number of slits.

Chapter 2

Background

We now discuss the relevant background concepts for the formalism that is presented in this work. The key ingredients of a unitary description include

- A Hilbert space: The Helmholtz equation, is a self-adjoint linear differential equation. Therefore, the solutions of the Helmholtz equation form a Hilbert space. The inner product in this Hilbert space is the spatial overlap between the two functions. In this chapter, we discuss the Helmholtz equation and its formal solution in terms of its Green's function [22, 23, 31]. Specifically, we discuss the application of the far-field and small-slit approximations to the solution of the Helmholtz equation for slit diffraction.

- A propagator that maps between different elements in the Hilbert space. Such a propagator comes out naturally in terms of the Green's function.

- A basis for the Hilbert space. The natural choice for a basis in this situation seems to be the eigensolutions of the Helmholtz equation which form a complete orthonormal basis for the Hilbert space of solutions of the Helmholtz equation. However, the eigenfunctions of the Helmholtz equation do not have compact support over finite intervals. On the other hand, detectors have finite-sized windows. Therefore, we need a basis of functions with compact support over the window of the detector. For this, we discuss *wavelets* which are functions with compact support and can be translated and dilated to make an

orthonormal set of functions [32, 33].

- A transfer matrix representation of the propagator in the chosen basis. In this chapter, I discuss the transfer matrix for a beam splitter as an example. A beam splitter is one of the fundamental components in optical interferometry. Moreover, any unitary operator can be realized using beam splitters and phase shifters.

2.1 The Helmholtz equation

In the classical regime, light is represented as continuous spacetime fields which are solutions to the Maxwell's equations. In this thesis, the electric field is always linearly polarized and therefore, the scalar version of the wave equation is sufficient. In free space, the four Maxwell's equations combine to yield the wave equation

$$\left(\nabla^2 - \frac{1}{c^2}\partial_t^2\right) E(\boldsymbol{r}, t) = \rho(\boldsymbol{r}, t) \tag{2.1}$$

where E (linearly polarized and hence represented by a scalar) is the electric field (or any field that satisfies the wave equation) and ρ is a source term [22, 23, 31].

Specifically, if the time-dependence of the source is like that of a simple-harmonic motion, the time-dependence of the field is also simple-harmonic. The harmonic time-dependence is a good approximation for many sources which produce light by the oscillation of charges. In this case, the wave equation reduces to a time-independent equation

$$\left(\nabla^2 - \frac{1}{c^2}\partial_t^2\right) E(\boldsymbol{r})\ \mathrm{e}^{-\mathrm{i}\omega t} = \rho(\boldsymbol{r})\ \mathrm{e}^{-\mathrm{i}\omega t}, \tag{2.2}$$

$$\implies \quad \left(\nabla^2 + \frac{\omega^2}{c^2}\right) E(\boldsymbol{r}) = \rho(\boldsymbol{r}), \tag{2.3}$$

where ω is the angular frequency of the oscillation. For brevity, it is customary to

define

$$k^2 = \frac{\omega^2}{c^2}, \tag{2.4}$$

reducing the Helmholtz equation to

$$\left(\nabla^2 + k^2\right) E(\boldsymbol{r}) = \rho(\boldsymbol{r}), \tag{2.5}$$

which is referred to as the Helmholtz equation.

The Helmholtz equation is a second-order partial differential equation. The complete formal solution of the equation requires the boundary conditions to be specified. Let us consider a volume $\mathcal{V}$ enclosed by a surface $\partial\mathcal{V}$ as shown in figure 2.1, in which I choose a connected region for simplicity. Within $\mathcal{V}$, there is a source $\rho(\boldsymbol{r}')$, and we want the field at any point $\boldsymbol{r}$ within the volume but outside the region occupied by the source. This is easily done by finding the Green's function of the Helmholtz equation.

Let $G(\boldsymbol{r}, \boldsymbol{r}')$ be the Green's function of the Helmholtz equation. Then

$$\left(\nabla'^2 + k^2\right) G(\boldsymbol{r}, \boldsymbol{r}') = \delta^3(\boldsymbol{r} - \boldsymbol{r}'), \tag{2.6}$$

where δ is Dirac-Delta function. On combining the Green's function equation with the Helmholtz equation we get

$$\begin{aligned} E(\boldsymbol{r}')\ \delta^3(\boldsymbol{r} - \boldsymbol{r}') &= G(\boldsymbol{r}, \boldsymbol{r}')\ \rho(\boldsymbol{r}') + E(\boldsymbol{r}')\ \nabla'^2 G(\boldsymbol{r}, \boldsymbol{r}') - G(\boldsymbol{r}, \boldsymbol{r}')\ \nabla'^2 E(\boldsymbol{r}') \\ &= G(\boldsymbol{r}, \boldsymbol{r}')\ \rho(\boldsymbol{r}') + \nabla' \cdot \left(E(\boldsymbol{r}')\ \nabla' G(\boldsymbol{r}, \boldsymbol{r}') - G(\boldsymbol{r}, \boldsymbol{r}')\ \nabla' E(\boldsymbol{r}')\right) \end{aligned} \tag{2.7}$$

On integrating both sides of the above equation over the volume $\mathcal{V}$, and by applying the Gauss's divergence theorem, we get

$$E(\boldsymbol{r}) = \iiint_{\mathcal{V}} \mathrm{d}^3\boldsymbol{r}'\ G(\boldsymbol{r}, \boldsymbol{r}')\ \rho(\boldsymbol{r}') + \iint_{\partial\mathcal{V}} \mathrm{d}^2\boldsymbol{r}'\ \hat{n}(\boldsymbol{r}') \cdot \left(E(\boldsymbol{r}')\ \nabla' G(\boldsymbol{r}, \boldsymbol{r}') - G(\boldsymbol{r}, \boldsymbol{r}')\ \nabla' E(\boldsymbol{r}')\right) \tag{2.8}$$

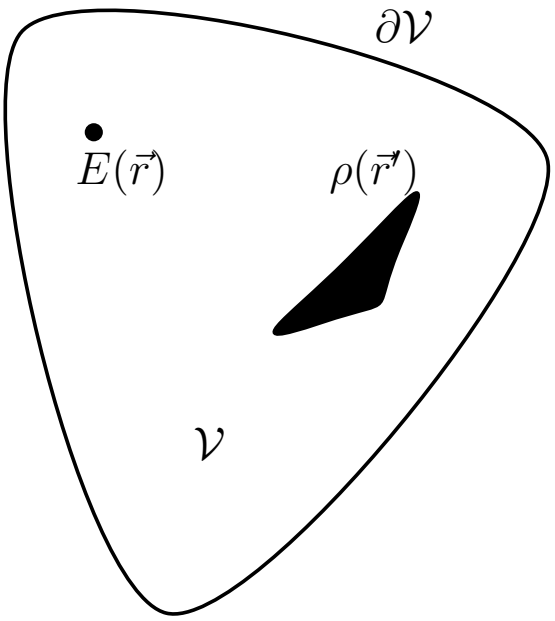

Figure 2.1: A source $\rho(\boldsymbol{r})$ in a volume $\mathcal{V}$ enclosed within the surface $\partial\mathcal{V}$. The field at point P at position $\boldsymbol{r}$ is $E(\boldsymbol{r})$.

where $\hat{n}(\boldsymbol{r}')$ is the unit normal to the surface. The right-hand-side (RHS) of Eq. (2.8) has a volume term and a surface term. The volume term is the contribution from the source and the surface term is the contribution from the boundary of the volume. The boundary condition is therefore important for the complete solution. The Green's function of the Helmholtz equation in free space is given by

$$G_{\text{ret}}(r) = \frac{1}{4\pi}\frac{\mathrm{e}^{\mathrm{i}|k|r}}{r}, \tag{2.9}$$

which is the retarded or forward propagating Green's function and

$$G_{\text{adv}}(r) = \frac{1}{4\pi}\frac{\mathrm{e}^{-\mathrm{i}|k|r}}{r}, \tag{2.10}$$

which is the advanced or backward propagating Green's function. The derivation of the Green's function of the Helmholtz equation is presented in Appendix A.

2.2 Hilbert space

Consider the homogeneous Helmholtz equation

$$\left(\nabla^2 + k^2\right) E(\boldsymbol{r}) = 0, \tag{2.11}$$

with respect to some boundary condition. If $E_1(\boldsymbol{r})$ and $E_2(\boldsymbol{r})$ are two distinct solutions of Eq. (2.11), then $E_1(\boldsymbol{r}) + E_2(\boldsymbol{r})$ is also a solution owing to the linearity of the equation. As Eq. (2.11) is a self-adjoint linear differential equation, all the solutions of the equation, with respect to the given boundary condition, form a Hilbert space with the inner product

$$\langle E_1, E_2 \rangle = \iiint_{\mathcal{V}} \mathrm{d}^3\boldsymbol{r}\ E_1^*(\boldsymbol{r}) E_2(\boldsymbol{r}). \tag{2.12}$$

The solutions of Eq. (2.11) are also called the *eigensolutions* of the Helmholtz equation, which form an orthonormal basis that spans the entire Hilbert space. Therefore, the particular solution of Eq. (2.5) can be expanded as a linear superposition of the eigensolutions of the Helmholtz equation.

Furthermore, consider a coordinate system in which the solution is separable in the transverse coordinate, say $\boldsymbol{r}_\perp$, and the longitudinal coordinate, say z, then the projections of the 3D solutions on a 2D surface $z = z_0$ also form a Hilbert space as they satisfy the equation

$$\left(\nabla_\perp^2 + \left(\partial_z^2\big|_{z_0} + k^2\right)\right) E(\boldsymbol{r}) = 0, \tag{2.13}$$

where the double derivative with respect to z is calculated at $z = z_0$. The inner product of the projected solutions is defined as

$$\langle E_1(z_0), E_2(z_0) \rangle \coloneqq \iint_{z=z_0} \mathrm{d}^2\boldsymbol{r}_\perp\ E_1^*(\boldsymbol{r}_\perp; z_0) E_2(\boldsymbol{r}_\perp; z_0), \tag{2.14}$$

where z_0 is now a parameter that denotes the surface under consideration.

One choice of basis for the Hilbert space on each slice is the set of the eigensolutions of Eq. (2.13). However, there is a practical problem with using such a basis. As, in practice, the detectors used in an experiment have finite-sized windows, it is suitable to choose a basis whose elements have a compact support over the window of the detector. The eigensolutions of the Helmholtz equation, in general, do not have this property as they have support over the entire 2D surface. This calls for choosing a different basis, the elements of which have compact support. In the next section, we discuss such functions, which could be used to construct a basis for the slices.

2.3 Wavelets

In simplest terms, wavelets are square-integrable functions with compact support over a finite interval. The concept of wavelets is much more intricate, powerful and detailed than what the above definition suggests. It is one of the most powerful tools in the field of signal processing. We discuss wavelets at a level that is sufficient to understand its application to the research presented in this thesis. A detailed study of the subject can be found in many books, examples of which are in the references [32, 33].

A simple example of wavelet is the Haar wavelet function defined as

$$\psi(x) := \begin{cases} 1 & 0 \leq x < 0.5 \\ -1 & 0.5 \leq x < 1 \\ 0 & \text{otherwise} \end{cases} \tag{2.15}$$

and shown in the Fig. 2.2 [34]. Unlike a sine function which extends to infinity on both sides, the above function is truncated over a finite interval. Other wavelets of the same type can be constructed by translating (moving) and dilating (stretching)

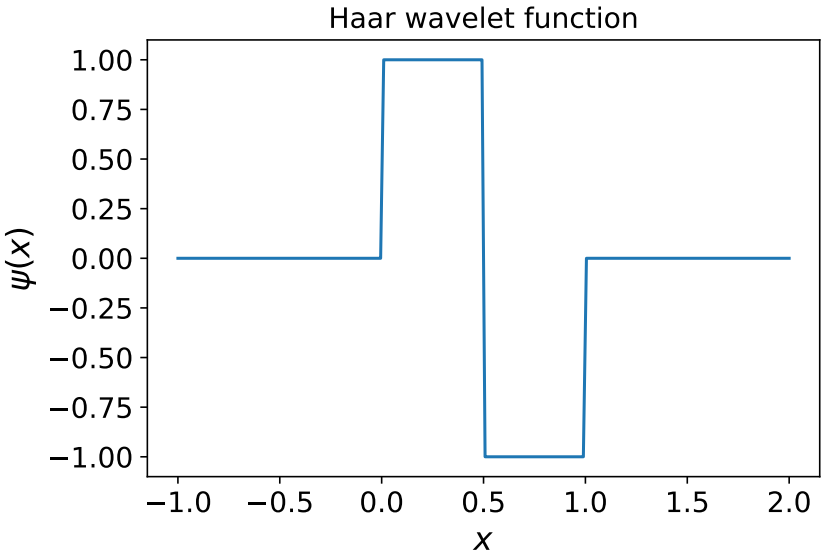

Figure 2.2: Haar wavelet function.

the above function. By translating and dilating $\psi(x)$, we get

$$\psi(x; a, b) = \frac{1}{\sqrt{a}}\,\psi\left(\frac{x-b}{a}\right) \tag{2.16}$$

where a is the factor by which the width of $\psi(x)$ is changed and b is the the displacement of $\psi(x)$. The factor $1/\sqrt{a}$ makes sure that the area under the curve is unchanged. Figures 2.3 and 2.4 show examples of translated and dilated Haar wavelets respectively.

2.3.1 Dyadic dilation and translation

It is customary in signal processing to dilate the wavelet function by powers of 2, i.e., $a = 2^{-m}$ for some integer m. The minus sign in the exponent is just a convention, which means that increasing the value of m shortens the extent of the wavelet function. Moreover, it is useful (as you will see shortly) to translated the wavelet function in steps of its width, i.e., $b = w2^{-m}n$, where w is the width of the generating wavelet function. With $w = 1$, the dyadically dilated and translated

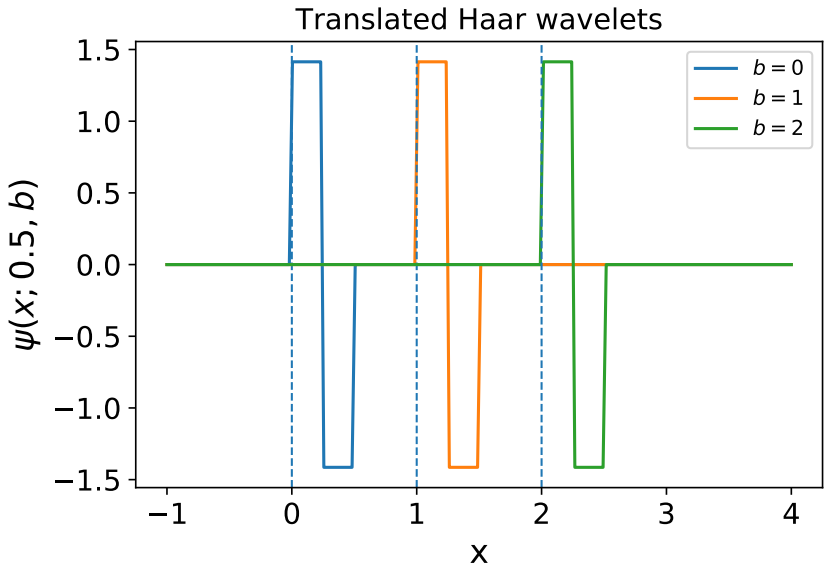

Figure 2.3: Haar wavelet with $a = 0.5$ (see Eq. (2.16)) and varying values of b which correspond to different amounts of translation.

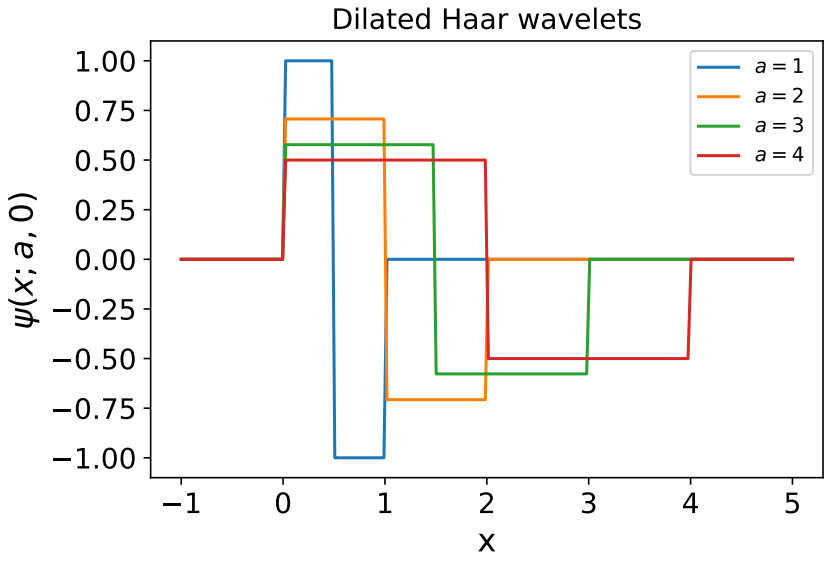

Figure 2.4: Haar wavelet with $b = 0$ (see Eq. (2.16)) and different values of a which correspond to different amounts of dilation.

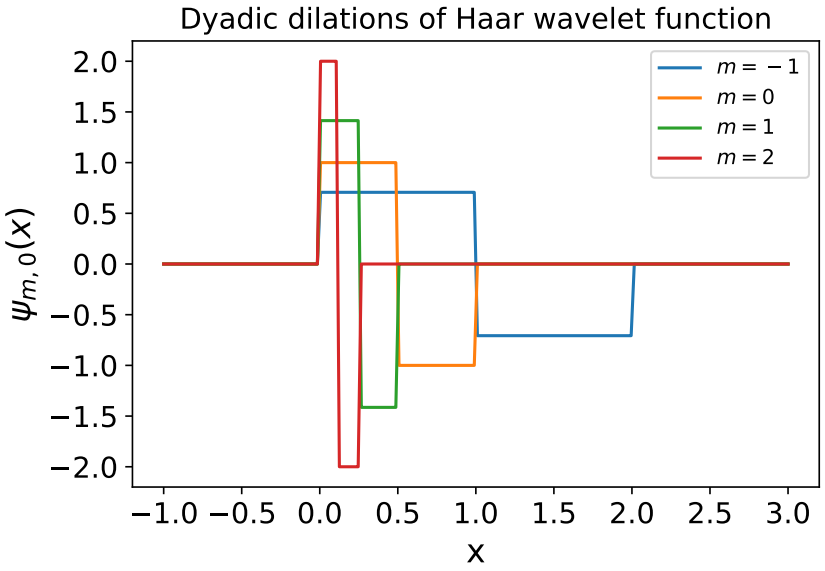

Figure 2.5: Wavelets with dyadic dilations. The value of n is set to zero while m is varied (see Eq. (2.17)).

wavelet function takes the form

$$\psi_{m,n}(x) := \frac{1}{\sqrt{2^{-m}}}\,\psi\left(\frac{x}{2^{-m}} - n\right) \qquad \forall m, n \in Z \tag{2.17}$$

where $\mathbb{Z}$ is the set of integers. Figure 2.5 shows only dyadic dilation of $\psi(x)$ and the following Fig. 2.6 shows the dyadic translation of the wavelet function with fixed m.

An advantage of dyadic dilation and translation of the Haar wavelet is that with respect to the inner product

$$\langle \psi_{m,n}, \psi_{m',n'} \rangle := \int_{-\infty}^{\infty} \mathrm{d}x\ \psi_{m,n}(x)\ \psi_{m',n'}(x) \tag{2.18}$$

it produces a set of orthonormal functions. If $m = m'$ and $n = n'$, the Haar wavelets are identical and completely overlapping with each other and therefore

$$\langle \psi_{m,n}, \psi_{m,n} \rangle = 1, \tag{2.19}$$

as $|\psi_{m,n}(x)|^2$ is a box with width 2^{-m} and height 2^m and therefore has area 1. Now let us consider the case in which $m = m'$ but $n \neq n'$. As discussed earlier, the

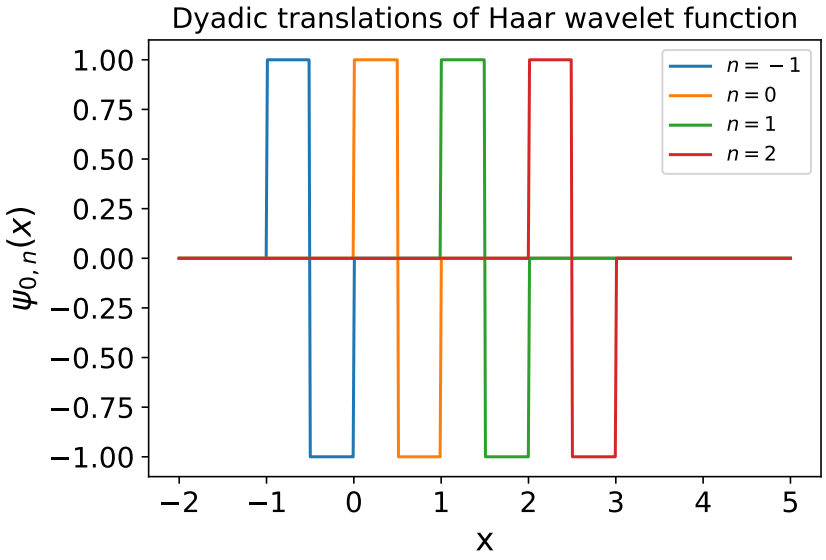

Figure 2.6: Wavelets translated in steps of their widths. The value of m is set to zero while n is varied (see Eq. (2.17)).

translation is always done in steps of the width of the Haar wavelet function, and the compact support of the wavelet ensures that there is no overlap between Haar wavelets translated with respect to each other (see Fig. 2.6). This implies that

$$\langle \psi_{m,n}, \psi_{m,n'} \rangle = \delta_{n,n'}, \tag{2.20}$$

where δ is Kroenecker delta. Now let us consider the case in which $n = n'$ but $m \neq m'$. First, note that the oscillatory nature of the Haar wavelet function leads to the fact that the area under the function is zero. Consequently, the area under a translated and/or dilated Haar wavelet is also zero. We show this formally for completeness. The area under the Haar wavelet function $\psi(x)$ is

$$\int_{-\infty}^{\infty} \mathrm{d}x\ \psi(x) = \int_{0}^{0.5} \mathrm{d}x\ 1 + \int_{0.5}^{1} \mathrm{d}x\ (-1) = 0 \tag{2.21}$$

which is easy to see from the definition of the Haar wavelet function. Now the area

under $\psi_{m,n}(x)$ is

$$\int_{-\infty}^{\infty} \mathrm{d}x\ \psi_{m,n}(x) = \int_{-\infty}^{\infty} \mathrm{d}x\ \frac{1}{\sqrt{2^{-m}}}\ \psi\left(\frac{x}{2^{-m}} - n\right), \tag{2.22}$$

where by subtituting

$$t = \frac{x}{2^{-m}} - n$$

we get

$$\int_{-\infty}^{\infty} \mathrm{d}x\ \psi_{m,n}(x) = \sqrt{2^{-m}} \int_{-\infty}^{\infty} \mathrm{d}t\ \psi\left(t\right) \tag{2.23}$$

$$= 0, \tag{2.24}$$

as the area under the Haar wavelet function is zero.

Now getting back to the case when $n = n'$ and $m \neq m'$. The compact support of $\psi_{m,n}(x)$ is the interval $[2^{-m}n, 2^{-m}(n+1))$. Now the inner product of two wavelets with different values of dilation parameter is

$$\langle \psi_{m,n}, \psi_{m',n} \rangle = \int_{-\infty}^{\infty} \mathrm{d}x\ \psi_{m,n}(x)\ \psi_{m',n}(x). \tag{2.25}$$

If $m' > m$, the range of the integration reduces to $\left[2^{-m'}n, 2^{-m'}(n+1)\right)$ and yields

$$\langle \psi_{m,n}, \psi_{m',n} \rangle = \int_{2^{-m'}n}^{2^{-m'}(n+1)} \mathrm{d}x\ \psi_{m,n}(x)\ \psi_{m',n}(x). \tag{2.26}$$

As we have assumed $m' > m$, $2^{-m'} < 2^{-m}$ and $2^{-m'}(n+1) \leq \frac{2^{-m}(n+1)}{2}$ which implies that

$$\left[2^{-m'}n, 2^{-m'}(n+1)\right) \subset \left[2^{-m}n, \frac{2^{-m}(n+1)}{2}\right), \tag{2.27}$$

and as $\psi_{m,n}(x)$ is constant over the interval $\left[2^{-m}n, \frac{2^{-m}(n+1)}{2}\right)$, the integral in Eq. (2.26)

becomes

$$\langle \psi_{m,n}, \psi_{m',n} \rangle = \pm \int_{2^{-m'}n}^{2^{-m'}(n+1)} \mathrm{d}x \ \psi_{m',n}(x) \tag{2.28}$$

$$= 0, \tag{2.29}$$

as we have shown that the area under a wavelet is zero. Combining Eqs. (2.19), (2.20) and (2.29), we get

$$\langle \psi_{m,n}, \psi_{m',n'} \rangle = \delta_{m,m'} \ \delta_{n,n'}, \tag{2.30}$$

hence proving that the dyadically translated and dilated Haar wavelets form a set of orthonormal functions. This set of orthonormal functions can be used to construct a basis for a function with support over a compact interval (or window). However, in general, an infinite number of wavelets are required to construct a given function. To circumvent this problem a bound must be set on the wavelets by using the scaling function.

2.3.2 Haar scaling function

Haar scaling function is defined as

$$\phi(x) := \begin{cases} 1 & 0 \leq x < 1 \\ 0 & \text{otherwise} \end{cases} \tag{2.31}$$

as shown in Fig. 2.7. The scaling function can also be translated and dilated to create a set of other functions, i.e.,

$$\phi_{j,k}(x) := \frac{1}{\sqrt{2^{-j}}} \ \psi\left(\frac{x}{2^{-j}} - k\right) \qquad \forall m, n \in Z. \tag{2.32}$$

Now at a particular value of j, say j_0, the translation of the scaling function yields a set of orthonormal functions as shown in Fig. 2.8. It is clear that there is no overlap

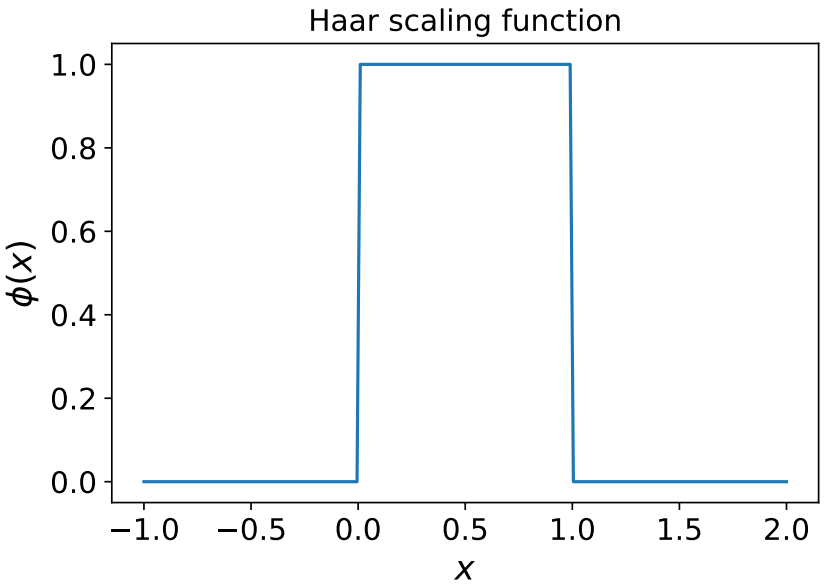

Figure 2.7: The Haar scaling function in one dimension.

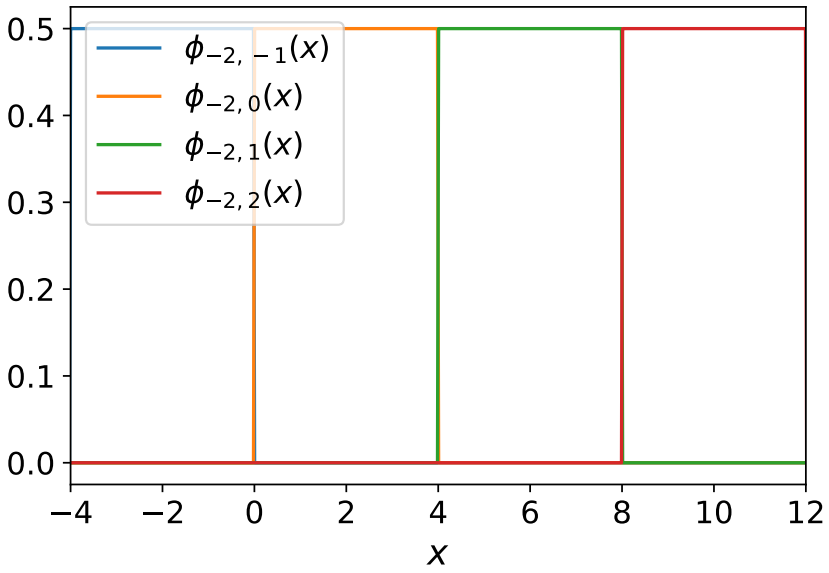

Figure 2.8: Scaling function translated in steps of its width. The value of j is set to -2 while k is varied (see Eq. (2.32)).

between the different translated scaling functions and therefore,

$$\langle \phi_{j_0,k}, \phi_{j_0,k'} \rangle = \delta_{k,k'} \tag{2.33}$$

for any fixed value of $j = j_0$. The Haar scaling function with a particular value of j along with the Haar wavelets can be used to reconstruct a function defined over a given interval.

2.3.3 Expanding a function using Haar wavelets

As an example, consider the function

$$f(x) = \sin(x) \tag{2.34}$$

defined over an interval, say $[0, 1)$. To reconstruct this function in terms of the Haar wavelets and scaling function, we fix $j = 0,\ k = 0$ so that the scaling function covers the entire interval. We label the chosen scaling function as

$$g_1(x) = \phi_{0,0}(x) \tag{2.35}$$

Along with the chosen scaling function, we choose all the Haar wavelets that have compact support within the interval $[0, 1)$. Such wavelets are

$$g_\imath(x) = \psi_{m,n}(x) \quad \forall\ m, n \in \mathbb{Z}, \tag{2.36}$$

where $\mathbb{Z}$ is the set of integers and $\imath$ is a meta-index for m and n which have the constraints

$$m \geq 0, \tag{2.37}$$

$$0 \leq n < 2^m, \tag{2.38}$$

which ensures that all the wavelets are within the chosen interval. The function $f(x)$ can be expanded as

$$f(x) = \langle \phi_{0,0}, f \rangle \, \phi_{0,0}(x) + \sum_{m>0} \sum_{n=0}^{2^m-1} \langle \psi_{m,n}, f \rangle \, \psi_{m,n}(x), \tag{2.39}$$

or in terms of the meta-index

$$f(x) = \sum_{i=0}^{\infty} \langle g_i, f \rangle \, g_i(x). \tag{2.40}$$

The accuracy of the expansion depends on the upper bound of m (see Fig. 2.9).

2.3.4 Wavelets in two-dimensions

Two-dimensional wavelets are just the tensor product of two wavelets in orthogonal coordinates. For example, if the orthogonal coordinates are the Cartesian x and y coordinates, then the two-dimensional wavelet in the xy plane is

$$\psi_{m,n,m',n'}(x, y) \coloneqq \psi_{m,n}(x)\psi_{m',n'}(y), \tag{2.41}$$

and similarly, the two-dimensional scaling function is

$$\phi_{j,k,j',k'}(x, y) \coloneqq \phi_{j,k}(x)\phi_{j'k'}(y). \tag{2.42}$$

In this work, we will project the 3D solutions of the Helmholtz equation on 2D planes, and the two-dimensional Haar wavelets will be used to make a postselected basis for the inputs and the outputs. In the next chapter, we discuss how to use the 2D wavelets to cast diffraction in the language of postselected unitary representations. In particular, we show that in this framework, a double-slit setup is an effective beam splitter in a postselected sense. In the following section, we briefly discuss the classical treatment of slit diffraction.

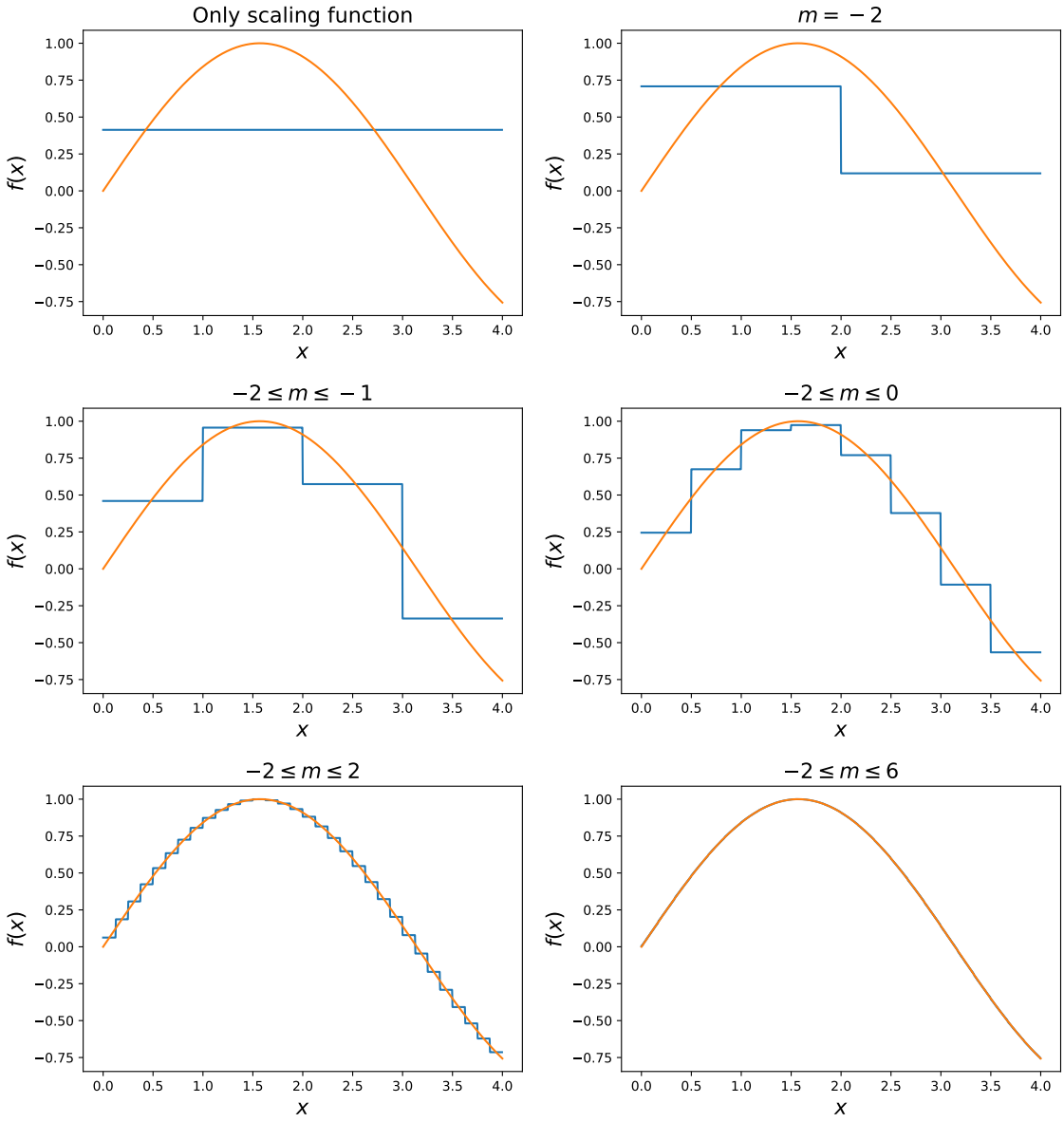

Figure 2.9: The accuracy of reconstruction of $f(x) = \sin(x)$ using the Haar wavelets and scaling function according to Eq. (2.39). The reconstruction is better with higher upper bound of m.

2.4 Slit diffraction

The formal solution of the Helmholtz equation is one of the ways in which the diffraction of light is explained (there are other methods like finite-difference-time-domain). The advantage of the Green's function method of finding the diffracted fields is that with some reasonable assumptions like far-field, the solution of the Helmholtz equation reduces to a straightforward expression. Specifically, for diffraction by a small slit, the far-field solution reduces to the mathematical representation of the well-known Huygen's principle [22].

Consider an opaque (infinite) plane with a rectangular aperture in it, placed at $z = z_s$ (see Fig. 2.10). Let the position of the center of the slit be $\boldsymbol{r}_s$ and its extent be w_x and w_y along the x and y axes respectively. All the other boundaries of the system are at infinity (for simplicity). A point-like source of electromagnetic radiation is placed at position $\boldsymbol{r}_f$. Assuming that the time-dependence of the source is harmonic, the field from the source will satisfy the Helmholtz equation (Eq. (2.5)). With far-field and small-slit approximations, the diffracted field is

$$\begin{aligned} E(\boldsymbol{r}) = &- \mathrm{i}kw_x w_y \left(\frac{z - z_s}{|\boldsymbol{r} - \boldsymbol{r}_s|} + \frac{z_s - z_f}{|\boldsymbol{r}_s - \boldsymbol{r}_f|} \right) G(\boldsymbol{r}, \boldsymbol{r}_s)\, G(\boldsymbol{r}_s, \boldsymbol{r}_f) \\ &\times \operatorname{sinc}\left(\frac{kw_x}{2} \left(\frac{\boldsymbol{r} - \boldsymbol{r}_s}{|\boldsymbol{r} - \boldsymbol{r}_s|} - \frac{\boldsymbol{r}_s - \boldsymbol{r}_f}{|\boldsymbol{r}_s - \boldsymbol{r}_f|} \right) \cdot \hat{\boldsymbol{x}} \right) \\ &\times \operatorname{sinc}\left(\frac{kw_y}{2} \left(\frac{\boldsymbol{r} - \boldsymbol{r}_s}{|\boldsymbol{r} - \boldsymbol{r}_s|} - \frac{\boldsymbol{r}_s - \boldsymbol{r}_f}{|\boldsymbol{r}_s - \boldsymbol{r}_f|} \right) \cdot \hat{\boldsymbol{y}} \right), \end{aligned} \tag{2.43}$$

which is the familiar sinc variation of light diffracted by a rectangular slit. The detailed calculations are shown in Appendix B. In this thesis, we use Eq. (2.43) to calculate the fields diffracted by slits in the far-field regime.

As we want to connect slit diffraction interferometry with the unitary description of multi-beam optical interferometry, it is important to discuss a key optical device called the beam splitter and its versatility in the experimental implementation of unitary operations.

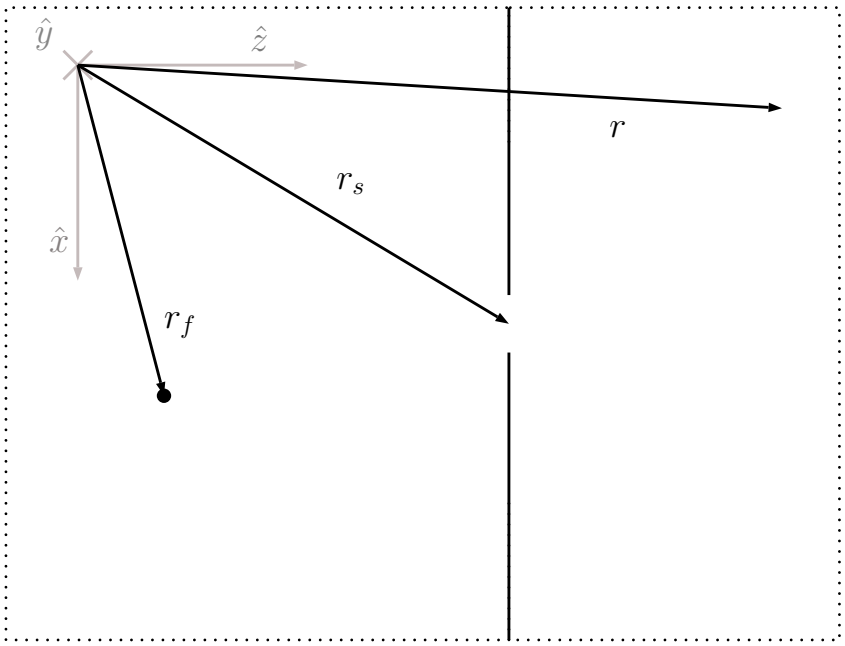

Figure 2.10: The schematic of single slit diffraction of light from a point-like source. The dotted line represents the fact that the boundary of the system is at infinity. A point-like source of monochromatic light is placed at $\boldsymbol{r}_f$. The light emanating from it is diffracted by a slit whose center is at $\boldsymbol{r}_s$. The position $\boldsymbol{r}$ is where the field is measured.

2.5 Beam splitter and its transfer matrix

A beam-splitter is a ubiquitous two-input-two-output component in interferometry. The importance of beam splitter is a result of the fact that any N-dimensional unitary operator can be decomposed into beam splitter operations and phase shifter operations [28, 29]. An example schematic of such a decomposition, with $N = 4$ is shown in Fig. 2.11. In optics, a beam splitter is commonly in the form of a glass cube, half-silvered mirror or fibre-based, which have two input and two output modes corresponding to each of their ports. In a 50:50 cubic beam splitter, for example, the modes are the k-vectors corresponding to the plane wave entering each of its ports, forming a basis to represent the inputs and outputs as two-dimensional column vectors in a Hilbert space. In such a representation, the beam splitter

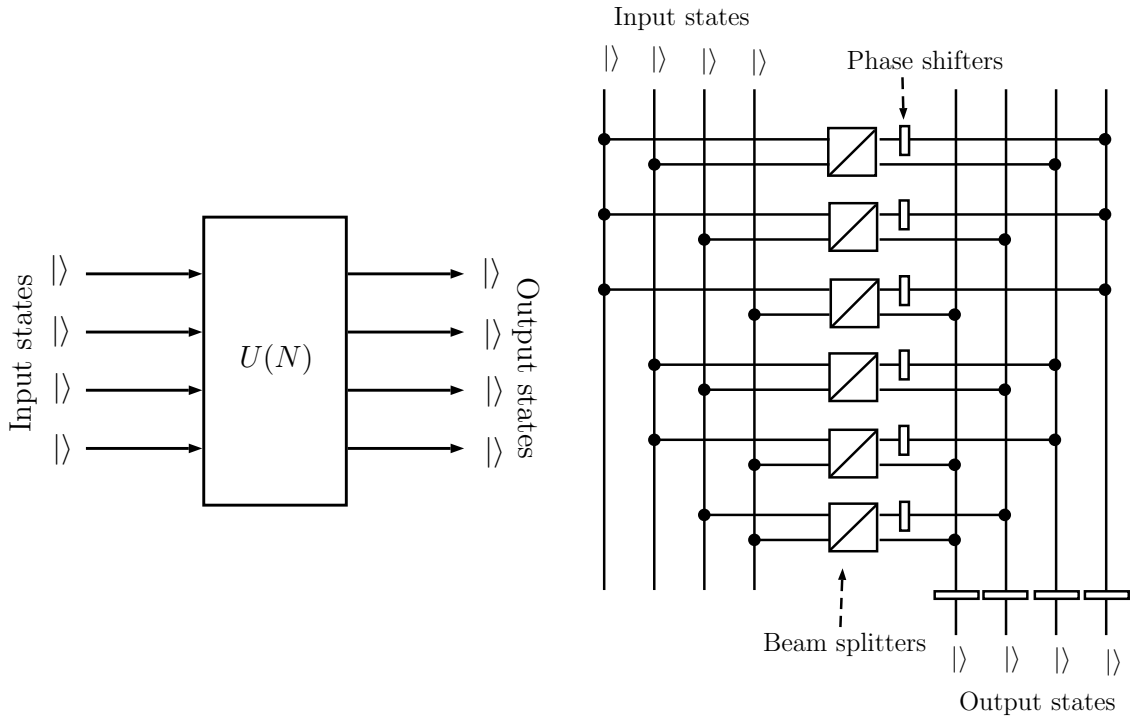

Figure 2.11: An example of how an N-dimensional ($N = 4$ here) unitary operator can be constructed using beam splitters and phase shifters in general.

transformation has a two-dimensional transfer matrix representation [5, 6, 35],

$$U_{\mathrm{BS}} = \frac{1}{\sqrt{2}} \begin{pmatrix} 1 & \mathrm{i} \\ \mathrm{i} & 1 \end{pmatrix}, \tag{2.44}$$

where each row corresponds to the superposition of the two input modes to form the outputs, and complex elements of the matrix denote the phase-shift introduced in each input. The transformation in Eq. (2.44) is that for a cubic beam splitter like that shown in Fig. 2.12. Another example of a beam splitter matrix is

$$U_{\mathrm{BS}} = \frac{1}{\sqrt{2}} \begin{pmatrix} 1 & 1 \\ 1 & -1 \end{pmatrix}, \tag{2.45}$$

also known as the Hadamard gate in quantum information. A half-silvered mirror beam splitter (see Fig. 2.13) has such a transfer matrix.

In general, if the source of light does not emit in a single mode (say, a diver-

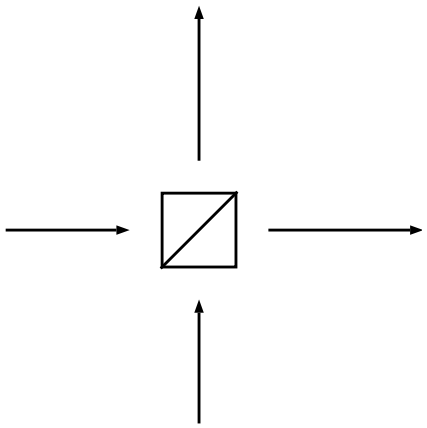

Figure 2.12: A cubic beam splitter.

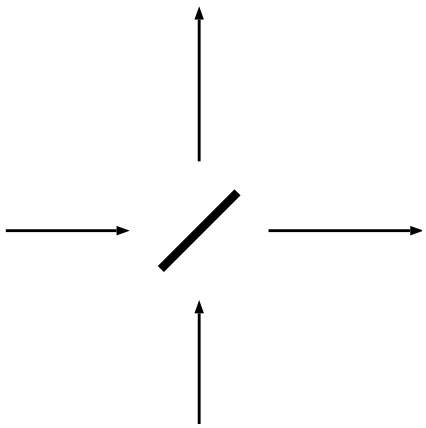

Figure 2.13: A half-silvered mirror as a beam splitter.

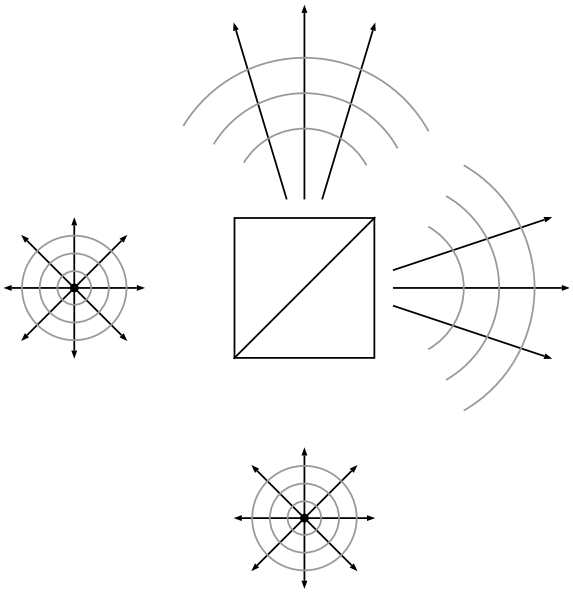

Figure 2.14: A beam splitter setup with source emitting multiple modes, in this case, infinitely many plane wave modes. In such a case the beam splitter transformation has an infinite-dimensional transfer matrix representation. In order to truncate the transfer matrix to a 2-dimensional matrix, two input and two output modes must be post-selected. For example if the selected modes are those corresponding to normally incident input and output modes, the 2×2 transfer matrix is as in Eq. (2.44).

gent beam), the vector representation of the inputs and outputs can be infinite-dimensional, yielding an infinite-dimensional transfer matrix of the beam splitter. In such a case, two suitable input and two output modes can be post-selected to reduce the infinite-dimensional transfer matrix to a postselected 2×2 transfer matrix as in Eq. (2.44). In practice, this postselection is achieved by collimating the input beams of the beam splitter. But as collimation is not perfect, leaving the beam slightly divergent, the 2×2 matrix is only an approximate representation of the beam splitter transformation.

A consequence of the beam splitter transformation is that the outputs of the beam splitter are correlated. Such a correlation manifests as the Hong-Ou-Mandel effect as a result of two-photon interference.

2.6 Hong-Ou-Mandel effect

The Hong-Ou-Mandel [21] effect is a result of two-photon interference between single photons passing through a beam splitter, one entering each port of the beam splitter as shown in Fig. 2.15. Let us say that the two photons are in modes $\boldsymbol{k}_1$ and $\boldsymbol{k}_2$, one for each input port of the beam splitter. If the two input photons arrive at their respective ports at the same time, the input state of the system can be represented as a vector in a Hilbert space as

$$|\psi\rangle_{\text{in}} = \hat{a}_1^\dagger \, \hat{a}_2^\dagger \, |0\rangle_1 |0\rangle_2 \tag{2.46}$$

where $\hat{a}_1^\dagger$ is the creation operator for a photon in mode $\boldsymbol{k}_1$ and $\hat{a}_2^\dagger$ is that for mode $\boldsymbol{k}_2$. After passing through a 50:50 beam splitter, the state transforms as

$$|\psi\rangle_{\text{out}} = \left(\frac{\hat{a}_1^\dagger + \mathrm{i}\hat{a}_2^\dagger}{\sqrt{2}} \right) \left(\frac{\hat{a}_1^\dagger - \mathrm{i}\hat{a}_2^\dagger}{\sqrt{2}} \right) |0\rangle_1 |0\rangle_2 \,, \tag{2.47}$$

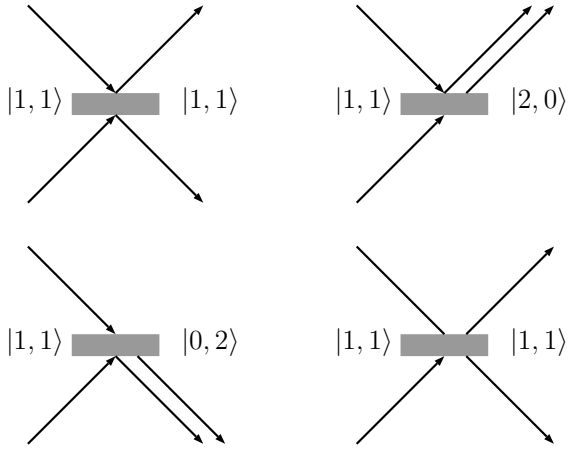

Figure 2.15: Schematic of the Hong-Ou-Mandel effect. The rectangular blocks represent 50:50 beam splitters and the arrows represent the input and output photons. The figure shows the four possible outputs of the beam splitter when two indistinguishable photons enter the beam splitter. The HOM effect is the non-occurrance of the top-left and bottom-right cases due to two-photon interference.

and as $\left[\hat{a}_1^\dagger, \hat{a}_2^\dagger\right] = 0$, the final state reduces to

$$|\psi\rangle_{\text{out}} = \frac{\left(\hat{a}_1^\dagger\right)^2 + \left(\hat{a}_2^\dagger\right)^2}{2} |0\rangle_1 |0\rangle_2 \tag{2.48}$$

$$= \frac{|2\rangle_1 |0\rangle_2 + |0\rangle_1 |2\rangle_2}{\sqrt{2}}. \tag{2.49}$$

Therefore, due to the two-photon interference both the photons exit the same output port of the beam splitter, and the probability of one photon exiting each port is zero, resulting in zero chance of coincident detection of photons at the two detectors placed at the output ports. This bunching of photons is call the Hong-Ou-Mandel effect and it is considered one of the signatures of the quantum nature of light.

If there is a time-delay between the incident input photons, the probability of coincident photodetection is shows a 100% dip as the time-delay approaches zero, making the two input photons indistinguishable from each other.

The accurate characterization of linear optical interferometers requires the measurement of one- and two-photon interference [20]. As we cast slit diffraction in the language of linear optical interferometers using a unitary representation, we need these testbeds to verify the diffraction interferometers. However, as we use classical

treatment for slit diffraction in this work, we need a bridge between the classical description of light and photodetection. This bridge is provided by the semiclassical theory of photoelectric detection.

2.7 Semi-classical theory of photoelectric detection

In the semiclassical theory of photoelectric detection [36, 37, 38], the process of the photoelectric effect is explained by treating light as a classical electromagnetic field whereas treating the surface, from which the photoelectrons eject upon illumination, as composed of quantum systems. It is claimed that the output of the photoelectric detector is a manifestation of the fluctuations in the light falling on it, in such a way that the probability of photo-emission is proportional to the instantaneous intensity of the light.

Building upon that line of reasoning, it was also shown that the correlation between the photo-detections at two detectors placed at different locations can be explained by the "fourth-order interference" (or intensity-intensity correlation) between the classical light falling on these detectors. In particular, if $I(\boldsymbol{r}_1, t_1)$ and $I(\boldsymbol{r}_2, t_2)$ are the intensities intercepted by two detectors at positions $\boldsymbol{r}_1$ and $\boldsymbol{r}_2$, at times t_1 and t_2 respectively, the probability of coincident photoelectric detections is given by

$$P(\boldsymbol{r}_1, t_1, \boldsymbol{r}_2, t_2) = \eta_1 \eta_2 \left\langle I(\boldsymbol{r}_1, t_1) I(\boldsymbol{r}_2, t_2) \right\rangle \Delta t_1 \Delta t_2 \tag{2.50}$$

where Δt_1 (Δt_2) is centered around t_1 (t_2). The angled brackets denote the ensemble average over the flucutations in the light and η_1 (η_2) is the efficiency of detector 1

(detector 2). If T is the acquisition time of the detector then

$$P(\boldsymbol{r}_1, t_1, \boldsymbol{r}_2, t_2) = \eta_1 \eta_2 \left\langle \int_{t_1 - T/2}^{t_1 + T/2} \mathrm{d}t \; I(\boldsymbol{r}_1, t) \int_{t_2 - T/2}^{t_2 + T/2} \mathrm{d}t' \; I(\boldsymbol{r}_2, t') \right\rangle \tag{2.51}$$

therefore, relating the probability of multi-photodetections on distinct detectors to the intensity-intensity correlation of the classical light.

However, the derived correlation formula did not explain the Hong-Ou-Mandel effect. According to the semiclassical theory, the coincidence probability drops only by 50%, as opposed to the 100% dip, which is observed in experiments. This led to the widespread belief that the HOM effect is a signature of the quantum nature of light and that no semiclassical theory can explain it. In this work, we will show that the HOM effect can indeed be simulated using the classical description of light. This helps us connect the classical treatment of slit diffraction with the unitary description of quantum gates.

Chapter 3

Unitary Description of Diffraction

In this chapter, we build the framework in which slit diffraction is cast as unitary transformations on a Hilbert space. By using double-slit diffraction as an example, we show that a double slit is effectively a beam splitter acting on an appropriate Hilbert space. In this scheme, the 3-dimensional solution of the Helmholtz equation is projected on to 2-dimensional surfaces all parallel to one another. We refer to these projections as *slices* of the field. Using the formal solution of the Helmholtz equation, we find a propagator that maps one slice to another. Diffraction is then expressed as a transformation of the slice by the slit(s) [39].

The aim is to represent the slice-to-slice map as a transformation on vectors in a Hilbert space. As the Helmholtz equation is a self-adjoint linear partial differential equation, its solutions are vectors in a Hilbert space, say $\mathbb{H}$. As a corollary, each slice is also a vector in a subspace of $\mathbb{H}$. With an appropriate basis on each slice, the slice-to-slice propagator has a transfer matrix representation. In general, the said Hilbert space is infinite-dimensional yielding an infinite-dimensional transfer matrix representation of diffraction. With the use of postselection (see the discussion of such a postselection for a beam splitter in §2.5) the transfer matrix is truncated to be finite-dimensional.

For double-slit setup, with which we work here, we get a postselected 2-dimensional transfer matrix. However, in general, such a transfer matrix is not unitary because of the losses incurred by the diffracting fields. In such cases, we carry out a polar

decomposition [40] of the transfer matrix to reveal the underlying unitary transformation. The Hermitian component of the polar decomposed transfer matrix captures the losses in the system. The unitary component of the transfer matrix comes out close to that for a beam splitter.

To verify the beam splitter behaviour of the double-slit setup, we calculate the intensity-intensity correlation of the outputs and compare it with that for a beam splitter. Moreover, we also construct a Mach-Zehnder interferometer using such double-slit setups as beam splitters to show the effectiveness of the beam splitter. The double-slit setup, as an example, set the stage for extending the framework to systems with a higher number of slits. As an example of that, we apply the framework to a triple slit setup and find its postselected unitary transfer matrix.

In §3.1, we discuss how the formal solution of the Helmholtz equation is used to get the slice-to-slice map. In §3.2, we describe the double-slit setup using which we will describe the framework for a postselected unitary representation of slit-diffraction. In §3.3, we discuss how to construct an appropriate basis for a slice using Haar wavelets. From the set of infinite Haar wavelets that will span a slice, we will postselect two as input modes and two as output modes. With the postselected input and output modes we get an effective 2×2 transfer matrix for slit-diffraction in §3.4. In chapter 5, we verify the double slit as an effective beam splitter by studying the intensity-intensity correlation of its outputs, and by concatenating two such double-slit setups to construct an effective Mach-Zehnder interferometer. The final section of this chapter, i.e., §5.3, we extend the framework to find the transfer matrix for a triple slit. All the results of this work are numerically solved.

3.1 Slice-to-slice map

If one does not have any information about the source of the field but knows the field on a surface, is it possible for the observer to get the value of the field at other points? Consider a source $\rho(\boldsymbol{r})$ that emits radiation with harmonic time-dependence, as shown in the Fig. 3.1. The dotted boundary denotes boundaries

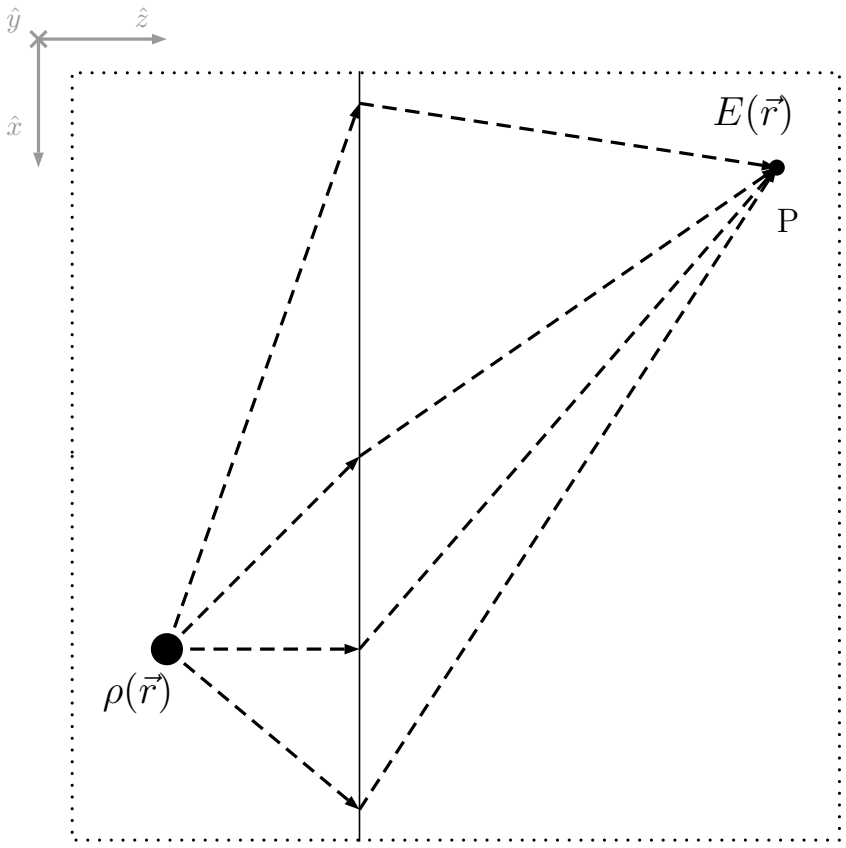

Figure 3.1: An example of calculating the field from the field on a slice. The dotted lines of the boundary denote that the boundary is infinitely far from the points of interest. The observer at point P does not have any information about the source but only knows the field on the given slice. The field on the slice is from the source ρ, and the surface term of the formal solution of the Helmholtz equation Eq. (2.8) can be used to calculate the field at point P.

at infinity (or very far away from the points of interest). The solid line represents a two-dimensional infinite plane on which the field is projected. The observer at point P does not have any information about the nature of the source term ρ but knows the field on the two-dimensional surface. Henceforth, the projection of the three-dimensional field on a two-dimensional surface is called a *slice* of the field. The field at P can be calculated from the field at the surface alone.

The field on any point on the chosen plane can be calculated using the volume term of the formal solution of Helmholtz equation. The surface term does not any

point $\boldsymbol{r}$ on the plane is

$$E_s(\boldsymbol{r}) = \iiint_{\mathcal{V}} \mathrm{d}^3\boldsymbol{r}' \; G(\boldsymbol{r}, \boldsymbol{r}') \; \rho(\boldsymbol{r}') \tag{3.1}$$

the field at point P is from the slice, i.e.,

$$E(\boldsymbol{r}) = \iint_{s} \mathrm{d}^2\boldsymbol{r}' \; \hat{n}(\boldsymbol{r}') \cdot (E(\boldsymbol{r}') \; \nabla' G(\boldsymbol{r}, \boldsymbol{r}') - G(\boldsymbol{r}, \boldsymbol{r}') \; \nabla' E(\boldsymbol{r}')) \tag{3.2}$$

3.2 The double-slit setup

We elaborate on the slice modes concept using a customized double-slit setup with two sources and two detectors as shown in Fig. 3.2, where $\hat{\boldsymbol{y}}$ extends into the plane of the paper. The slits are parallel to the xy plane, and so are the sources and the detectors at different values of z. The width of the apertures and other distances are chosen such that far-field approximations can be applied to solutions of the Helmholtz equation. A perfectly absorbing barrier is added that runs along the z direction and separates a slit from the detector across the barrier. The purpose of the barrier is to prevent the high diffraction orders [22] from reaching the detectors and also to isolate one detector from another to avoid an overlap of fields between the two.

3.2.1 Sources

The sources S_1 and S_2 are monochromatic point-like sources (practically a spherical source with diameter $\sim \lambda$) emanating linearly polarized light as spherical waves ($Y_0^0(\theta, \phi)$ spherical harmonic [23]) with wavelength λ. They are placed at

$$\boldsymbol{r}_{\mathrm{S}_1} = (d/2, 0, -L)\,, \tag{3.3}$$

$$\boldsymbol{r}_{\mathrm{S}_2} = (-d/2, 0, -L)\,, \tag{3.4}$$

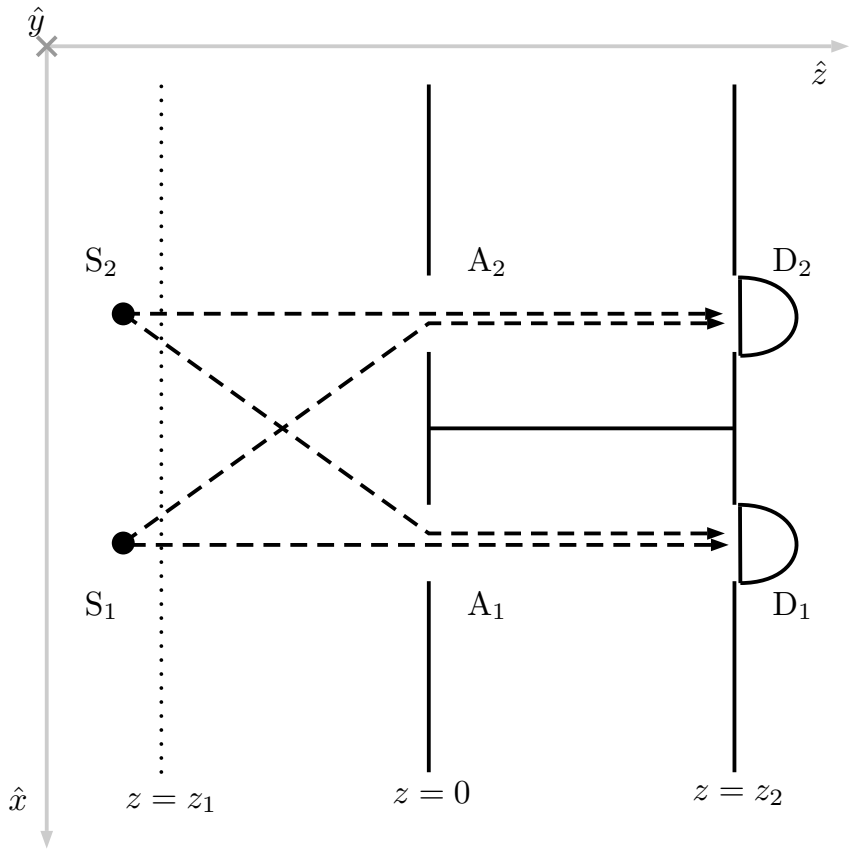

Figure 3.2: Schematic of the double-slit setup considered in this paper. Two point-like sources S_1 and S_2 emanate monochromatic linearly polarized light with harmonic time-dependence. The imaginary plane at $z = z_1$ (represented by a dotted line) is for the input slice. Two slits A_1 and A_2 are placed at $z = 0$ where each slit is aligned centre-to-centre with one of the sources. The second pair of slits D_1 and D_2 are placed at $z = z_2$ where each port is aligned centre-to-centre with one of the sources. Behind each of these slits is a square-faced detector which measures the integrated intensity of the light falling on it. The plane $z = z_2$ is also for projecting the output slice. A perfectly absorbing barrier runs between $z = 0$ and $z = z_2$ that prevents the field from slit A_1 (A_2) from reaching port D_2 (D_1). The dashed arrows represent the ray approximations of the fields from the sources to the detectors.

respectively, where

$$d = 20\lambda \tag{3.5}$$

is the distance between the two sources and

$$L = 800\lambda \tag{3.6}$$

is the distance between the sources and the slit plane along the z direction. Without loss of generality, we choose $\lambda = 1$.

In the far-field regime [22], these sources can be approximated by Dirac-delta functions $\delta^3(\boldsymbol{r} - \boldsymbol{r}_{\mathrm{S}_1})$ and $\delta^3(\boldsymbol{r} - \boldsymbol{r}_{\mathrm{S}_2})$. We multiply the source-term with a factor of 10^5 so that the simulation results do not suffer precision errors. As the sources are linearly polarized, the field from source S_i at points far from the slits, before diffraction, can be found by solving the Helmholtz equation for scalar fields and can be approximated by

$$E^{(i)}(\boldsymbol{r}) \approx G(\boldsymbol{r}, \boldsymbol{r}_{\mathrm{S}_i}), \tag{3.7}$$

where the use of the scalar equation is justified because the polarizations of field from both the sources are collinear. Note that the approximation in Eq. (3.7) is valid only because the slit plane is far enough from the plane at z_1, so that the surface-effects are negligible.

3.2.2 Slits

Two square-shaped slits A_1 and A_2, each with side-length

$$w = 4\lambda \tag{3.8}$$

are placed at $z = 0$ with the positions of their centers

$$\boldsymbol{r}_{\mathrm{A}_1} = (d/2, 0, 0)\,, \tag{3.9}$$

$$\boldsymbol{r}_{\mathrm{A}_2} = (-d/2, 0, 0)\,, \tag{3.10}$$

respectively, and therefore aligned with the respective sources. In the Fraunhofer regime, the diffracted field $E_j^{(i)}(\boldsymbol{r})$ from source S_i through slit A_j, is calculated by simplifying the surface term in Eq. (2.8) by applying the appropriate approximations (see appendix B). Note that, due to the opaque barrier between the two detectors, detector port D_k is blocked from the field $E_j^{(i)}(\boldsymbol{r})$ if $k \neq j$.

3.2.3 Detectors and slices

Another pair of square-shaped slits D_1 and D_2, aligned with A_1 and A_2 respectively, are placed at $z = L$, behind each of which is a square-law detector (that measures the integrated squared magnitude of fields) whose window is of the same shape and size as those of the slits. The detector is 100% efficient for the light of wavelength λ. The detectors could have been placed without the second pair of slits which play a role only when two such double-slit setups are concatenated to construct interferometers.

Two imaginary planes are at

$$z_1 = -\,0.9L, \tag{3.11}$$

$$z_2 = L, \tag{3.12}$$

on which the input and output slices are considered respectively, for the double-slit. The input slice is not placed at $-L$ where the sources are, as the solution of the Helmholtz equation diverges at the sources.

The Fraunhofer approximation can be applied to the fields in the double-slit described above if the Fresnel number of the system is much less than 0.1. For the

dimensions chosen, the Fresnel number is

$$F = \frac{w^2}{L\lambda} = 0.02 \tag{3.13}$$

which justifies the use of Fraunhofer approximation. Moreover, as we seek a beam splitter matrix in Eq. (2.44), we have chosen the dimensions such that

$$\sqrt{L^2 + d^2} - L = (2q + 1)\frac{\pi}{2}, \ \forall \ q \in \mathbb{Z}, \tag{3.14}$$

such that the field from source S_1 (S_2) acquires a phase of an odd multiple of $\pi/2$ with respect to the field from S_2 (S_1) as it reaches the slit A_2 (A_1). The transfer matrix of the double-slit diffraction is sensitive to the geometry and dimensions of the system. Here we have chosen the dimensions motivated by the form of the 50:50 beam splitter matrix as in Eq. (2.44), but other transfer matrices can be realized by choosing different geometries and dimensions.

Now we discuss how to choose a basis for the two slices, that we have placed in the system, using two-dimensional Haar wavelets. We will also discuss how to postselect wavelets for the two input and two output modes of the double-slit beam splitter.

3.3 The slice modes

The non-compact eigenfunctions of the Helmholtz equation do not make suitable modes for detectors with finite-sized windows. Haar functions (§2.3) on the other hand, have compact support over a given interval and therefore two-dimensional Haar functions make suitable modes for the square-shaped detector windows. The Haar wavelets and the Haar scaling functions, however, form an overcomplete set of orthonormal functions [32, 33].

To remove the redundancy, we divide each slice into non-overlapping square patches, each with side-length equal w, as shown in Fig. 3.3. The square patches

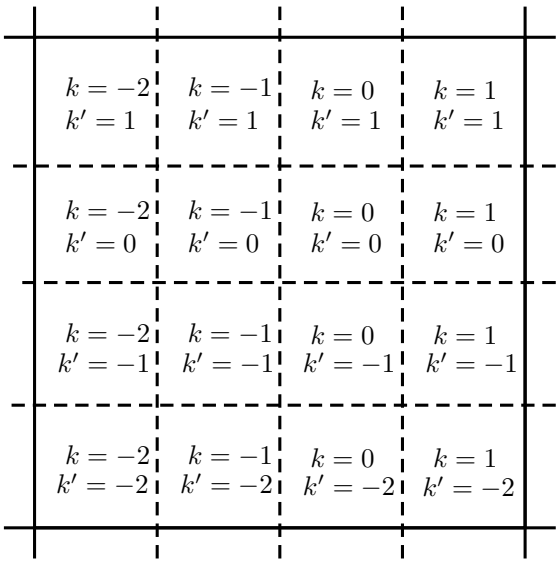

Figure 3.3: An example of how a plane at some z can be segmented into non-overlapping square patches indexed by two integers k and k'. The width of each patch is equal to the width of the available detector. All the patches must be considered to know the entire slice at z. But usually, there are a finite number of detectors so that only a few patches can be covered. In that case, only those Haar wavelets and scaling functions are considered which have a compact support on the considered patches.

are labelled using two indices k and k' which take integer values. Each square patch supports a countably infinite set of Haar wavelets that fall entirely within the patch. Together with the Haar scaling function that covers the square patch, all the supported Haar wavelets form a basis for any function that has compact support over the patch. The first element of this basis is the Haar scaling function that covers the entire patch, i.e.,

$$g_1(x, y; z_1, j_0, k, k') \coloneqq \phi_{j_0,k}(x)\ \phi_{j_0,k'}(y - j_0), \tag{3.15}$$

where the dilation parameter of the scaling function, i.e., j_0 is set so that $g_1(x, y; z_1, j_0, k, k')$ covers the entire patch (see Eq. (2.32)), and $z = z_1$ is the plane on which the slice is considered. Note that we have chosen $y - j_0$ as the argument of the y component of the two-dimensional scaling function in Eq. (3.15), so the the scaling function is symmetrical about the x axis just like the window of the detector. The other elements of the basis are all Haar wavelets with compact support over the square

patch, i.e.,

$$g_\imath(x, y; z_1, j_0, k, k') := \psi_{m,n}(x)\psi_{m'n'}(y - j_0) \;\forall\; \imath > 1 \;\in\; \mathbb{Z}^+, \tag{3.16}$$

where $\mathbb{Z}^+$ is the set of positive integers. The subscript $\imath$ is a meta-index for m, n, m' and n', and

$$m \geq j_0, \tag{3.17}$$

$$2^{m-j_0}k \leq n < 2^{m-j_0}(k+1), \tag{3.18}$$

$$m' \geq j_0, \tag{3.19}$$

$$2^{m'-j'_0}k' \leq n' < 2^{m'-j'_0}(k'+1), \tag{3.20}$$

where the ranges ensure that all the wavelets have compact support over the square patch chosen. If such Haar functions for all the square patches are combined, the slice can be resolved in terms of these functions (see §2.3.3 for example).

The 2D wavelets are used as basis functions on each of these slices so that each slice can be represented as a column vector. By choosing the input and the output slices on either side of the slits, a transfer matrix mapping the input slice to the output slice can be calculated. However, the slice-to-slice map can also be done in a continuous manner where a propagator sequentially maps one slice to another very close to it, gradually moving forward in the z direction. Such a map is constructed using the surface term of the formal solution of the Helmholtz equation (see Eq. (3.2)), which is discussed in appendix C. However, for the purpose of showing that a double-slit is effectively a beam splitter, a direct transfer matrix between the input and output slices suffices.

The two detector-windows in the double-slit setup cover only two of the square patches. Consequently, they do not intercept the entire slice, but only a portion of it. Nevertheless, each detector window supports a countably infinite number of Haar functions. We justify the postselection of two input and two output modes.

3.3.1 Output modes

As the width of the detector is $w = 4$, we set $j_0 = -2$ so that the Haar scaling function covers the entire patch. According to the positions of the detectors in Fig. 3.2, the square patch occupied by the detector at port D_1 is the one with indices $k = 2,\ k' = 0$. Similarly, the patch covered by the detector at port D_2 is the one with $k = -3,\ k' = 0$. From the infinite set of Haar functions supported by the square patches, two have to be postselected. There are two ways to achieve that.

One way is to design a detector that responds to the projection of light on a particular Haar wavelet or scaling function. Although possible in principle, making such a detector is practically challenging because of the jump discontinuities in the Haar wavelet functions. Another and more tractable approach is to construct the double-slit setup in such a way that most of the light intercepted by the detectors has a projection on a single Haar wavelet or the scaling function, which becomes a detector mode. Consequently, even if the detector is multimode, the detection is in single mode. The latter is the case with the double-slit setup considered in this work.

To find such modes, the diffracted fields intercepted by the detector windows (ports D_1 and D_2) are resolved in terms of the corresponding Haar functions. For example, the field $E_1^{(1)}(x, y; z_2)$ can be expanded as

$$E_1^{(1)}(x, y; z_2) = \sum_{\imath=1}^{\infty} A_\imath(z_2)\ g_\imath(x, y; z_2, -2, 2, 0), \tag{3.21}$$

where $A_\imath(z_2)$ are the projections of the field on the corresponding Haar function. For convenient visualization, the field at $y = 0$, i.e., $E_1^{(1)}(x, 0; z_2)$ is shown in Figs. 3.4 and 3.5.

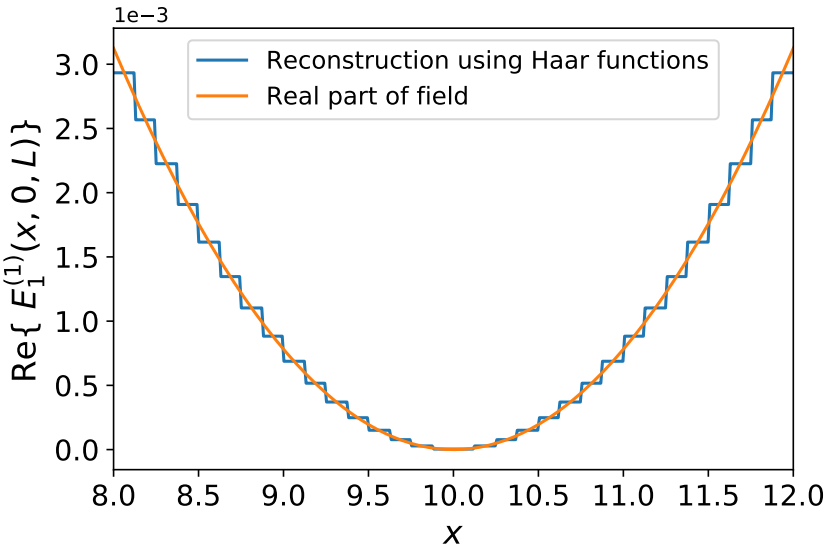

Figure 3.4: Reconstruction of the real part of $E_1^{(1)}(x, 0, z_2)$ using the wavelets supported over the patch $k = 2,\ k' = 0$, using Eq. (3.21). The values of dilation parameter m for the Haar wavelets (as in Eq. (2.17)) is taken from -2 to 2 so that the Haar wavelets are visible. A finer reconstruction can be done by taking m upto higher values. For m upto 6, the reconstruction is almost perfect.

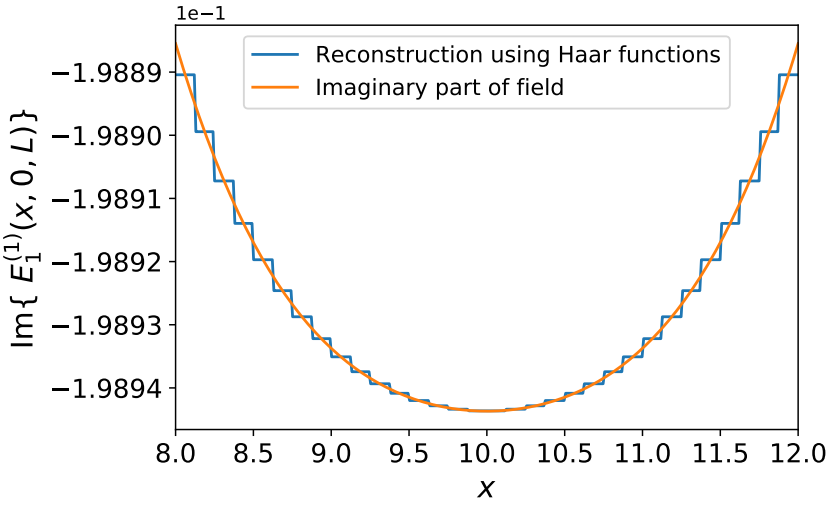

Figure 3.5: Reconstruction of the imaginary part of $E_1^{(1)}(x, 0, z_2)$ using the wavelets supported over the patch $k = 2,\ k' = 0$, using Eq. (3.21). The values of dilation parameter m for the Haar wavelets (as in Eq. (2.17)) is taken from -2 to 2 so that the Haar wavelets are visible. A finer reconstruction can be done by taking m upto higher values. For m upto 6, the reconstruction is almost perfect.

Although it takes more than one basis function to capture the fine features of the field, most of the power of the light resides in just one mode, i.e., $g_1(x, y; z_2, -2, 2, 0)$. The proof of this fact is in Table 3.1, where the total power intercepted by port D_1

is compared with the total power in the projection on $g_1(x, y; z_2, -2, 2, 0)$. The calculation shows that about 99.9956% of the total power is in the said projection. The field $E_1^{(2)}(x, y; z_2)$ also has most of the power in this mode. Therefore, we ignore all the other Haar functions which have negligible contribution to the field. Similarly, for detector port D_2, the dominant contribution is from $g_1(x, y; z_2, -2, -3, 0)$. Henceforth, two post-selected output modes are

$$e_1(x, y; z_2) \coloneqq g_1(x, y; z_2, -2, 2, 0), \tag{3.22}$$

$$e_2(x, y; z_2) \coloneqq g_1(x, y; z_2, -2, -3, 0), \tag{3.23}$$

which reduce the infinite-dimensional representation of the slice at $z = z_2$ to a two-dimensional column vector

$$\boldsymbol{Y}^{(i)}(z_2) = \begin{pmatrix} \left\langle e_1(z_2), E_1^{(i)}(z_2) \right\rangle \\ \left\langle e_2(z_2), E_2^{(i)}(z_2) \right\rangle \end{pmatrix}, \tag{3.24}$$

where $E_j^{(i)}(x, y; z_2)$ is the field from source S_i diffracted by slit A_j and therefore intercepted by the detector port D_j, and

$$\left\langle e_1(z_2), E_1^{(i)}(z_2) \right\rangle = \int_{-\infty}^{\infty} \mathrm{d}x \int_{-\infty}^{\infty} \mathrm{d}y \; e_1^*(x, y; z_2) \; E_1^{(i)}(x, y; z_2) \tag{3.25}$$

and similarly for the second entry in the column vector.

Integrated intensity intercepted	**Integrated projections on chosen modes**	**Ratio**
$\iint_{D_1} \mathrm{d}x\ \mathrm{d}y\ \left\lvert \bar{E}_1^{(1)}(x,y;z_2)\right\rvert^2 = 0.633115$	$\iint_{D_1} \mathrm{d}x\ \mathrm{d}y\ \left\lvert \left\langle e_1(z_2), \bar{E}_1^{(1)}(z_2)\right\rangle\right\rvert^2 = 0.633087$	99.9956%
$\iint_{D_2} \mathrm{d}x\ \mathrm{d}y\ \left\lvert \bar{E}_2^{(1)}(x,y;z_2)\right\rvert^2 = 0.61200$	$\iint_{D_2} \mathrm{d}x\ \mathrm{d}y\ \left\lvert \left\langle e_2(z_2), \bar{E}_2^{(1)}(z_2)\right\rangle\right\rvert^2 = 0.611971$	99.9952%
$\iint_{D_1} \mathrm{d}x\ \mathrm{d}y\ \left\lvert \bar{E}_1^{(2)}(x,y;z_2)\right\rvert^2 = 0.61200$	$\iint_{D_1} \mathrm{d}x\ \mathrm{d}y\ \left\lvert \left\langle e_1(z_2), \bar{E}_1^{(2)}(z_2)\right\rangle\right\rvert^2 = 0.611971$	99.9952%
$\iint_{D_2} \mathrm{d}x\ \mathrm{d}y\ \left\lvert \bar{E}_2^{(2)}(x,y;z_2)\right\rvert^2 = 0.633115$	$\iint_{D_2} \mathrm{d}x\ \mathrm{d}y\ \left\lvert \left\langle e_2(z_2), \bar{E}_2^{(2)}(z_2)\right\rangle\right\rvert^2 = 0.633087$	99.9956%

Table 3.1: A comparison of the total integrated intensity detected by the detectors and the square of the magnitudes of the projections of the fields on the chosen modes. The ratios show that most of the light intercepted by the detectors are in the chosen modes as in Eqs. (3.22) and (3.23). Therefore the choice of modes is justified.

3.3.2 Input modes

Each source in the double-slit setup (Fig. 3.2) emits light in a particular mode, for example spherical mode (approximately). The projection of the source modes on the slice at $z = z_1$ are projected on the Haar functions on that plane. The input modes chosen are square patches on the plane at z_1 centered at the same positions on the plane as the output ports are placed on plane at z_2. Moreover, the post-selected input modes are similar to those chosen for the output, i.e.,

$$e_1(x,y;z_1) \coloneqq g_1(x,y;z_1,-2,2,0), \tag{3.26}$$

$$e_2(x,y;z_1) \coloneqq g_1(x,y;z_1,-2,-3,0), \tag{3.27}$$

with z_1 denoting that the modes are for a slice on plane $z = z_1$. Note that the input and output modes are distinguished using the parameter that denotes the plane on which the slice is, i.e., z. Therefore, the post-selected two-dimensional vector

representation of the input, i.e., slice at $z = z_1$

$$\boldsymbol{X}^{(i)}(z_1) = \begin{pmatrix} \left\langle e_1(z_1), E_1^{(i)}(z_1) \right\rangle \\ \left\langle e_2(z_1), E_2^{(i)}(z_1) \right\rangle \end{pmatrix}, \tag{3.28}$$

where the superscript denotes that source S_i is turned on. With the input and output slice modes postselected, we need a transfer matrix that maps the input modes to the output modes.

3.4 The effective 2×2 transfer matrix

The transfer matrix $T(z_2, z_1)$ must map the input vector $\boldsymbol{X}^{(i)}(z_1)$ to the output vector $\boldsymbol{Y}^{(i)}(z_2)$, i.e.,

$$T(z_2, z_1)\ \boldsymbol{X}^{(i)}(z_1) = \boldsymbol{Y}^{(i)}(z_2), \tag{3.29}$$

for $i \in \{1, 2\}$, which gives a set of four simultaneous equations for the four elements of $T(z_2, z_1)$. To solve the equations, the double-slit setup is characterized numerically, by calculating $\boldsymbol{X}^{(i)}(z_1)$ and $\boldsymbol{Y}^{(i)}(z_2)$ for each source turned on at a time. The transformation equation for both sources are combined into one matrix equation

$$T(z_2, z_1) \begin{pmatrix} \boldsymbol{X}^{(1)}(z_1) & \boldsymbol{X}^{(2)}(z_1) \end{pmatrix} = \begin{pmatrix} \boldsymbol{Y}^{(1)}(z_2) & \boldsymbol{Y}^{(2)}(z_2) \end{pmatrix}, \tag{3.30}$$

where $\begin{pmatrix} \boldsymbol{X}^{(1)}(z_1) & \boldsymbol{X}^{(2)}(z_1) \end{pmatrix}$ is a 2×2 matrix with $\boldsymbol{X}^{(1)}(z_1)$ and $\boldsymbol{X}^{(2)}(z_1)$ as columns, and similar for the right-hand side. Inverting Eq. (3.30) yields

$$T(z_2, z_1) = \begin{pmatrix} \boldsymbol{Y}^{(1)}(z_2) & \boldsymbol{Y}^{(2)}(z_2) \end{pmatrix} \begin{pmatrix} \boldsymbol{X}^{(1)}(z_1) & \boldsymbol{X}^{(2)}(z_1) \end{pmatrix}^{-1}, \tag{3.31}$$

provided that $\begin{pmatrix} \boldsymbol{X}^{(1)}(z_1) & \boldsymbol{X}^{(2)}(z_1) \end{pmatrix}$ is invertible. In general, $\begin{pmatrix} \boldsymbol{X}^{(1)}(z_1) & \boldsymbol{X}^{(2)}(z_1) \end{pmatrix}$ is a symmetric matrix because of the symmetry in the setup, and the diagonal elements are slightly different from the off-diagonal elements as the projections of

field from one source is not equal on both the post-selected modes. Such a matrix is always invertible.

However, the effective transfer matrix is not unitary because diffraction is intrinsically a lossy process in which most of the light incident on the slits are blocked by the opaque areas and also the fact that the finite-sized detectors only intercept a portion of the slice. Moreover, the wavelets, chosen as bases of the Hilbert space of each slice, are not eigenfunctions of the Helmholtz equation. Therefore, there is cross-talk between different modes as one moves from one slice to another. Polar decomposition of the transfer matrix reveals the underlying unitary transformation. Such a decomposition factorizes the non-unitary transfer matrix into a unitary matrix and a Hermitian matrix.

3.5 Numerical results

Numerical calculations of the solutions of the Helmholtz equation (with Fraunhofer approximations, see §2.4) gives the resultant transfer matrices for the double and triple-slit setups. The effective 2×2 transfer matrix is calculated by characterizing the double-slit setup by turning one source on at a time. For each source the input and output slices have a post-selected vector representation. For the double-slit setup under consideration, the input and output vectors when source S_1 is on are

$$\boldsymbol{X}^{(1)}(z_1) \approx \begin{pmatrix} -394.761 - 41.473\ \mathrm{i} \\ 10.284 - 13.398\ \mathrm{i} \end{pmatrix}, \tag{3.32}$$

$$\boldsymbol{Y}^{(1)}(z_2) \approx \begin{pmatrix} 0.008 - 0.796\ \mathrm{i} \\ 0.782 + 0.008\ \mathrm{i} \end{pmatrix}, \tag{3.33}$$

with respect to the post-selected modes (see §3.3). Similarly, the post-selected vector representations of the input and output slice when source S_2 is on are

$$\boldsymbol{X}^{(2)}(z_1) \approx \begin{pmatrix} 10.284 - 13.398\ \mathrm{i} \\ -394.761 - 41.473\ \mathrm{i} \end{pmatrix}, \tag{3.34}$$

$$\boldsymbol{Y}^{(2)}(z_2) \approx \begin{pmatrix} 0.782 + 0.008\ \mathrm{i} \\ 0.008 - 0.796\ \mathrm{i} \end{pmatrix}. \tag{3.35}$$

We use the above results in Eq. (3.31) to calculate the effective transfer matrix.

With respect to the post-selected input and output vectors, the effective transfer matrix is

$$T(z_2, z_1) \approx \mathrm{e}^{0.476\pi\mathrm{i}} \begin{pmatrix} 2.07 & 1.90\ \mathrm{e}^{0.486\pi\mathrm{i}} \\ 1.90\ \mathrm{e}^{0.486\pi\mathrm{i}} & 2.07 \end{pmatrix} \times 10^{-3}, \tag{3.36}$$

which is a symmetric matrix as expected from the symmetry of the double-slit setup (Fig. 3.2). Note that apart from a factor of about $\mathrm{e}^{0.476\pi\mathrm{i}} \times 2\sqrt{2} \times 10^{-3}$, the matrix $T(z_2, z_1)$ is approximately (but not exactly) a 50:50 beam splitter matrix. The deviation from the ideal 50:50 beam splitter is due to the non-unitary nature of the transfer matrix. To reveal the exact unitary transformation the polar decomposition of the transfer matrix is performed.

As expected, the transfer matrix $T(z_2, z_1)$ is not unitary as can be seen from

$$T(z_2, z_1)T^{\dagger}(z_2, z_1) \approx \begin{pmatrix} 7.90 & 0.35 \\ 0.35 & 7.90 \end{pmatrix} \times 10^{-6} \neq \begin{pmatrix} 1 & 0 \\ 0 & 1 \end{pmatrix}, \tag{3.37}$$

because of the reasons discussed in §3.4. To reveal the underlying unitary transformation a polar decomposition of $T(z_2, z_1)$ is carried out which yields,

$$T(z_2, z_1) = U(z_2, z_1)P(z_2, z_1), \tag{3.38}$$

where the result for the double-slit system considered in this paper, i.e. the polar

decompostion of the transfer matrix in Eq. (3.36) is

$$U(z_2, z_1) \approx \mathrm{e}^{0.47\pi \mathrm{i}} \times \frac{1}{\sqrt{2}} \begin{pmatrix} 1.04 & 0.95\ \mathrm{i} \\ 0.95\ \mathrm{i} & 1.04 \end{pmatrix}, \tag{3.39}$$

$$P(z_2, z_1) \approx \begin{pmatrix} 2.81 & 0.06 \\ 0.06 & 2.81 \end{pmatrix} \times 10^{-3}, \tag{3.40}$$

where U is the transformation of a 54:46 beam splitter upto a global phase (which is irrelevant as the detectors are square-law type) [39]. The Hermitian component $P(z_2, z_1)$ captures the non-unitarity of the transfer matrix. Its diagonal elements show the fraction of the input that is detected by the detectors after post-selection. The off-diagonal terms show cross-talk between the two modes. Note that the near-diagonal form of the matrix $P(z_2, z_1)$ means that there is negligible cross-talk between the two modes and the nature of the non-unitarity is only attenuation in individual channels. Therefore, the double-slit setup in Fig. 3.2 is effectively a lossy beam splitter with respect to the post-selected input and output modes.

For verification, the cross-correlation of the postselected outputs is calculated, and the result is compared with what is expected from an ideal beam splitter. In the next chapter, we discuss the classical equivalent of two-photon interference, which is a tool to characterize a linear interferometer. This helps connect the classical description of slit diffraction and the unitary framework that we have presented here with the unitary description of quantum interferometry.

Chapter 4

Hong-Ou-Mandel Dip with Classical Light

When two identical photons enter the two ports, one photon in each port, of a 50:50 beam splitter, they undergo two-photon interference (see Fig. 2.15). The outcome of such an interference manifests as bunching of photons at the output. If the probability of coincident photodetection at the two output ports, is observed as a function of the time-delay between the two incident photons, a dip is observed. Specifically, as the time-delay between the incident photons approaches zero, the probability of coincident detection also drops to zero, i.e., both the photons exit the same port. This phenomenon is called the Hong-Ou-Mandel effect (HOM effect)[21].

However, it is popular folklore that no semi-classical theory can explain the 100% HOM dip. Here, we show that the HOM effect is not an undisputed signature of the quantum nature of light. We show that the HOM effect can be mimicked using classical light in such a way that it cannot be distinguished from the HOM effect with photons [41]. Further, we show that to distinguish the classical version of the experiment from the quantum version, one must exploit the wave-particle duality of the photons, by setting up a complementarity experiment along with the HOM setup.

A brief outline of the semi-classical theory of photoelectric detection, as pro-

posed by Mandel, Sudarshan and Wolf [36, 37], and that is relevant to this work, is discussed in §2.7. We now describe how the HOM effect can be mimicked with classical pulses and conceptualize the experimental setup used to achieve this task.

4.1 Simulating HOM effect with classical pulses

In this section, we discuss the schematic of the experiment to demonstrate the simulation of the HOM effect with classical pulses. Consider two Gaussian pulses travelling perpendicular with respect to each other, each entering one port of a 50:50 beam splitter, as shown in figure 4.1. In classical electrodynamics, the two pulses will be represented by analytic functions of spacetime (or fields), i.e.,

$$E_1(\boldsymbol{r}, t; \boldsymbol{k}_1, \omega, 0, 0) = \mathcal{E}(\boldsymbol{k}_1 \cdot \boldsymbol{r} - \omega t)\ \mathrm{e}^{\mathrm{i}(\boldsymbol{k}_1 \cdot \boldsymbol{r} - \omega t)}, \tag{4.1}$$

$$E_2(\boldsymbol{r}, t; \boldsymbol{k}_2, \omega, \tau, \varphi) = \mathcal{E}(\boldsymbol{k}_2 \cdot \boldsymbol{r} - \omega t - \omega\tau)\ \mathrm{e}^{\mathrm{i}(\boldsymbol{k}_2 \cdot \boldsymbol{r} - \omega t + \varphi)}, \tag{4.2}$$

where E_i is the electric field of the i^{th} pulse. In general, the field is vectorial, but if both signals have the same polarization, the vector notation can be dropped. $\mathcal{E}$ is the amplitude-modulation of the signals (such as Gaussian), $\boldsymbol{k}_i$ is the propagation vector, ω is the angular frequency, φ is the relative phase between the two signals and τ is the time delay between the two pulses. The perpendicularity of the travelling directions of the two pulses necessarily and sufficiently implies that $\boldsymbol{k}_1 \cdot \boldsymbol{k}_2 = 0$. Furthermore, if the setup is such that the path lengths of both beams are equal, then we ignore the $\boldsymbol{r}$ dependence as well. Figures 4.2 and 4.3 show an example of the pulses. Note that the time delay τ appears only in the envelope and not in the carrier oscillating wave. A time delay introduced in the oscillating wave is equivalent to introduction of a phase shift and hence can be absorbed in φ.

In simplified notation, if the two perpendicular pulses serve as inputs to a balanced cubic beam splitter, the outputs are

$$E_{\pm}(t; \omega, \tau, \varphi) = \frac{1}{\sqrt{2}} \left(E_1(t; \omega, 0, 0) \pm E_2(t; \omega, \tau, \varphi) \right). \tag{4.3}$$

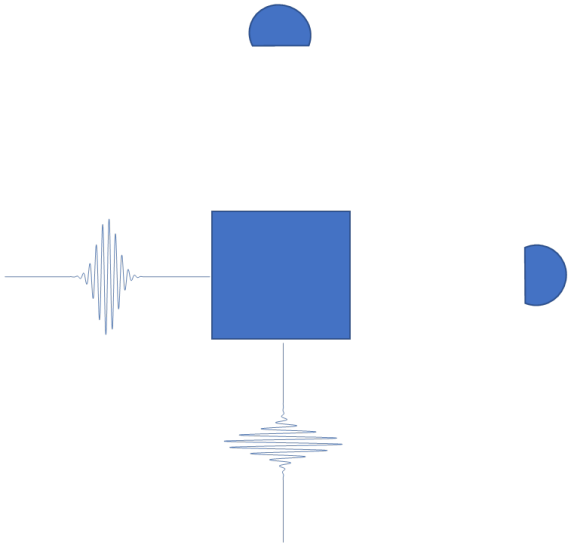

Figure 4.1: A cubic beam splitter with two input pulses entering its ports. Each pulse is sinusoidal pulse with Gaussian.

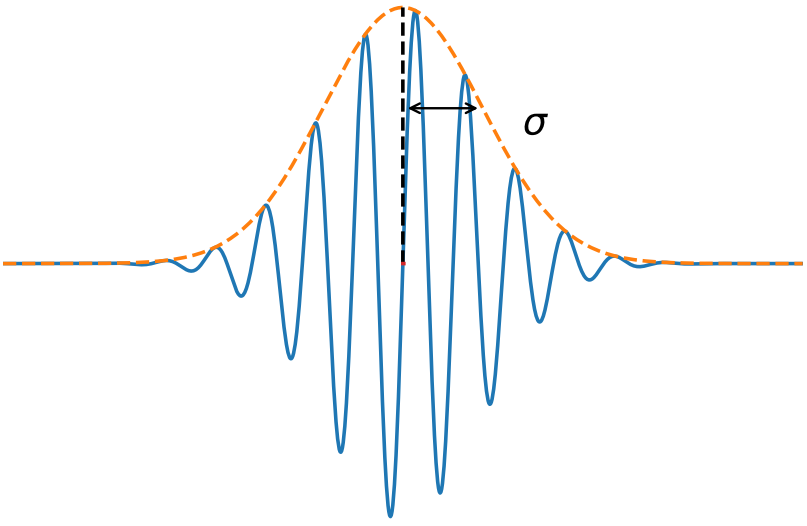

Figure 4.2: Example of a pulse with sinusoidal carrier and a Gaussian amplitude envelope.

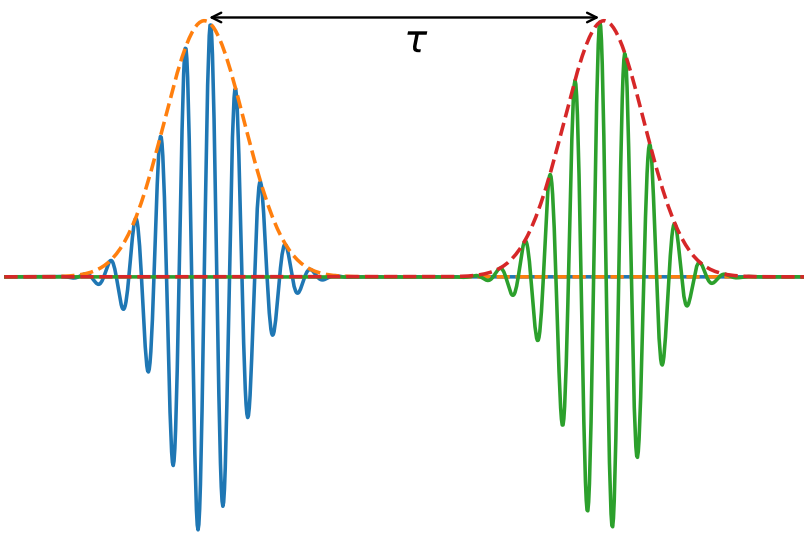

Figure 4.3: Two Gaussian pulses with a time delay of τ between them

We now introduce fluctuation in the signals by making the phase φ a random variable with a fixed probability distribution $P(\varphi)$ such that

$$\int \mathrm{d}\varphi \; P(\varphi) \; \cos\varphi = 0, \tag{4.4}$$

which yields

$$|E_{\pm}|^2 = \frac{1}{2} \left(|E_1|^2 + |E_2|^2 \right) \tag{4.5}$$

thereby revealing that second-order interference between the pulses is not observable if the time-scale of the fluctuation is much less than the time-scale of the measurement.

In the semi-classical theory of photodetection [36, 37], the coincidence probability at the two detectors is proportional to the cross-correlation of the integrated intensities at the detectors. The normalized correlation function is

$$C(\tau) := \frac{\int \mathrm{d}\varphi P(\varphi) \int_{T_{\mathrm{on}}}^{T_{\mathrm{off}}} \mathrm{d}t \, |E_+(t;\omega,\tau,\varphi)|^2 \int_{T_{\mathrm{on}}}^{T_{\mathrm{off}}} \mathrm{d}t' \, |E_-(t';\omega,\tau,\varphi)|^2}{\left[\int \mathrm{d}\varphi P(\varphi) \int_{T_{\mathrm{on}}}^{T_{\mathrm{off}}} \mathrm{d}t \, |E_+(t;\omega,\tau,\varphi)|^2\right] \left[\int \mathrm{d}\varphi' P(\varphi') \int_{T_{\mathrm{on}}}^{T_{\mathrm{off}}} \mathrm{d}t \, |E_-(t;\omega,\tau,\varphi')|^2\right]}, \tag{4.6}$$

where $E_+(t;\omega,\tau,\varphi)$, $E_-(t;\omega,\tau,\varphi)$ are the output fields from the transmitted and reflected ports of the 50:50 beam splitter respectively, when the input pulses have

carrier frequency ω, a time delay τ between them, and relative phase φ which fluctuates with probability $P(\varphi)$. Time $T = T_{\rm off} - T_{\rm on}$ over which each signal is measured is much larger than input-pulse width. We have normalized the correlation function so that it is independent of the amplitudes of the input pulses and the detector efficiencies. However, the correlation is still sensitive to the difference between the amplitudes of the individual pulses. Without loss of generality, setting $T_{\rm on} = 0$ and using Eqs. (4.1), (4.2) and (4.3), with the simplified notation, we obtain

$$\int_0^T \mathrm{d}t\, |E_{\pm}(t;\omega,\tau,\varphi)|^2 = \frac{1}{2}\int_0^T \mathrm{d}t\, \left[\mathcal{E}^2(t;\omega) + \mathcal{E}^2(t-\tau;\omega) \pm 2\mathcal{E}(t;\omega)\mathcal{E}(t-\tau;\omega)\cos\varphi\right]. \tag{4.7}$$

If T is large compared to input-pulse width, the first two terms are equal. The third term, which captures the temporal overlap of the two pulses, is a function of time delay and phase. From the definition of cross-correlation in Eq. (4.6) and (4.7), we obtain

$$C(\tau) = 1 - \frac{\mathcal{I}^2(\tau;\omega)}{\mathcal{I}^2(0;\omega)} \int \mathrm{d}\varphi\ P(\varphi)\ \cos^2\varphi, \tag{4.8}$$

where

$$\mathcal{I}(\tau;\omega) = \int_0^T \mathrm{d}t\ \mathcal{E}(t;\omega)\ \mathcal{E}(t-\tau;\omega), \tag{4.9}$$

Therefore, the correlation function depends on the ensemble of phases as well as the time-delay between the input pulse. The visibility of the correlation vs time-delay curve is

$$V = 1 - \frac{C(0)}{C(\tau)} = \int \mathrm{d}\varphi\ P(\varphi)\cos^2\varphi, \tag{4.10}$$

which depends on $P(\varphi)$.

The folklore that semi-classical theory cannot explain the HOM effect of a 100% dip in the coincidence probability, comes from the fact that, the probability distribution of the phases, i.e., $P(\varphi)$ is always chosen to be a uniform distribution over

the continuous interval $[0, 2\pi)$ as that is what happens when there is no control over the relative phase, i.e.,

$$P(\varphi) = \frac{1}{2\pi} \tag{4.11}$$

which when put in Eq. (4.10), yields

$$V = \frac{1}{2}, \tag{4.12}$$

as is claimed. However, there are other probability distributions that satisfy Eq. (4.4) so that the field-field interference is washed out. An example of which is the probability distribution

$$P(\varphi) = \frac{1}{2}\,\delta(\varphi) + \frac{1}{2}\,\delta(\varphi - \pi), \tag{4.13}$$

which means that the phases are picked uniformly from the discrete set $\{0, \pi\}$. Such a probability distribution gives a 100% dip in the cross-correlation function, i.e.,

$$V = 1, \tag{4.14}$$

thereby proving that the HOM effect can be simulated using classical pulses provided the ensemble of input signals are pre-selected appropriately. The point of emphasis here is that the chosen probability distribution still washes out the second-order interference, thereby revealing the higher-order interference. This fourth-order interference captured by the correlation function is a measure of the probability of coincident photoelectric detections at the two detectors. In the following section, we describe an example scenario in which this result can be used to simulate the HOM effect, such that it is indistinguishable from the quantum version of the experiment.

4.2 A thought experiment

HOM effect is considered one of the signatures of the quantum nature of light. However, the simulation of this effect with classical pulses implies otherwise. Consider a game with two participants, Alice and Bob. Alice has a source of classical light, and Bob has two photoelectric detectors. The game is for Bob to identify whether Alice's source generates classical light or quantum light (photons). As Bob considers the HOM effect as a signature of the quantum light, he brings a 50:50 beam splitter along with his detectors and places the two detectors at the two output ports as shown in Fig. 4.4. Bob's hypothesis is that Alice's source generates single photons. Therefore, he asks Alice to send two photons, one in each input port of the beam splitter, with different time-delays between them and repeat them several times to have a large statistical sample from which meaningful inference can be drawn. Bob's strategy is to plot the probability of coincidence detections and infer the nature of the light source from the visibility of the curve. If the dip in the curve is below or equal to 50%, he identifies the source as classical; otherwise, he identifies it as a quantum source.

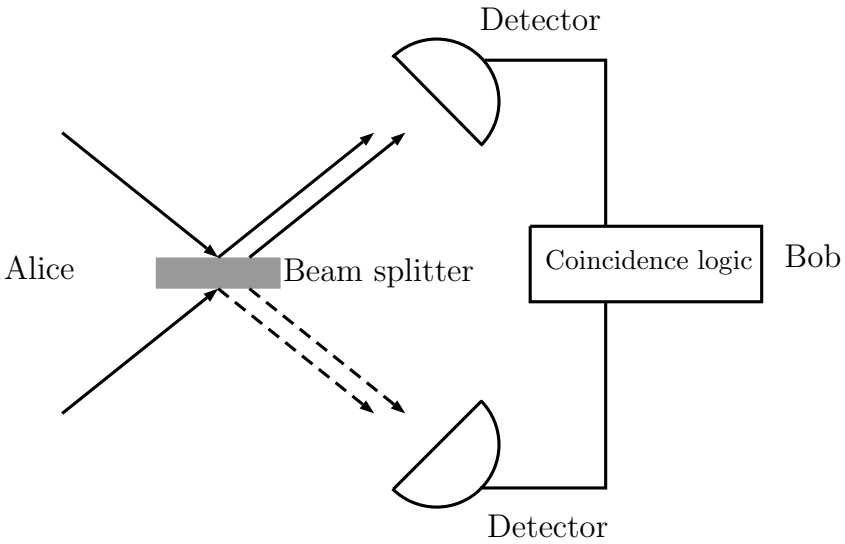

Figure 4.4: In this setup, Bob uses the HOM effect as a test to verify the two photons that Alice is supposed to send. The two signals generated by Alice are passed through a 50:50 beam splitter and the output is recorded by two photoelectric detectors by Bob. The two detectors are connected to a coincidence logic that counts the coincident photoelectric detections at the two detectors.

Alice, on the other hand, has a classical source. As the semi-classical theory relates the photon number to the intensity of classical light, Alice sends in a very low-intensity signal, when Bob asks for single photons in each port of the beam splitter. The intensity of the input signals is low enough that at most a single photoelectric emission will take place when the light falls on a detector. However, Alice plans to misguide Bob into thinking that her source generates single-photons. She does this by controlling the relative phase between the classical input pulses so that Bob's coincidence probability vs time-delay graph shows a 100% dip. This way, Bob is fooled into thinking that Alice's source generates single-photons.

However, Bob is cleverer than Alice thinks, and he announces that even though his observation of HOM effect suggests that Alice's source generates single photons, he wants to extend the setup to construct a Mach-Zehnder interferometer(MZI) and check for interference effects. Bob's extended setup is shown in figure 4.5. He closes an MZI and puts a phase-shifter in one of the arms. If Alice's source indeed generates single photons, Bob should see an interference effect as he rotates the phase-shifter as the superposition of biphoton state in the two arms of the MZI will show interference. Let us assume that the time-delay between the two inputs is set to zero. Then, in the two-photon case, the input to the beam splitter can be written in Fock basis as $|1,1\rangle$. On passing the first beam splitter, the output is the N00N state

$$\frac{1}{\sqrt{2}}(|2,0\rangle - |0,2\rangle). \tag{4.15}$$

The phase-shifter imparts a phase, say θ, in one of the arms and therefore, the input to the second beam splitter in the MZI becomes

$$\frac{1}{\sqrt{2}}\left(|2,0\rangle - \mathrm{e}^{\mathrm{i}\theta}\,|0,2\rangle\right).$$

The output of the second beam splitter is then

$$\frac{1-\mathrm{e}^{\mathrm{i}\theta}}{2\sqrt{2}}\left(|2,0\rangle+|0,2\rangle\right)+\frac{1+\mathrm{e}^{\mathrm{i}\theta}}{2}|1,1\rangle$$

and therefore, an interference pattern is observed as the phase-shifter is rotated. For the trivial case of $\theta = 0$ (no phase-shift), the output is $|1,1\rangle$ as expected.

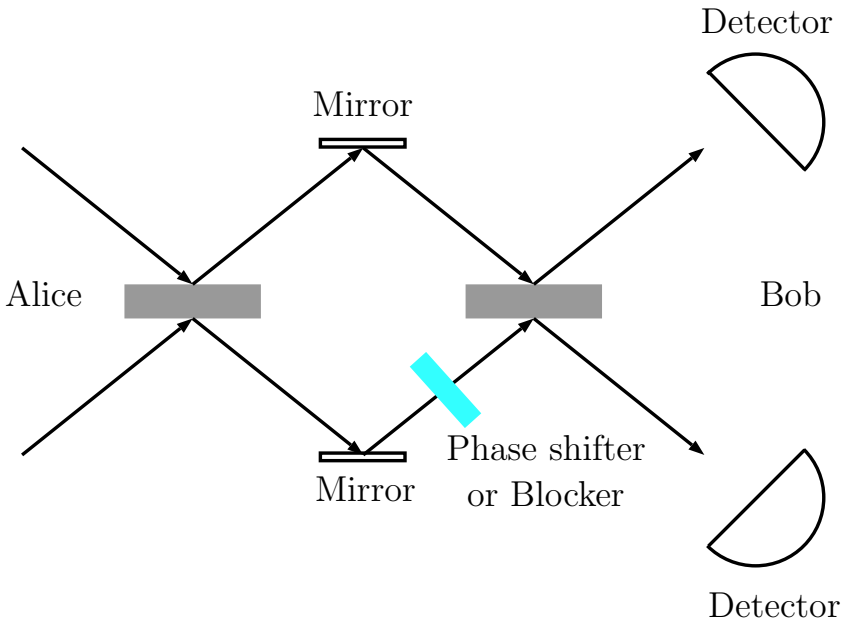

Figure 4.5: Having checked for the HOM effect with the setup in Fig. 4.4, Bob checks for interference at the outputs of a Mach-Zehnder interferometer (MZI). A phase shifter or blocker is placed in one of the arms of the MZI.

On the other hand, in the case with classical pulses, the phase-shifter doesn't give rise to such interference at the output, as the output of the first beam splitter always travels entirely through one of the arms of the MZI. The outputs fields of the second beam splitter are

$$\eta_{\pm}=\frac{1}{\sqrt{2}}\left[E_{+}\pm\mathrm{e}^{\mathrm{i}\theta}E_{-}\right], \tag{4.16}$$

where θ is the phase introduced in one arm. Note that when $\varphi \in \{0,\pi\}$ one of $E_{\pm}$ is always zero and consequently, the terms involving θ always vanish, making $|\eta_{\pm}|^2$ independent of the phase that is introduced by the phase-shifter. In terms of coincidence probability, the phase-shifter affects the coincidence rate in the quantum

case but leaves it untouched in the classical case.

But since Bob has announced that he wants to check for interference, Alice changes the settings of her source such that the relative phase of the input pulses is uniformly randomized over the continuous interval $[0, 2\pi)$. Therefore, the pulses will no longer simulate the HOM effect but will show interference at the outputs of the MZI. Therefore, Bob is fooled again. Note that, Bob cannot do both types of measurements, i.e., HOM effect and interference in MZI, simultaneously. Alice takes advantage of this situation and changes the source settings appropriately to always convince Bob that her source generates single photons.

Bob is unable to identify the classical nature of Alice's source because Alice adjusts the source setting based on what experiment or test Bob is going to perform. However, if Bob does not announce in advance which test he is going to perform, Alice will not know which setting to apply and will get caught. In case of a single-photon source, no such adjustment is required to pass either of the tests that Bob performs. This is because photons exhibit wave-particle duality without any change in the source settings, whereas the classical pulses fail that test. Therefore the wave-particle complementarity is the undisputed signature of the quantumness of light.

Now we will discuss the experiment to mimic HOM effect followed by another experiment to test for the wave-particle complementarity showing that the classical version will fail the complementarity test.

4.3 The experimental setup

In this section, we describe the experiment used to simulate the HOM effect using classical pulses and the MZI setup used to distinguish between the classical and quantum case by exploiting the wave-particle complementarity nature of photons. The key to demonstrating HOM effect with classical pulses is controlling φ, which is achieved in an optics experiment using electro-optic modulators (EOM) [42, 43, 44]. However, the accuracy of the correlation function depends on the input pulses being

identical. Pulse distortion caused by EOMs can increase distinguishability, thereby reducing the visibility of the correlation curve. Moreover, maintaining identical polarization, perfect alignment of the beams as well as active phase control in such an experiment that requires many iterations, is cumbersome. This challenge motivated our use of a novel, carefully designed electrical version of the beam splitter experiment shown in Fig. 4.6. As electrical signals with accurate phase control are directly generated, an extra apparatus for phase control is not needed. This innovation also eliminates polarization and alignment issues leading to a clean, precise experiment beyond the capability of optical systems, which enabled tremendous accuracy and precision in demonstrating the HOM effect with classical fields.

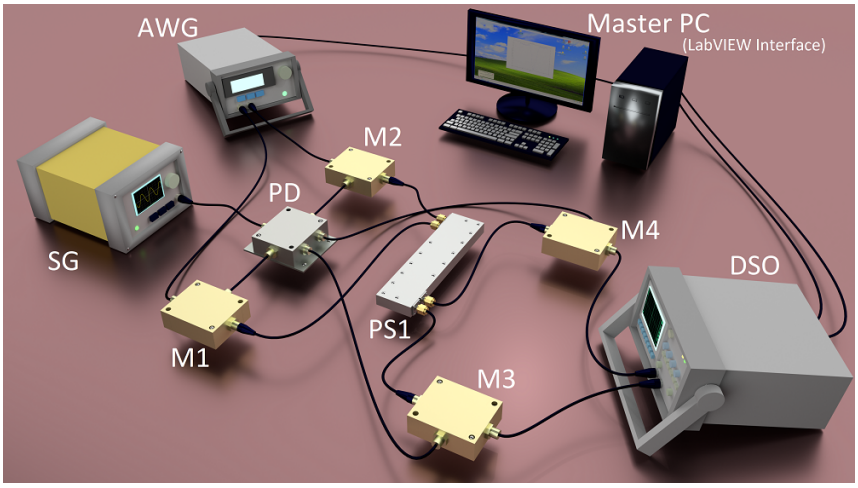

Figure 4.6: Schematic for the HOM experiment using classical microwave pulses. Detailed description of the setup is in the main text.

An arbitrary waveform generator (AWG) (Keysight Technologies-33622A) with dual-channel is programmed using LabVIEW to generate two sine signals with Gaussian amplitude modulation with 100 mV peak-to-peak and 1 kHz carrier frequency. The programmability of AWG facilitates the control of the relative phase φ and the time delay τ between the two pulses. The input-pulses are injected into a 180° power splitter PS1.

The two power splitters PS1 (and PS2 to be used in the MZI setup) are broadband (ET industries model: J-076-180) with operating frequency from 770 MHz to 6 GHz. Both power splitters are characterized, and from S-parameter analysis [45],

the operational frequency is chosen to be 1162 MHz, for which the power splitting ratios are closest to the ideal expectation of 50:50 (49.3:50.7 for PS1 and 50.3:49.7 for PS2) and phase error is around 2°-3°.

An oscilloscope (Agilent Technologies DSO60 14A), denoted by DSO in Fig. 4.6, is used as a detector with frequency sensitivity up to 100 MHz. As the desired operation frequency for the power splitters is 1162 MHz, signals from AWG are up-converted at the transmitter end and down-converted at the receiver end which requires mixers and a local oscillator. The local oscillator (SG) (Keysight Analog Signal generator N5173B), is tuned at 1161.999 MHz and connected to a one-input-four-output power divider (Mini circuits part number: ZA4PD-2). Mixers M1, M2, M3 and M4 (Mini circuits: FM-2000, level 7 mixer), which operate in the range of 100-2000 MHz, are driven by four output ports of a power divider PD. The power level from SG is set to +14 dBm to take care of power loss in the cable and power divider. The output shown on the oscilloscope screen is saved as a MATLAB® data file for post-processing. Detailed calculations of the signal processing are shown in §4.3.1 and §4.3.2.

Using LabVIEW we vary τ between -7 ms and 7 ms in steps of 1 ms to calculate the cross-correlation of the output signals for different time delays. The output signals recorded at the two channels of the oscilloscope are post-processed to calculate the cross-correlation using Eq. (4.6) and produce the plots of the cross-correlation as a function τ. The number of samples of pairs of input signal produced for good statistics is explained in §4.3.3.

4.3.1 Signal processing in the classical experiment

In the experiment, sinusoidal voltages play the role of the EM radiation. The time delay between input signals τ and relative phase φ are variable parameters. For each value of τ, an ensemble of output signals is generated with values of φ chosen from a chosen probability distribution. The ensemble is used to calculate cross-correlation.

Mathematical expressions of the signals generated using the AWG are

$$E_1(t;\omega,\tau,\varphi) = A_1 \text{ Exp}\left(-\frac{1}{2}\frac{t^2}{\sigma^2}\right) \sin(\omega t), \tag{4.17}$$

$$E_2(t;\omega,\tau,\varphi) = A_2 \text{ Exp}\left(-\frac{1}{2}\frac{(t-\tau)^2}{\sigma^2}\right) \sin(\omega t+\varphi), \tag{4.18}$$

where $A_1 = A_2 = 0.05$ V are the peaks of the Gaussian envelopes of the two signals. Both signals have Gaussian envelopes with $\sigma = 0.001$ s, and the sinusoidal wave has a frequency $f = 1$ KHz ($\omega = 2\pi f$).

The frequency range in which the power splitter has a splitting ratio of 50:50 is well beyond the maximum frequency that the AWG can produce. So, the effective input is generated by up-converting the frequency of the input signal by using a frequency mixer. The frequency of the local oscillator (SG) signal used for the mixing is $f_L = 1161.999$ MHz. A 4-port power-divider PD is used to branch the SG signal into four channels, two of which are used to up-convert the input signals, and the other two are used to down-convert the output of the power splitter. After the power splitter splits the inputs, the outputs need to be down-converted for measurement.

The measurement device used is an oscilloscope, two of whose channels are used to measure the two outputs of the power splitter. As the oscilloscope has an upper limit to the frequencies that it can measure, the high frequency output of the power splitter is down-converted using the LO. The result of down-conversion is a mixture of low and high frequencies. The oscilloscope acts as a low-pass filter and measures only the low frequency components, making the effective output (see Appendix D)

$$E_{\pm}(t;\omega,\tau,\varphi) = \frac{A_L^2}{2}\frac{E_1(t;\omega,\tau,\varphi) \pm E_2(t;\omega,\tau,\varphi)}{\sqrt{2}}. \tag{4.19}$$

Although the output depends on A_L, the cross-correlation function does not depend on it because of normalization.

4.3.2 Data acquisition and post-processing in the classical experiment

The digital oscilloscope samples the voltage signal at a sampling rate of 2 Giga-samples per second and consequently the recorded signal is a time-series of voltages $E_+^{(n)}(\tau,\varphi)$ and $E_-^{(n)}(\tau,\varphi)$. Each time-series contains a thousand points which implies that the time interval between successive points is $\Delta t = \frac{1}{2\times10^9}$s and the total acquisition time is $T = \frac{1000}{2\times10^9}$s.

To calculate $C(\tau)$ we take the ensemble average over the fluctuating φ. We focus our attention to fluctuation that is ergodic, described by a time-independent probability distribution $P(\varphi)$. The fluctuation can then be simulated by a discrete random process in which a pair of signals is generated with phase-difference φ, chosen from the said distribution.

4.3.3 Minimum N for good statistics

The relative phase φ of the input signals is averaged over so that there is no second-order interference as we are interested in studying only the fourth-order interference between the inputs. Consequently, the average integrated intensities of the output in both arms of the beam splitter (the normalization factor for the cross-correlation) are independent of τ. Therefore, to ensure the absence of the second-order interference, we determine the minimum number of samples (of φ) required to estimate the constant average-integrated-intensity within 5% error with a confidence level of 95% using the two-tailed test[46].

Let

$$\mu(\omega,\tau) = \int \mathrm{d}\varphi\ P(\varphi) \int_0^T \mathrm{d}t\ \left|E_\pm(t;\omega,\tau,\varphi)\right|^2 \tag{4.20}$$

be the true average-integrated-intensity of the output signals and

$$\mu^*(\omega,\tau) = \frac{1}{N}\sum_{i=1}^{N} \int_0^T \mathrm{d}t\ \left|E_\pm(t;\omega,\tau,\varphi_i)\right|^2 \tag{4.21}$$

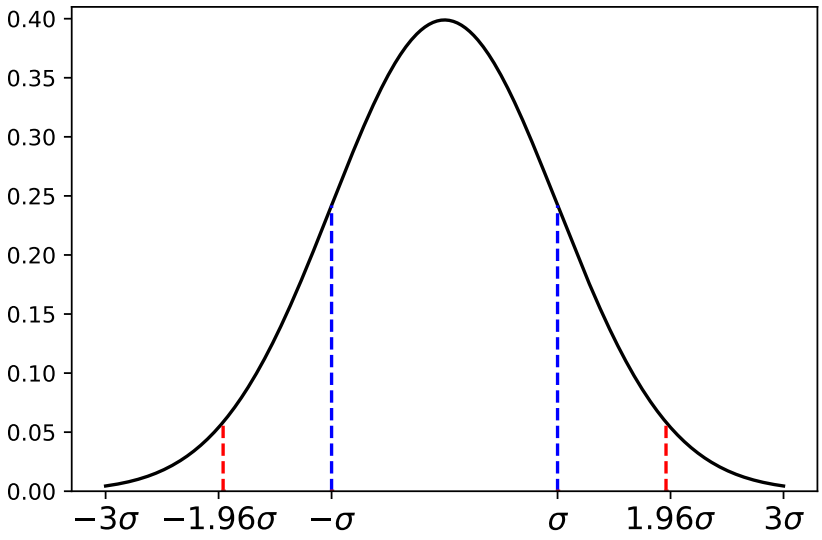

Figure 4.7: Plot of normal distribution. The dotted lines demarcate the boundaries of the confidence intervals. Between -1.96σ and 1.96σ the area under the curve is about 0.95.

be the average calculated from the sample outputs, where N is the number of samples recorded. Let

$$t = \sqrt{N}\frac{\mu^*(\omega,\tau) - \mu(\omega,\tau)}{\sigma(\omega,\tau)} \tag{4.22}$$

where $\sigma(\omega,\tau)$ is the true standard deviation of the integrated intensities for each τ. From the central limit theorem we know that for large enough N, the distribution of t will be closely approximated by the Normal distribution. As the 95% confidence interval for a normal distribution is $(-1.96, 1.96)$, the 95% confidence interval (C.I.) for $\mu^*(\omega,\tau)$ is

$$\text{C.I.} = \left(\mu(\omega,\tau) - \frac{1.96\ \sigma(\omega,\tau)}{\sqrt{N}}, \mu(\omega,\tau) + \frac{1.96\ \sigma(\omega,\tau)}{\sqrt{N}}\right) \tag{4.23}$$

If we want the error in the estimation of μ to be $\pm 5\%$ with 95% confidence, the width of the C.I. must be 10% of μ; i.e.,

$$2 \times \frac{1.96\ \sigma(\omega,\tau)}{\sqrt{N}} = 0.1\ \mu(\omega,\tau). \tag{4.24}$$

Equation (4.24) is then solved to get the minimum number of samples N required,

$$N(\omega,\tau) = \left(\frac{1.96\ \sigma(\omega,\tau)}{0.05\ \mu(\omega,\tau)}\right)^2. \tag{4.25}$$

In the 100% correlation dip case, the phase between the input signals is chosen uniformly from the set $\{0,\pi\}$, so the probability distribution of φ is

$$P(\varphi) = \frac{1}{2}\ \left(\delta(\varphi) + \delta(\varphi-\pi)\right), \tag{4.26}$$

and Fig. 4.8 shows $N_{\min}$ as a function of τ.

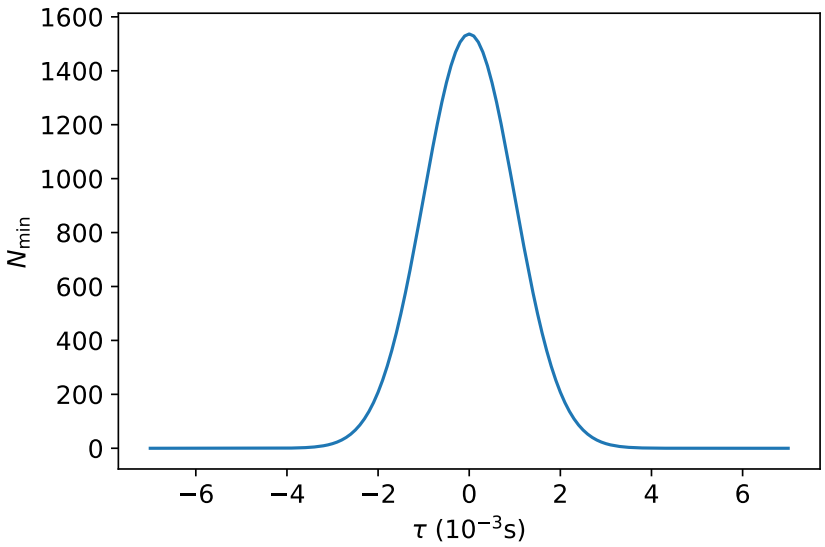

Figure 4.8: Plot of minimum number of samples (of φ) $N_{\min}$ versus the time delay τ between the input signals, for the experiment demonstrating 100% correlation dip.

The 50% correlation dip experiment is done in two versions. First the phase is chosen uniformly from the continuous interval $[0, 2\pi)$ for which

$$P(\varphi) = \frac{1}{2\pi}. \tag{4.27}$$

In the other version, the phase is chosen uniformly from the set $\left\{0, \frac{\pi}{2}, \pi, \frac{3\pi}{2}\right\}$ with probability distribution

$$P(\varphi) = \frac{1}{4}\ \left(\delta(\varphi) + \delta\left(\varphi - \frac{\pi}{2}\right) + \delta(\varphi-\pi) + \delta\left(\varphi - \frac{3\pi}{2}\right)\right). \tag{4.28}$$

In either case, the means and standard deviations for all values of τ are identical and hence $N_{\min}$ is given by the graph in Fig. 4.9.

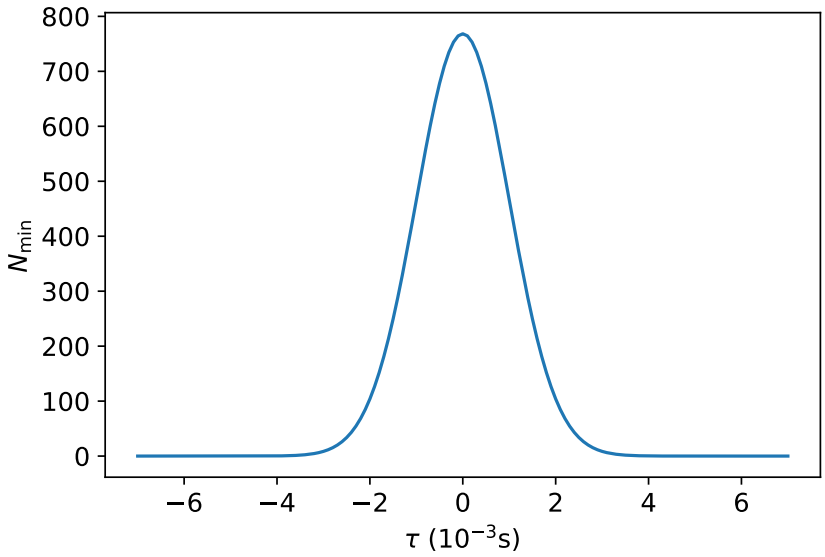

Figure 4.9: Plot of minimum number of samples (of φ) $N_{\min}$ versus the time delay τ between the input signals, for the experiment demonstrating 50% correlation dip.

The number of samples to be generated in the experiment is guided by the graphs in figures 4.8 and 4.9.

4.4 The result of classical experiment

To recreate the 50% dip in the cross-correlation, we run the experiment with a uniform probability distribution of phase over the continuous interval $[0, 2\pi)$. The result of calculated cross-correlation is shown in figure 4.10. The visibility of the correlation curve is

$$V = 0.481 \pm 0.025 \tag{4.29}$$

Figure 4.10 has two curves. The dotted curve is the theoretical estimate from Eq. 4.6, which shows a dip of exactly 50%. However, the experimental result does not show a dip of exactly 50%. The reason for that is the systematic error due to the mismatch of amplitudes of the input pulses. The amplitude mismatch is a result of different

attenuations in the different channels through which the signals travel. To account for the amplitude mismatch, we fit Eq. 4.6 with amplitude mismatch as the fit parameter. As is evident from Fig. 4.10, the fitted curve matches the result well.

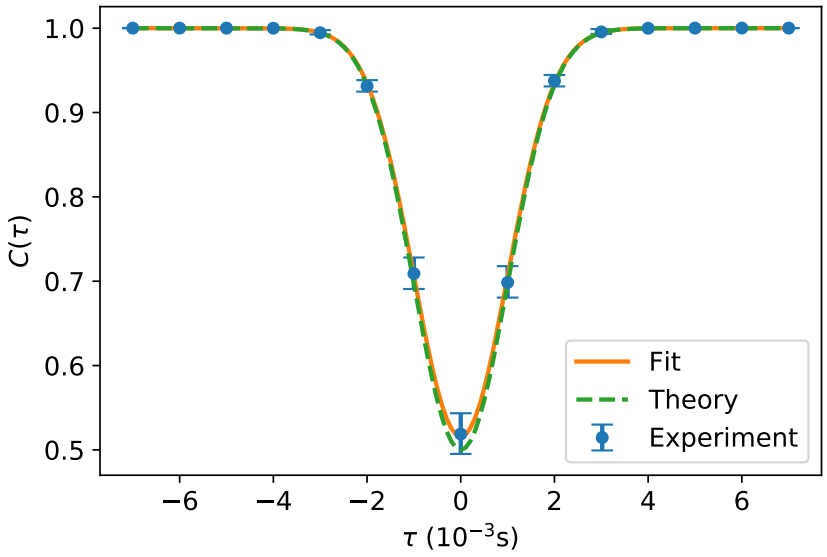

Figure 4.10: The normalized cross-correlation of the output pulses, as a function of the time delay τ between the input signals when the phase between them is uniformly random over the continuous interval $[0, 2\pi)$. The dots represent the experimental result. The green dashed "Theory" curve is the result of the theoretical calculation and shows a 50% dip. The attenuation of the signals causes an amplitude mismatch, which results in a dip slightly less than 50%. The cross-correlation is fitted to the experimental data to get the orange solid "Fit" curve by taking the amplitude mismatch as a fit parameter.

The remaining sources of error have a negligible contribution. However, for completeness, they must be discussed. Every instrument used in the circuit has an uncertainty in the measurement of the respective quantity. The maximum instrumental error was calculated using the specifications from the data-sheets of each instrument. The error in the beam-splitting ratio of the power splitters was found from their characterization. The relative error is plotted in Fig. 4.11. Other sources of errors include finite sampling rates of the AWG and the oscilloscope. However, the rates are sufficiently high for a near-perfect sampling of the signals.

Another way of achieving the 50% dip is to consider the following probability

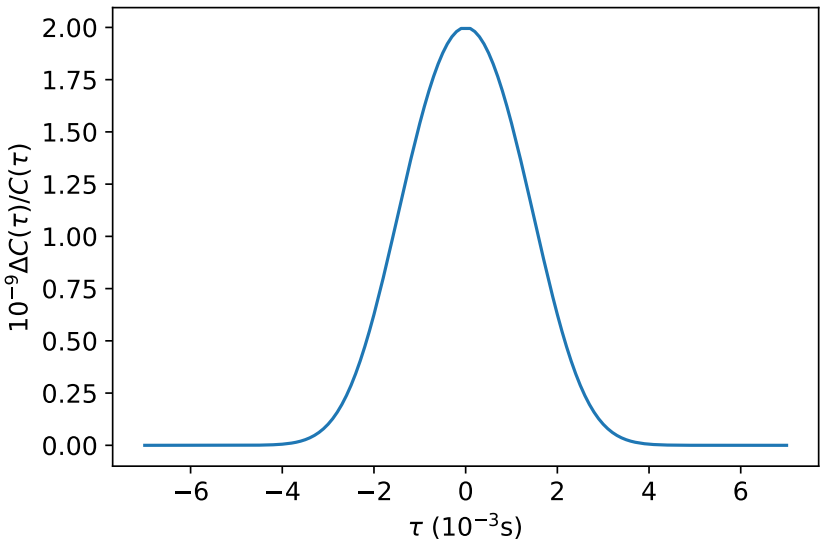

Figure 4.11: The relative error in the cross-correlation of the output signals due to various instrumental errors, as a function of the time delay τ between the input signals.

distribution,

$$P(\varphi) = \frac{1}{4}\left(\delta(\varphi) + \delta(\varphi - \pi/2) + \delta(\varphi - 3\pi/2) + \delta(\varphi - \pi)\right) \tag{4.30}$$

which also yields a 50% dip in the correlation function as shown in figure 4.12. The visibility achieved in this case is

$$V = 0.480 \pm 0.035. \tag{4.31}$$

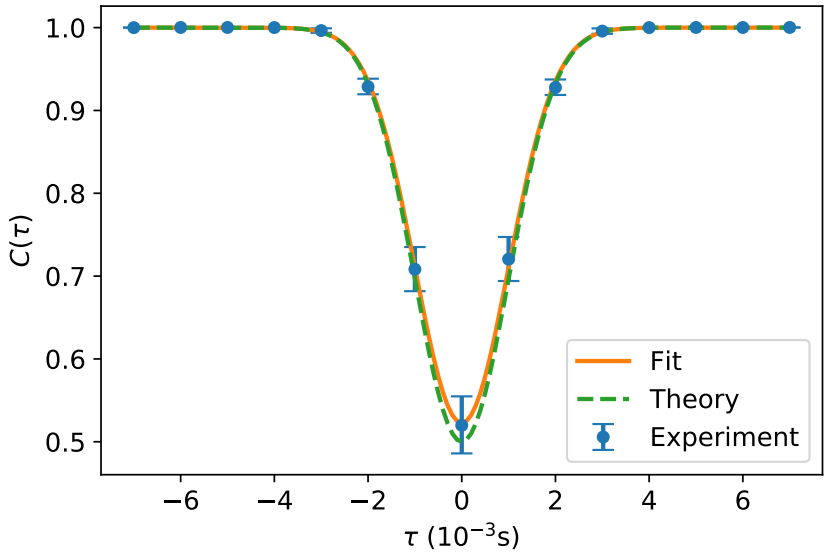

Figure 4.12: The plot shows the normalized cross-correlation as a function of time delay τ when the phase φ between the two input pulses is averaged over the set $\{0, \pi/2, \pi, 3\pi/2\}$ with all four values of phase difference being equally likely. The dots represent the experimental result, the green dashed line is the theoretical expectation, and the solid orange line is the result of fitting the theoretical expression for the cross-correlation to the experimental result, with amplitude mismatch between the input pulses as the fitting parameter. We obtain a TPCVD of 48.03% with the error bars representing 95% confidence interval of the mean value at each time delay.

Now we present the result of the experiment with phase been chosen uniformly from the set $\{0, \pi\}$. As figure 4.13 shows, the dip in the correlation is 100% as the time-delay approaches zero. We achieve visibility of

$$V = (99.635 \pm 0.002)\%, \tag{4.32}$$

which shows that a near 100% dip can be achieved with classical pulses as well if we can control and choose the fluctuations of the relative phase φ [41].

To compare the result of the classical version of the experiment, we show the result from the quantum version in the following section.

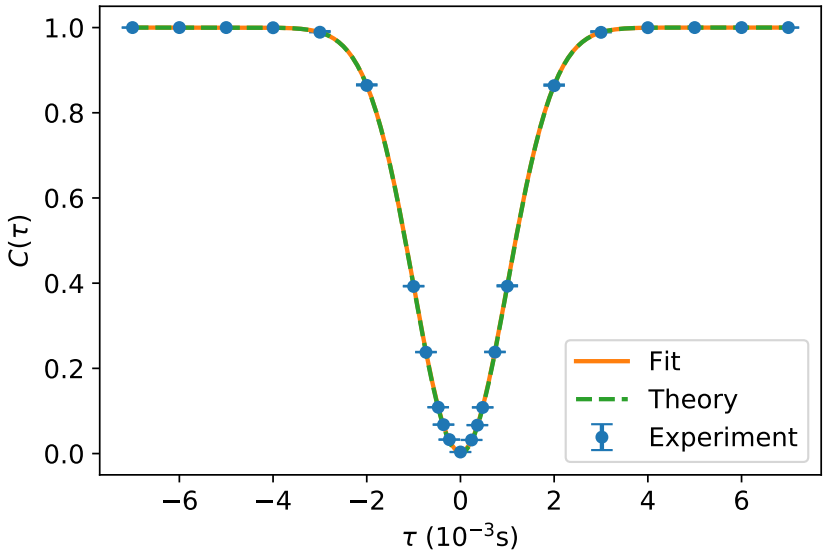

Figure 4.13: The plot shows the normalized cross-correlation as a function of time delay τ when the phase φ between the two input pulses to the beam splitter is averaged over the set $\{0, \pi\}$ with choice of 0 and π being equally likely. The dots represent the experimental result, the green dashed line is the theoretical expectation, and the solid orange line is the result of fitting the theoretical expression for the cross-correlation to the experimental result, with amplitude mismatch between the input pulses as the fitting parameter. The fitted curve overlaps almost completely with the theoretically expected curve. We obtain a TPCVD of 99.635% with the error bars representing 95% confidence interval of the mean value at each time delay.

4.5 Reproducing the HOM experiment

In the quantum version (see Fig. 4.14 for setup), we employ a Type II heralded photon source [47] in collinear configuration. A diode laser (Toptica-iwave) at 405 nm with 50 mW power pumps a 5 mm×5 mm×10 mm Type II BBO crystal. A pair of lenses of focal lengths 22.5 cm and 25 cm focus the pump beam at the crystal and collimate the down-converted photons, respectively. Pairs of orthogonally polarized frequency degenerate photons with a central wavelength of 810 nm are split in two directions by a polarizing beam splitter (PBS). A half-wave plate in one of the arms of the PBS makes the two photons have identical polarization. An arrangement of long-pass filters transmits wavelengths above 405 nm. A band-pass filter with a 3.1 nm bandwidth centred at 810 nm restricts the bandwidth of the transmitted photons also blocking any residual pump. Two fibre couplers collect photons from the same pair and inject them in a 2×2 polarization-maintaining fused fibre beam splitter (FBS).

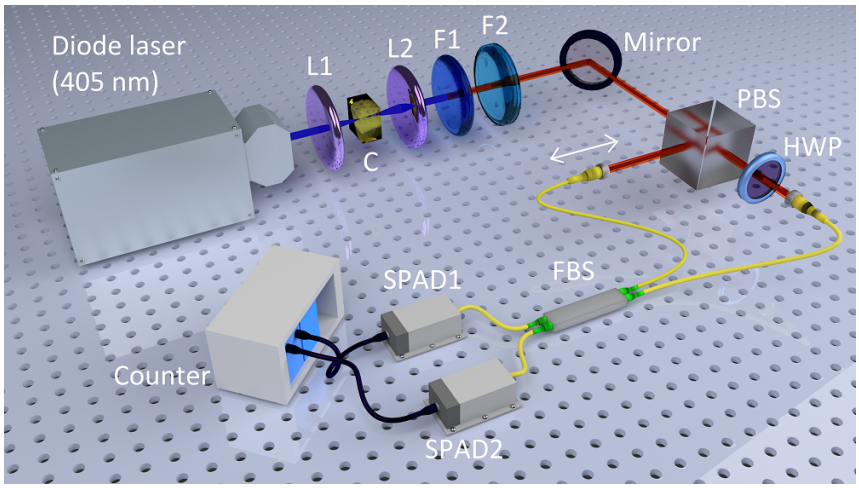

Figure 4.14: Schematic for the HOM experiment using IR photons. Detailed description of the setup is in the main text.

One of the couplers is mounted on a motorized stage to vary the delay between the two photons. We measure the coincidence count as a function of relative beam displacement between the signal and idler photons. A 10 μm step size for the stage provides necessary precision to resolve the HOM-dip width. The data acquisition time is 5 s at each position, and we measure at 160 positions. We repeat the mea-

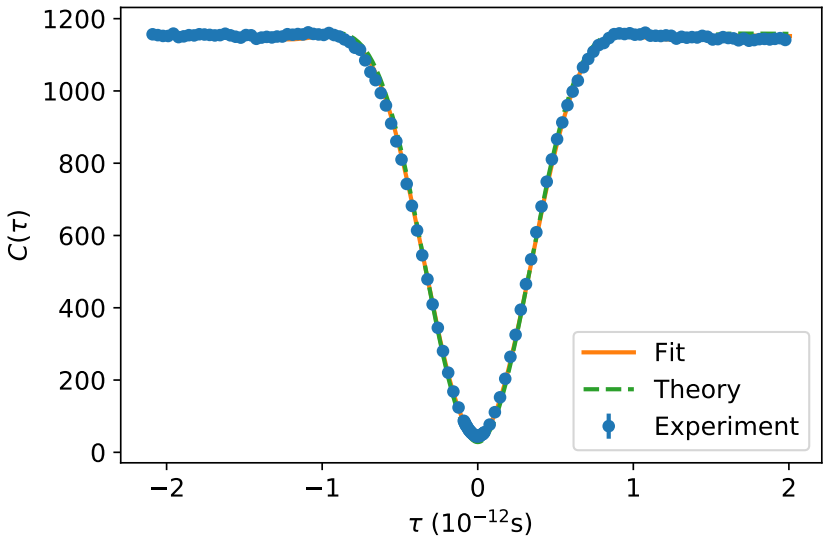

Figure 4.15: The dots represent the average coincidence-counts measured as a function of the time delay between the two input photons. The green dashed line is the theoretical expectation (see appendix E.1). The solid orange line is the result of fitting the theoretical result to the data (see appendix E.2) resulting in a correlation dip of 96.06%. The fitted line overlaps almost completely with the green dashed line (theoretical expectation). The R-squared value of the fit is 0.9998. The error bars represent 95% confidence intervals for the mean coincidence count at each time delay.

surement 100 times for better averaging and to estimate an error bar (see appendix F for details).

Figure 4.15 shows two-photon coincidence counts as a function of time delay τ between the two input photons. We obtain a correlation dip of (96.06 ± 0.16) %. Details concerning choice of parameters for both experimental setups are in Appendix E.

4.6 The complementarity test

Classical pulses indeed demonstrate a high degree of anticorrelation indicated by "HOM-like" dip, by applying appropriate relative-phase control between the two inputs. As the question of classical-vs-quantum nature is established by trying to realize particle-wave complementarity, we recombine outputs from the power splitter on a second power splitter PS2 to make a Mach-Zehnder interferometer

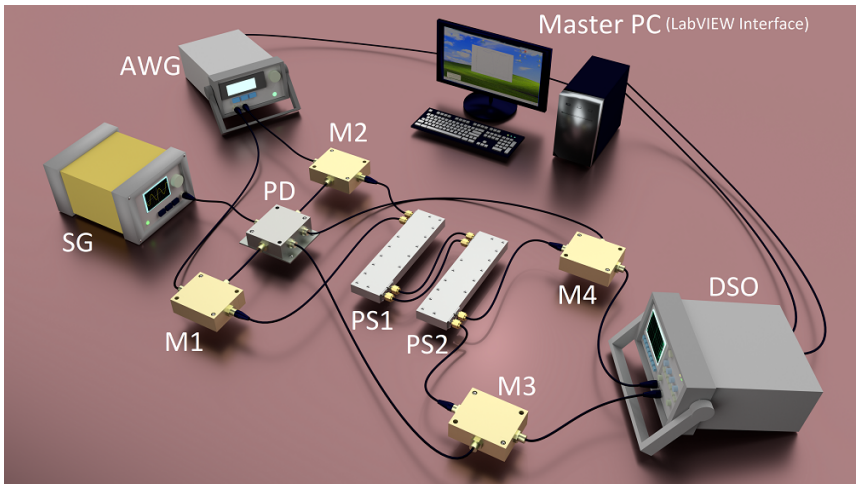

Figure 4.16: The schematic for the Complementarity experiment using classical pulses. A detailed description of the setup is in the main text.

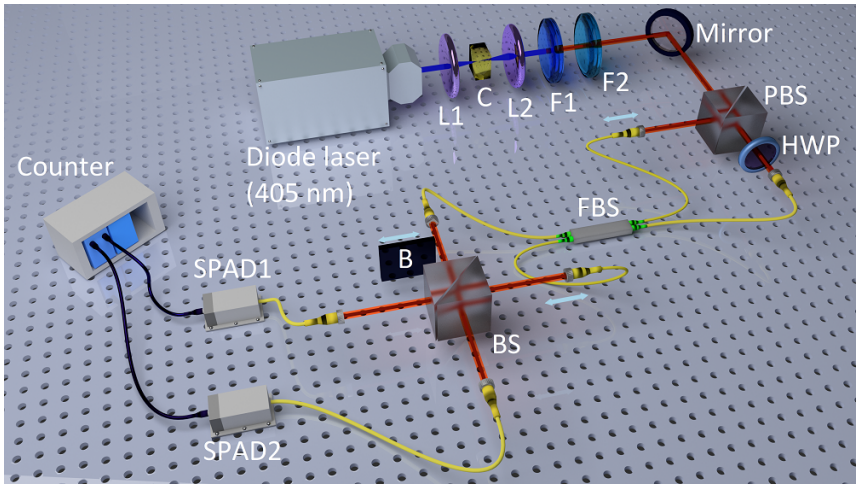

Figure 4.17: Schematic for the Complementarity experiment using IR photons. Detailed description of the setup is in the main text.

(MZI) to observe interference. Whether particle-like or wave-like behaviour can be observed in the classical case, depends crucially on the relative-phase choice for the inputs. Figures 4.16 and 4.17 show the schematics for the classical pulse and photonic versions of this experiment.

Instead of checking for complementarity through presence/absence of interference, we compare the classical and quantum cases using relevant ratios which only involve measurement at the central maximum of the interference pattern. This is a much simpler test for complementarity as it avoids phase stabilization of the interferometer in the IR domain and changing path lengths in the classical domain, which can be non-trivial.

We compare the case with both arms of the MZI unblocked (case A) with that in which one of the arms of the MZI is blocked (case B). In case A, the second power splitter/beam splitter recombines the arms to form the original inputs resulting in the probability of coincidence being 1 in both the classical and the quantum versions. But in case B, the results of the classical and quantum versions differ.

With classical pulses, the output of PS1 is in either one of the arms of the MZI, and the blocker blocks half of the signals to PS2. The unblocked arm simply splits into two resulting in a cross-correlation of 50% compared to that in case A. If the arm with field E_- is blocked

$$\eta_\pm = \frac{1}{\sqrt{2}} E_+ \implies |\eta_\pm|^2 = \frac{1}{2} |E_+|^2 . \tag{4.33}$$

On the other hand, if E_+ is blocked,

$$\eta_\pm = \pm \frac{1}{\sqrt{2}} E_- \implies |\eta_\pm|^2 = \frac{1}{2} |E_-|^2 . \tag{4.34}$$

In either case, the un-normalized cross-correlation function is

$$\tilde{C}(\tau) = \frac{I^2 + \mathcal{O}(\tau)}{4} \tag{4.35}$$

where

$$\mathcal{O}(\tau) = \int_{-\infty}^{\infty} \mathrm{d}t \; \mathcal{E}(t)\mathcal{E}(t-\tau) \tag{4.36}$$

and $I = \mathcal{O}(0)$. Specifically, $C(0) = \frac{I^2}{2}$ compared to I^2 when none of the arms is blocked. However, in either case $|\eta_+|^2 = |\eta_-|^2$ and hence perfectly correlated, which implies that classical theory predicts that there will never be a click in only one detector.

In the quantum version, the blocker collapses the superposition state to either $|2,0\rangle$ or $|0,2\rangle$ with equal probability, which blocks half of the states, say $|0,2\rangle$, from reaching the second beam splitter. $|2,0\rangle$ after going through the beam splitter

transforms to

$$|2,0\rangle \mapsto \frac{1}{\sqrt{2}}|1,1\rangle + \frac{1}{2}|2,0\rangle + \frac{1}{2}|0,2\rangle \tag{4.37}$$

yielding a coincidence probability of half. The drop in coincidence probability combined with the fact that half of the superposition states were blocked, results in a 25% coincidence rate compared to that in case A.

If one of the arms is blocked, the coincidence count drops. Say $|0,2\rangle$ is blocked, then a projection operator on the state yields

$$I \otimes \sum_n |0\rangle\langle n| \left(\frac{|2,0\rangle - |0,2\rangle}{\sqrt{2}}\right) = \frac{1}{\sqrt{2}}\left(|2,0\rangle - |0,0\rangle\right). \tag{4.38}$$

Further, applying the second beam splitter $\hat{B}$ on this state makes the output

$$\begin{aligned}\hat{B}\frac{1}{\sqrt{2}}\left(|2,0\rangle - |0,0\rangle\right) =& \frac{1}{2\sqrt{2}}\left(|2,0\rangle + |0,2\rangle + \sqrt{2}|1,1\rangle\right) \\ &- \frac{1}{\sqrt{2}}|0,0\rangle .\end{aligned} \tag{4.39}$$

This means that the coincidence probability drops from one down to a quarter. This drop in probability is a combined effect of the loss of half of the biphotons due to blocking and the absence of interference between the two arms.

Therefore the classical description predicts that the coincidence probability drops down by a factor of 2, which is different from the prediction of the quantum theory according to which this factor is 4. This result is equivalent to the complementarity test and separates the classical theory from quantum theory.

In experiment, we complete the MZI after PS1 with another power splitter PS2. The time delay between the two input pulses to PS1 is fixed at $\tau = 0$. The two outputs of PS1 are fed to PS2 (case A). The cross-correlation of outputs of PS2 is calculated.

Next, we block one arm of the MZI (case B). The connection between the Σ port of PS1 and 180° port of PS2 is removed, and both ends are terminated with

50 Ω terminators. The ratio between the cross-correlation values in cases A and B is computed and found to be **0.4919 ± 0.0242**. The sources of error are discussed in appendix E.

To demonstrate complementarity in the quantum case, we make the two input photons indistinguishable, i.e., $\tau = 0$ so that the output of the first beam splitter is the superposition of $|2,0\rangle$ and $|0,2\rangle$. The two outputs of the FBS are incident on a 50:50 beam splitter BS through two collimators. One of the collimators is placed on a motorized translational stage to vary the path difference (Δl) between the two arms of the MZI. The output ports of BS are coupled to single-mode fibres that are connected to two single-photon counting modules (τ-SPAD from Pico Quant) for coincidence measurement using a universal quantum device time-tagging unit.

We measure coincidence counts as a function of Δl and observe interference. However, to compare with the classical version, we fix $\Delta l = 0$, i.e., at the interference maximum. We then compare the coincidence count in case A with that in B.

To determine the position of the translational stage such that Δl=0, we make the time delay between the input photons large so that there is no two-photon state in the MZI arms. Then we use the interference pattern between the two arms of MZI to set the stage position for which $\Delta l = 0$. We then make the time delay between input photons zero again. The result of our experiment is a ratio of **0.25 ± 0.009**.

This confirms that in the quantum case, we observe complementarity between 100% correlation dip (particle-nature) and interference (wave-nature) with the same setting of the sources. The classical signal was not in a superposition state thereby not exhibiting wave-nature.

Our theory and experiment elucidate the quantumness of one of the most famous, ubiquitous and useful quantum optics experiments. In summary, we have shown that the semi-classical theory of photodetection can be applied to calculate the coincidence probability in a HOM experiment, provided the ensemble of inputs is chosen appropriately. The 50% threshold for the dip in coincidence probability is not the boundary between classical and quantum behaviours of light, but rather a result

of the lack of control over the phases of the input pulses. Although classical pulses can be made to switch between exhibiting particle-like and wave-like behaviours by controlling the phase, both cannot manifest with the same choice of phase. A two-photon state, on the other hand, shows wave-particle complementarity, by being indivisible in an anticorrelation experiment vs taking a superposition of two paths when interference is measured in an MZI, without any change in the source setting. This wave-particle complementarity is the boundary between the classical and the quantum.

The nature of the correlation of the outputs of a beam-splitter is a signature of that beam splitter. We use this signature to verify the double-slit based beam splitter that we discuss in the following chapter.

Chapter 5

Verifying the double-slit beam splitter

To check the efficacy of the double-slit beam splitter that we constructed in chapter 3, we study the cross-correlation of the outputs. As the solutions of the Helmholtz equation are time-independent, the cross-correlation is modified such that the distinguishability parameter between the inputs is the angle of polarization [48] instead of the time-delay. Further, we concatenate two such double-slit beam splitters to construct a Mach-Zehnder interferometer.

5.1 Cross-correlation of the post-selected output fields

5.1.1 Modified correlation function

Let the field from source S_2 have a phase φ with respect to that from source S_1. Also, we rotate the polarization of source S_2 so that θ is the angle between the directions of polarizations of the fields from the two sources. When both the sources are turned on, port D_1 intercepts the vector superposition of fields from sources S_1 and S_2 through slit A_1. The integrated intensity in the post-selected mode on port D_1, i.e., $e_1(x, y; z_2)$ (see §3.3), is the projection of the vector sum of the fields

intercepted by the port, i.e.,

$$\begin{aligned}\|E_+(z_2,\theta,\varphi)\|^2 &\coloneqq \iint_{z_2} \mathrm{d}x\ \mathrm{d}y\ \ |E_+(x,y,z_2,\theta,\varphi)|^2 \\ &= \left|\left\langle e_1(z_2), E_1^{(1)}(z_2)\right\rangle\right|^2 + \left|\left\langle e_1(z_2), E_1^{(2)}(z_2)\right\rangle\right|^2 \\ &\quad + 2\mathrm{Re}\left\{\left\langle e_1(z_2), E_1^{(1)}(z_2)\right\rangle^* \left\langle e_1(z_2), E_1^{(2)}(z_2)\right\rangle\right\}\cos\varphi\cos\theta, \quad (5.1)\end{aligned}$$

where θ is the distinguishability parameter between the two sources. Similarly, the integrated intensity in the post-selected mode on port D_2 is calculated by projecting $E_-(x,y;z_2,\theta,\varphi)$ on to $e_2(x,y;z_2)$.

The cross-correlation between the two outputs as a function of θ is modified for time-independent fields as

$$C(\theta;z_2) \coloneqq \frac{\int \mathrm{d}\varphi\ p(\varphi)\,\|E_+(z_2,\theta,\varphi)\|^2\,\|E_-(z_2,\theta,\varphi)\|^2}{\int \mathrm{d}\varphi\ p(\varphi)\,\|E_+(z_2,\theta,\varphi)\|^2 \int \mathrm{d}\varphi\ p(\varphi)\,\|E_-(z_2,\theta,\varphi)\|^2} \quad (5.2)$$

which is the intensity-intensity correlation of the two output modes of the slice at $z = z_2$.

5.1.2 Numerical result

Now we show the result of the numerically calculated intensity-intensity cross-correlation of the post-selected outputs using Eq. (5.2) with

$$p(\varphi) = \frac{1}{2\pi}, \quad (5.3)$$

i.e., the relative phase between the two sources is uniformly random. Figure 5.1 shows the values of the correlation as a function of the distinguishability parameter, which in this case is the relative polarization angle θ between the two sources. The function that fits the result is

$$C_{50}(\theta) = 0.75 - 0.25\ \cos 2\theta, \quad (5.4)$$

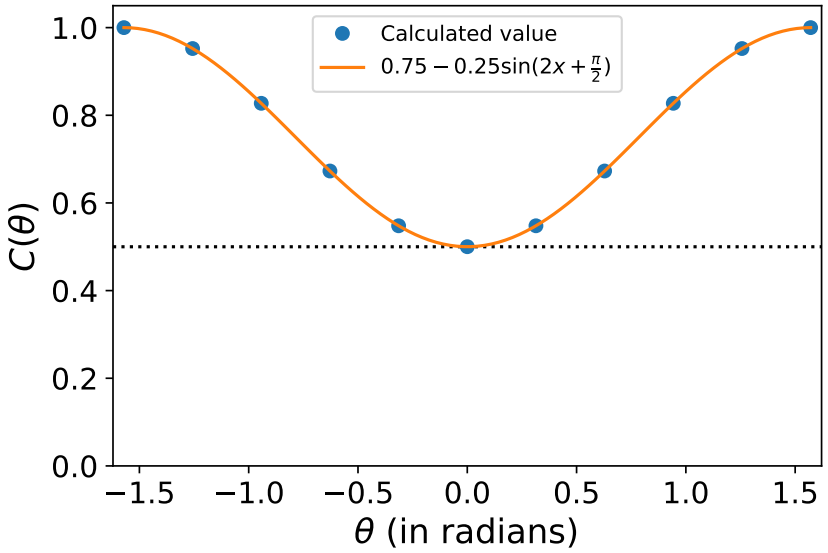

Figure 5.1: The intensity-intensity correlation of the output in the double-slit setup is calculated using Eq. (5.2) with φ chosen from the probability distribution in Eq. (G.2). As is the case with a regular cubic 50:50 beam splitter, the correlation shows a 50% dip. The minimum is for $\theta = 0$ when both the inputs are indistinguishable, and maximum for $\theta = \pi/2$ when they are completely distinguishable. Compare this with Fig. 5.2.

the visibility of which is 0.5.

On the other hand, for a 50:50 cubic beam splitter (with transfer matrix as in Eq. (2.44)), if the relative phase φ between the two sources is distributed uniformly over the interval $[0, 2\pi)$, the cross-correlation function shows a visibility of 0.5 as shown in Fig. 5.2 (see appendix G for more details on the correlation of the outputs of a cubic beam splitter). On comparing the variation of the correlation of the outputs of the double-slit setup with that of the cubic beam splitter, we confirm the beam splitter like behaviour of the double-slit setup [39].

For completeness, we discuss the 100% dip in the correlation by using a suitable probability distribution of phase. The visibility of the correlation is dependent on the probability distribution $p(\varphi)$. In particular, if

$$p(\varphi) = \frac{1}{2}\delta\left(\theta - \frac{\pi}{2}\right) + \frac{1}{2}\delta\left(\theta + \frac{\pi}{2}\right), \tag{5.5}$$

the correlation function shows a visibility of 1.0, as shown in Fig. 5.3. The function

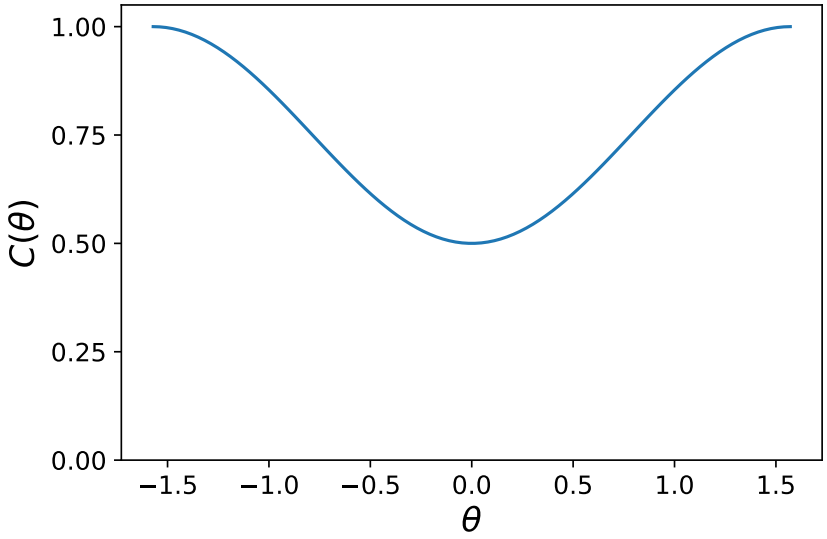

Figure 5.2: The cross-correlation function plotted as a function of the relative polarization angle θ between the input pulses, for a cubic beam splitter. The correlation is minimum when both the sources are indistinguishable, i.e., $\theta = 0$, and maximum when they are completely distinguishable, i.e., $\theta = \pi/2$. The detailed calculations are presented in appendix G

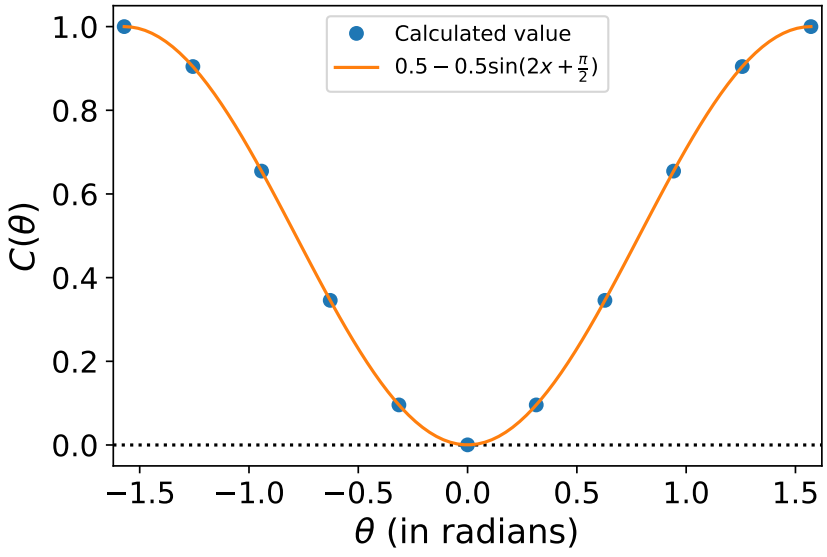

Figure 5.3: The intensity-intensity correlation of the output in the double-slit setup is calculated using Eq. (5.2) with φ chosen from the probability distribution is Eq. (5.5). In this case the correlation shows a dip of 100%. Although the fields are classical, a 100% dip or a Hong-Ou-Mandel like dip is achieved if the probability distribution of the relative phase between the inputs are chosen carefully.

that fits the result is

$$C_{100}(\theta) = 0.5 - 0.5 \ \cos 2\theta, \tag{5.6}$$

which shows that although the fields are classical, a 100% dip or a Hong-Ou-Mandel like dip is achieved if the probability distribution of the relative phase between the inputs are chosen carefully [41].

5.2 Effective Mach-Zehnder interferometer

The double-slit beam splitters, discussed in this work, can be concatenated to construct more sophisticated interferometers. As an example, Fig. 5.4 shows the schematic of an effective Mach-Zehnder interferometer (MZI) [30] made by concatenating two such double-slit modules.

The detectors behind ports D_1 and D_2 as in Fig. 3.2 are removed, and these ports now serve as inputs to the second double-slit module. The fields from these ports get diffracted by slits A_1' and A_2' and reach the output ports D_1' and D_2', of the second double-slit module behind each of which is a detector.

A phase shifter (see appendix H on how the phase-shifter is implemented numerically) causes an interference pattern at the output ports D_1' and D_2' as the phase, say α is changed in one of the arms of the MZI. The interference pattern obtained is used as a signature to verify the double-slit based MZI.

The MZI is essentially a concatenation of two beam splitters. If both the beam splitters are identical 50:50 splitters with transfer matrix in Eq. (2.44) and the phase in one arm, say α is set to zero (the arm lengths are considered equal), the transfer matrix for the MZI is [30]

$$\frac{1}{2}\begin{pmatrix} 1 & \mathrm{i} \\ \mathrm{i} & 1 \end{pmatrix}\begin{pmatrix} 1 & \mathrm{i} \\ \mathrm{i} & 1 \end{pmatrix} = \begin{pmatrix} 0 & i \\ i & 0 \end{pmatrix}, \tag{5.7}$$

and therefore the transfer matrix for the double-slit MZI should be close to this.

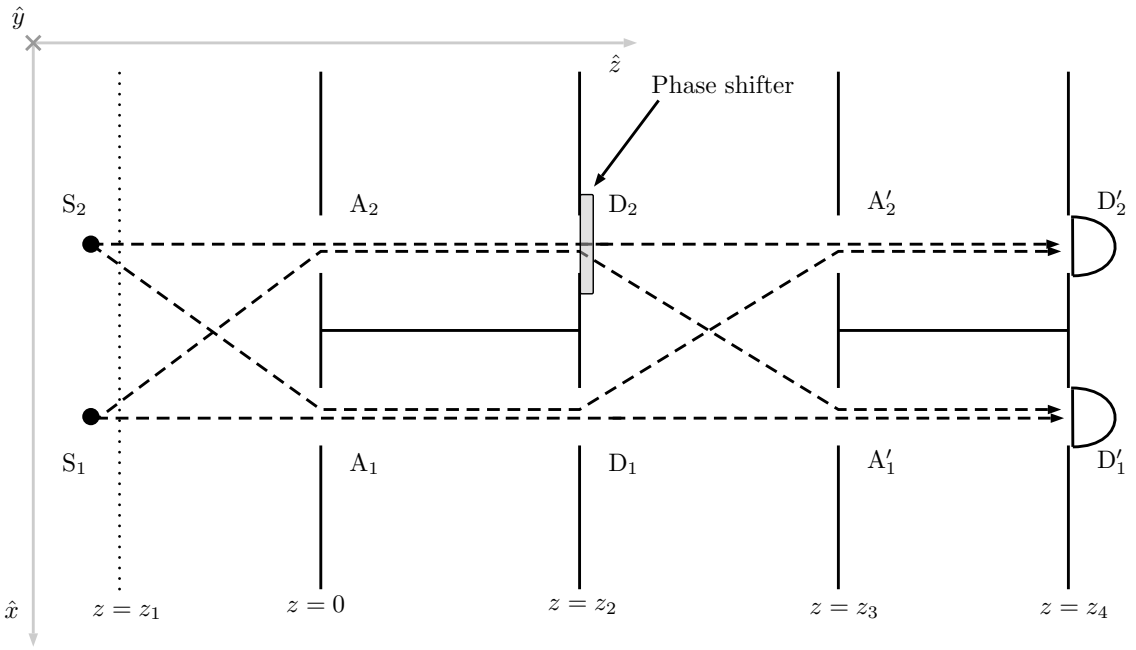

Figure 5.4: Using two double-slit setups a Mach-Zehnder interferometer is constructed by concatenating them such that both are aligned centre-to-centre and parallel to each other. The output ports D_1 and D_2 of the first double-slit beam splitter serve as the inputs for the second one. The two detectors are placed behind the output ports D_1' and D_2' of the second double-slit setup. A phase shifter is placed at the output port D_2 which changes the phase of the field from that port by α.

We use a similar approach as that used for the double-slit setup, to find the transfer matrix for the effective MZI, with the output slice at z_4 (as shown in Fig. 5.4).

5.2.1 The interference pattern of MZI

Here we show the interference pattern at the output of the double-slit based MZI, as shown in Fig. 5.4. Similar to the case of one double-slit setup, adopting the Fraunhofer approximation and calculating the integrated intensities at the two detectors for different values of α yields an interference pattern as shown in Fig. 5.5. Such an interference pattern is the signature of an MZI. The curves that fit the resultant integrated intensities at ports D_1' and D_2' are approximately

$$I_1(\alpha) = 2.41 \times 10^{-8} \left(1 - \sin\left(x - 2.45 \times 10^{-4}\right)\right), \tag{5.8}$$

$$I_2(\alpha) = 2.41 \times 10^{-8} \left(1 + \sin\left(x + 2.45 \times 10^{-4}\right)\right), \tag{5.9}$$

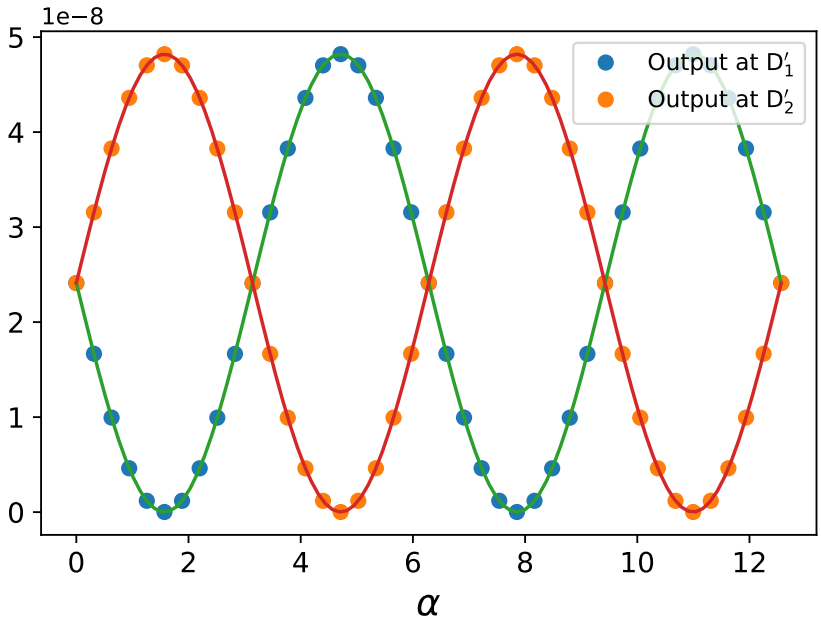

Figure 5.5: Interference pattern at the output of the MZI made of concatenated double-slit beam splitters.

respectively. The visibility V_{MZI} of both the curves is

$$V = 99.94\%, \tag{5.10}$$

which means that the effective MZI using double-slit modules closely emulates an MZI with cubic beam splitters. Therefore, the transfer matrix formalism applied to the setup in Fig. 5.4 should yield the transformation in Eq. (5.7).

5.2.2 Transfer matrix for the double-slit MZI

Using the method outlined in §3, the transfer matrix for the double-slit Mach-Zehnder in Fig. 5.4 is

$$T_{\mathrm{MZ}} \approx \mathrm{e}^{0.08\pi\mathrm{i}} \begin{pmatrix} 0.255 & 3.903\ \mathrm{e}^{0.39\pi\mathrm{i}} \\ 3.903\ \mathrm{e}^{0.39\pi\mathrm{i}} & 0.255 \end{pmatrix} \times 10^{-7}, \tag{5.11}$$

which after polar decomposition yields

$$U_{\mathrm{MZ}} \approx \begin{pmatrix} 0.061 & 0.998\ \mathrm{i} \\ 0.998\ \mathrm{i} & 0.061 \end{pmatrix} \times \mathrm{e}^{-0.03\pi\mathrm{i}}, \tag{5.12}$$

$$P_{\mathrm{MZ}} \approx \begin{pmatrix} 3.910 & 0.088 \\ 0.088 & 3.910 \end{pmatrix} \times 10^{-7}. \tag{5.13}$$

Up to a global phase the transfer matrix method successfully reveals the underlying unitary operator for the double-slit Mach-Zehnder which can be checked by comparing Eqs. (5.7) and (5.12).

5.3 Extending to three dimensions

A beam splitter is a two-input-two-output device which, as discussed above, can be effectively constructed using double-slit diffraction. However, one of the key potential uses of slit-diffraction and the framework outlined in this work is extension to higher dimensions. As an example, Fig. 5.6 shows a triple-slit setup in which a third source S_3 is placed at $(-3d/2, 0, -L)$, a slit A_3 centered at $(-3d/2, 0, 0)$ and a detector D_3 centered at $(-3d/2, 0, L)$. Similar to the double-slit case, the transfer matrix approach can be applied to this system.

5.3.1 The input and output modes for triple-slit

For the triple-slit setup, three Haar scaling functions are chosen as post-selected input modes and three for the post-selected output modes. According to the positions of the detectors (and slits) these modes are

$$e_1(x, y; z_1) \coloneqq g_1(x, y; z_1, -2, 2, 0), \tag{5.14}$$

$$e_2(x, y; z_1) \coloneqq g_1(x, y; z_1, -2, -3, 0), \tag{5.15}$$

$$e_3(x, y; z_1) \coloneqq g_1(x, y; z_1, -2, -8, 0), \tag{5.16}$$

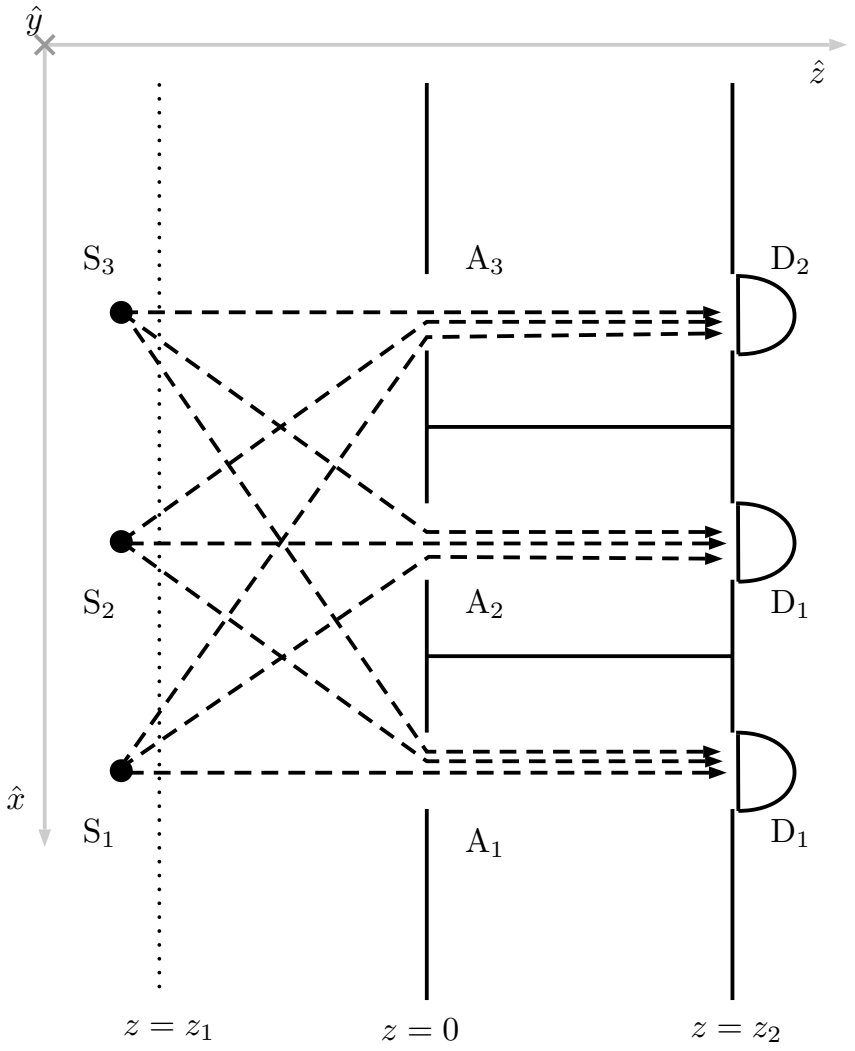

Figure 5.6: Schematic of a triple-slit setup constructed in a similar way as the double-slit setup in Fig. 3.2, by adding a source, slit and detector to the latter.

and similarly for slice at z_2.

Like in the case of two slits, the post-selected input and output will have a 3-dimensional column representation similar to those in Eqs. (3.24) and (3.28). The equation for the effective transfer matrix is

$$T(z_2, z_1)\begin{pmatrix} \boldsymbol{X}^{(1)}(z_1) & \boldsymbol{X}^{(2)}(z_1) & \boldsymbol{X}^{(3)}(z_1) \end{pmatrix} = \begin{pmatrix} \boldsymbol{Y}^{(1)}(z_2) & \boldsymbol{Y}^{(2)}(z_2) & \boldsymbol{Y}^{(3)}(z_2) \end{pmatrix}, \tag{5.17}$$

where the superscripts denote the source that is turned on.

5.3.2 Transfer matrix for the triple-slit setup

We have verified our formalism using a double-slit setup and by comparing it to a well-known optical device, the cubic beam splitter. Here, we apply the transfer matrix formalism to get the post-selected transfer matrix of a triple-slit setup, demonstrating the extensibility of the framework to higher-dimensional systems.

The effective 3×3 transfer matrix for the triple-slit setup in Fig. 5.6, with respect to the post-selected modes discussed in §**??** is

$$T_3(z_2,z_1) \approx \mathrm{e}^{-\mathrm{i}0.16\pi} \begin{pmatrix} 0.636 & 0.629\ \mathrm{i} & 0.594 \\ 0.626\ \mathrm{i} & 0.637 & 0.626\ \mathrm{i} \\ 0.594 & 0.629\ \mathrm{i} & 0.636 \end{pmatrix} \times 10^{-3}, \tag{5.18}$$

where subscript 3 denotes that the transfer matrix is for a triple-slit setup. The polar decomposition of the 3×3 transfer matrix results in

$$U_3(z_2,z_1) \approx \frac{\mathrm{e}^{-\mathrm{i}0.15\pi}}{\sqrt{3}} \begin{pmatrix} 1.493 & 0.844\ \mathrm{i} & -0.242 \\ 0.844\ \mathrm{i} & 1.255 & 0.844\ \mathrm{i} \\ -0.242 & 0.844\ \mathrm{i} & 1.493 \end{pmatrix}, \tag{5.19}$$

$$P_3(z_2,z_1) \approx \begin{pmatrix} 0.772 & 0.146\ \mathrm{i} & 0.730 \\ -0.146\ \mathrm{i} & 1.075 & -0.146\ \mathrm{i} \\ 0.730 & 0.146\ \mathrm{i} & 0.772 \end{pmatrix} \times 10^{-3}, \tag{5.20}$$

which reveals the underlying unitary transformation along with the losses captured by the Hermitian component.

By further similarly increasing the number of slits, even higher-dimensional transfer matrices can be realized using slit-diffraction. Therefore, unlike with four-port devices like beam splitters, which have to be concatenated to implement higher-dimensional transformations, a single N-slit setup can be used for an N-dimensional transformation. This way of implementing higher-dimensional transfer matrices should prove to be easier than that using orbital angular momentum of light, be-

cause of the practical limits on obtaining high OAM states [7].

Chapter 6

Conclusion and discussion

6.1 Summary

A postselected unitary representation of slit-diffraction is achieved by projecting the solutions of the Helmholtz equation on a two-dimensional plane and finding a transfer matrix that maps one slice to another. The Haar wavelets and scaling functions are used as orthonormal modes that span the slice on each plane. From the infinite set of modes, two input and two output modes are postselected depending on the area and position of the detectors. The non-unitary transfer matrix is polar decomposed to reveal the underlying unitary transformation and a Hermitian component that captures the losses. Using this approach, a double-slit setup, with appropriate modification, is effectively a 54:46 beam splitter. To verify the beam splitter, we study the correlation between the postselected outputs.

As a complete characterization of a linear interferometer can be done by measuring the one- and two-photon interference of its outputs, we find a bridge between the latter and the classical correlation of classical fields by using the semiclassical theory of photoelectric detection. As a part of this process, we also show that the Hong-Ou-Mandel effect, which is considered a signature of the quantum behaviour of light, can be simulated using classical pulses. Moreover, we show that wave-particle complementarity is the authentic signature of photons. The classical equivalent of one- and two-photon interference helps connect the classical description of slit diffraction

with the unitary description of quantum interferometry and quantum gates.

The beam splitter behaviour of the double-slit setup is verified by calculating the intensity-intensity cross-correlation of the outputs and getting a Hong-Ou-Mandel like variation. Two such double-slit beam splitters are concatenated to construct a Mach-Zehnder interferometer showing that sophisticated interferometers can be constructed using slit based diffraction. Similar to a double-slit setup, a higher number of slits can be used to construct a multi-input-multi-output device, an example of which is shown by finding the postselected transfer matrix for a triple-slit setup. The future work involves quantizing the fields and making a quantum version of slit-diffraction-based interferometers, which can be used for implementing QIP protocols.

6.2 Scope of research

Quantum diffraction interferometry

In this thesis, we have shown that a double slit, with carefully chosen dimensions, is effectively a beam splitter. The transfer matrix of the double-slit depends on its geometrical properties like the sizes and positions of the sources, slits and detectors. The interesting problem is to realize other transfer matrices by changing these properties. Similarly, other transfer matrices can be realized by concatenation of multiple double slits (like in the case of Mach-Zehnder interferometer) and also by increasing the number of slits to realize higher-dimensional transfer matrices. The classical treatment will give an intuition about how to design specific quantum gates once the fields are quantized, and to construct a complete set of gates for universal quantum information processing.

The real advantage and relevance of this formalism will come through with the quantum treatment of the same. Therefore the future direction in this research is towards dealing with quantized light and getting a double-slit beam splitter with photons in postselected modes. Moreover, extending to higher-dimensional will

result in a platform for higher-dimensional quantum information processing (QIP).

Although the decomposition of any N-dimensional unitary operator in terms of beam splitters and phase shifters provides a protocol to realize higher-dimensional QIP, realizing the same using multiple slits will facilitate miniaturization of the interferometers and also reduce the number of components required, unleashing the true advantage of slit based interferometers.

The classical-quantum boundary

In the quest for tools to characterize the double-slit beam splitter, we came across an interesting result of Hong-Ou-Mandel like effect with the classical description of light. We have shown that unlike the folklores, which say that Hong-Ou-Mandel effect is a purely quantum phenomenon and cannot be explained using any classical or semiclassical theory, can indeed be simulated using the classical description of light. Moreover, the true quantum behaviour lies in the wave-particle duality of photons that is not exhibited by classical light. This results in a refined boundary between the classical and quantum nature of light. This motivated exploring other signatures of the quantumness of light. Exhaustive comparisons between the quantum and classical descriptions of light are discussed by D. N. Klyshko [49, 50], and W. E. Lamb Jr. [51], for example.

A closer look at the classical-quantum boundaries has applications beyond intellectual satiation. The field of quantum information and computing is rapidly growing owing to the predicted advantages it has over classical computation. However, it cannot be asserted whether a quantum computer will have a significant advantage, partly because there may be a classical algorithm that we have not found. Mostly, the confidence in a quantum algorithm comes from the fact that it uses one or more effects that are signatures of quantum behaviour and have no counterparts in the classical regime. Therefore, it is necessary to refine the boundary between classical and quantum behaviour.

Appendix A

Green's function of the Helmholtz equation

Here we will calculate the Green's function for the Helmholtz equation in free-space. We consider the three-dimensional case here, and finding the Green's function for other dimensionalities follows the same approach. First we make some reasonable assumptions for simplification. Because of the homogeneity of free-space we conclude that the Green's function is a function of $\boldsymbol{r}-\boldsymbol{r}'$. We assume that the free-space Green's function has a Fourier transform and transform the Green's function equation as

$$\left(\nabla'^2 + k^2\right) \iiint \frac{\mathrm{d}^3\boldsymbol{p}}{(2\pi)^3}\, \mathrm{e}^{\mathrm{i}\boldsymbol{p}\cdot\boldsymbol{r}}\, \tilde{G}(\boldsymbol{p}) = \iiint \frac{\mathrm{d}^3\boldsymbol{p}}{(2\pi)^3}\, \mathrm{e}^{\mathrm{i}\boldsymbol{p}\cdot\boldsymbol{r}}, \tag{A.1}$$

where we use the fact that the Fourier transform of one is the Dirac-Delta function. As the differential operator on the left-hand-side (LHS) is independent of the variable $\boldsymbol{p}$, it can be taken inside the integration. Moreover, as the set of functions $\mathrm{e}^{\mathrm{i}\boldsymbol{p}\cdot(\boldsymbol{r}-\boldsymbol{r}')}$ for all $\boldsymbol{p}$ forms an orthogonal basis, its coefficients can be matched on the LHS and

RHS, yielding,

$$(k^2 - p^2)\tilde{G}(\boldsymbol{p}) = 1 \tag{A.2}$$

$$\tilde{G}(\boldsymbol{p}) = \frac{-1}{p^2 - k^2}, \tag{A.3}$$

which can be inverse-Fourier-transformed to get the Green's function, i.e.,

$$G(\boldsymbol{r} - \boldsymbol{r}') = \frac{-1}{(2\pi)^3} \iiint \mathrm{d}^3\boldsymbol{p}\ \frac{\mathrm{e}^{\mathrm{i}\boldsymbol{p}\cdot(\boldsymbol{r}-\boldsymbol{r}')}}{p^2 - k^2}. \tag{A.4}$$

It is convenient to solve the integral in three-dimensional spherical coordinate system (because the integral is spherically symmetric). In spherical coordinate system, $\mathrm{d}^3\boldsymbol{p} = \mathrm{d}p\ \mathrm{d}(\cos\theta)\ \mathrm{d}\varphi\ p^2$, where we choose θ to be the angle between $\boldsymbol{p}$ and $\boldsymbol{r} - \boldsymbol{r}'$ and φ as the azimuthal angle. This yields

$$G(\boldsymbol{r} - \boldsymbol{r}') = \frac{-1}{(2\pi)^3} \int_0^{\infty} \mathrm{d}p\ p^2 \int_1^{-1} \mathrm{d}(\cos\theta) \int_0^{2\pi} \mathrm{d}\varphi\ \frac{\mathrm{e}^{\mathrm{i}pr\cos\theta}}{p^2 - k^2}, \tag{A.5}$$

where I have defined $r = |\boldsymbol{r} - \boldsymbol{r}'|$. The integration over φ and θ yield

$$G(\boldsymbol{r} - \boldsymbol{r}') = \frac{-1}{(2\pi)^3}\ 2\pi \int_0^{\infty} \mathrm{d}p\ p^2 \int_1^{-1} \mathrm{d}(\cos\theta)\ \frac{\mathrm{e}^{\mathrm{i}pr\cos\theta}}{p^2 - k^2} \tag{A.6}$$

$$= \frac{-1}{(2\pi)^3 \mathrm{i}r}\ 2\pi \int_0^{\infty} \mathrm{d}p\ p \int_{\mathrm{i}pr}^{-\mathrm{i}pr} \mathrm{d}(\mathrm{i}pr\cos\theta)\ \frac{\mathrm{e}^{\mathrm{i}pr\cos\theta}}{p^2 - k^2} \tag{A.7}$$

$$= \frac{-\mathrm{i}}{(2\pi)^2 r}\ \int_0^{\infty} \mathrm{d}p\ p\ \frac{\mathrm{e}^{\mathrm{i}pr} - \mathrm{e}^{-\mathrm{i}pr}}{p^2 - k^2}. \tag{A.8}$$

Note that the integrand on the RHS is an even function of p and therefore we can write the integration as

$$G(r) = \frac{-\mathrm{i}}{2(2\pi)^2 r}\ \int_{-\infty}^{\infty} \mathrm{d}p\ p\ \frac{\mathrm{e}^{\mathrm{i}pr} - \mathrm{e}^{-\mathrm{i}pr}}{p^2 - k^2}, \tag{A.9}$$

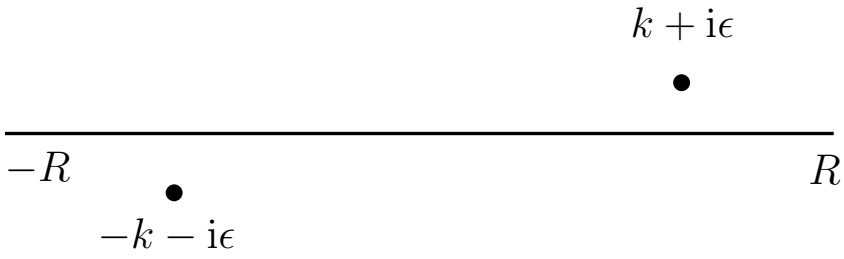

Figure A.1: The real number line shown in the interval $(-R, R)$. The two poles at $z = +|k|$ and $z = -|k|$ are pushed above and below the real line respectively. The purpose of doing this is to avoid the pole being on the contour line.

and perform a contour integral. Consider a complex integral

$$G\left(\boldsymbol{r} - \boldsymbol{r}'\right) = \frac{-\mathrm{i}}{2(2\pi)^2 r} \int \mathrm{d}z \; z \; \frac{\mathrm{e}^{\mathrm{i}zr} - \mathrm{e}^{-\mathrm{i}zr}}{z^2 - k^2}, \tag{A.10}$$

the poles of which are on the real line, i.e., $z = k$ and $z = -k$. We use the fact that $\lim_{\epsilon \to 0^+} k + \mathrm{i}\epsilon = k$ and displace the poles from the real line. Let us assume for now that $k > 0$. The effect of displacing the the poles is shown in figure A.1. The expression for the Green's function becomes

$$G\left(\boldsymbol{r} - \boldsymbol{r}'\right) = \lim_{\epsilon \to 0^+} \frac{-\mathrm{i}}{2(2\pi)^2 r} \int \mathrm{d}z \; z \; \frac{\mathrm{e}^{\mathrm{i}zr} - \mathrm{e}^{-\mathrm{i}zr}}{(z + k + \mathrm{i}\epsilon)(z - k - \mathrm{i}\epsilon)}, \tag{A.11}$$

which can be solved using contour integration. As $r > 0$, the contour must be closed in the upper-half-plane (UHP) for the term $\mathrm{e}^{\mathrm{i}zr}$ as shown in figure A.2. The closing curve C is a semi-circle of radius R. The term $\mathrm{e}^{\mathrm{i}zr}$ on C becomes an exponentially decaying term which becomes asymptotically zero as $R \to \infty$. Therefore, the only contribution to the integration along the entire closed curve comes from the real line $\lim_{R \to \infty} (-R, R)$. From Cauchy's integral theorem we have

$$\int \mathrm{d}z \; z \; \frac{\mathrm{e}^{\mathrm{i}zr}}{(z + k + \mathrm{i}\epsilon)(z - k - \mathrm{i}\epsilon)} = 2\pi\mathrm{i} \; (k + \mathrm{i}\epsilon) \; \frac{\mathrm{e}^{\mathrm{i}(k+\mathrm{i}\epsilon)r}}{2(k + \mathrm{i}\epsilon)} \tag{A.12}$$

$$= \pi\mathrm{i} \; \mathrm{e}^{\mathrm{i}(k+\mathrm{i}\epsilon)r} \tag{A.13}$$

With similar reasoning, the contour for the term with $\mathrm{e}^{\mathrm{i}zr}$ is in the lower-half-plane (LHP) as shown in figure A.3. and the integral

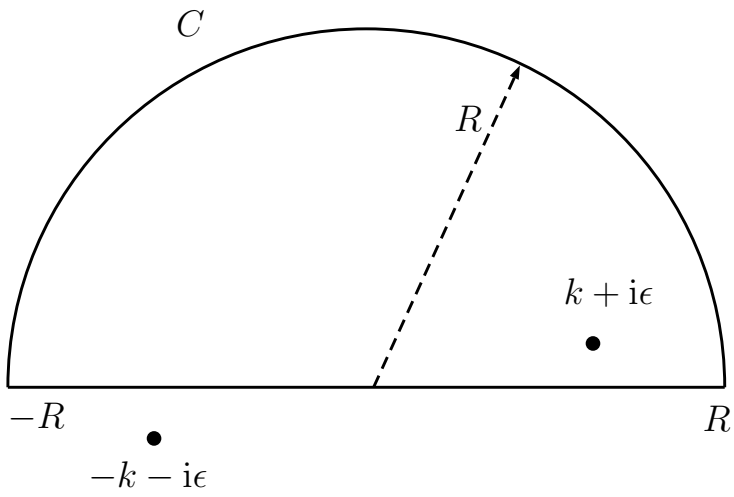

Figure A.2: For the term involving $\mathrm{e}^{\mathrm{i}zr}$ the contour is closed in the UHP so that the integral along the semi-circle vanishes as $R \to \infty$, leaving the only contribution to the integral being from the integral along the real line.

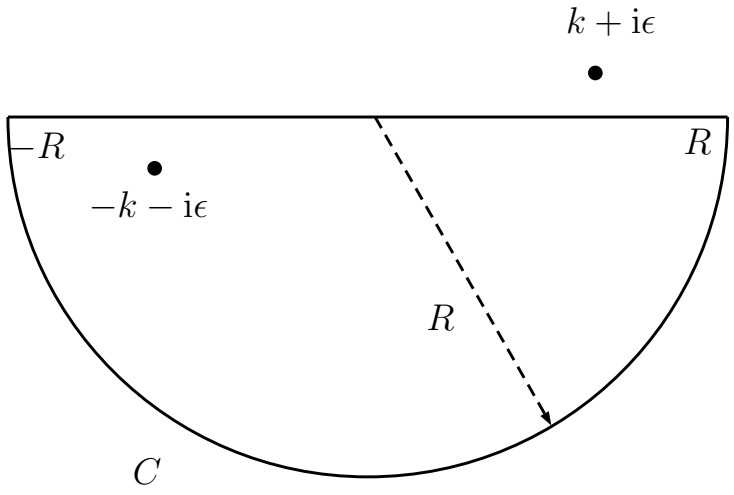

Figure A.3: For the term involving $\mathrm{e}^{-\mathrm{i}zr}$ the contour is closed in the LHP so that the integral along the semi-circle vanishes as $R \to \infty$, leaving the only contribution to the integral being from the integral along the real line.

Figure A.4: In case of the advanced Green's function for which $k < 0$, the poles get shifted in directions opposite to that in the case of the retarded Green's function as shown in figure A.1.

$$\int \mathrm{d}z\ z\ \frac{\mathrm{e}^{-\mathrm{i}zr}}{(z+k+\mathrm{i}\epsilon)(z-k-\mathrm{i}\epsilon)} = -\,2\pi\mathrm{i}\ (-k-\mathrm{i}\epsilon)\ \frac{\mathrm{e}^{-\mathrm{i}(-k-\mathrm{i}\epsilon)r}}{2(-k-\mathrm{i}\epsilon)} \tag{A.14}$$

$$= -\,\pi\mathrm{i}\ \mathrm{e}^{\mathrm{i}(k+\mathrm{i}\epsilon)r} \tag{A.15}$$

on combining both the terms, we get the Green's function

$$G_{\mathrm{ret}}\,(r) = \lim_{\epsilon\to 0^+} \frac{-\mathrm{i}}{2(2\pi)^2 r}\ 2\pi\mathrm{i}\mathrm{e}^{\mathrm{i}(k+\mathrm{i}\epsilon)r} \tag{A.16}$$

$$= \frac{1}{4\pi}\ \frac{\mathrm{e}^{\mathrm{i}|k|r}}{r}, \tag{A.17}$$

where the subscript denotes the fact that $k > 0$ and the corresponding Green's function is called the retarded Green's function.

On the other hand, if $k < 0$, the poles shift in the opposite directions as before, as shown in figure A.4. Closing the contours in the same way as before, we get

$$G_{\mathrm{adv}}\,(r) = \frac{1}{4\pi}\ \frac{\mathrm{e}^{-\mathrm{i}|k|r}}{r}, \tag{A.18}$$

which is called the advanced Green's function. Physically, the retarded Green's functions captures the field propagating in the forward direction, and the advanced Green's function on the other hand captures the backward propagating wave.

Appendix B

Solution for slit diffraction

Consider an opaque (infinite) plane with a rectangular aperture in it, placed at $z = z_s$ (refer to Fig. 2.10). Let the position of the center of the slit be $\boldsymbol{r}_s$. All the other boundaries of the system are at infinity (for simplicity). A point-like source of electromagnetic radiation is placed at position $\boldsymbol{r}_f$. Assuming that the time-dependence of the source is harmonic, the field from the source will satisfy the Helmholtz equation (Eq. (2.5)). To find the field diffracted by the slit, we solve the Helmholtz equation for this system in two steps. First we find the field on the slit-plane, and then from the field on the slit-plane, find the diffracted field.

For the first step, consider the infinite volume enclosed by the surfaces $x = \pm\infty$, $y = \pm\infty$, $z = \pm\infty$. Adopting Kirchoff's approximation, we impose that the field on the opaque part of the slit-plane is zero. The field on the boundary is also zero, because of the reasonable imposition that the field at a point infinitely far from the source is zero.

Using the formal solution of the Helmholtz equation, i.e., Eq. (2.8) the field within the area of the slit is

$$E(\boldsymbol{r}) = G(\boldsymbol{r}, \boldsymbol{r}_f), \tag{B.1}$$

and zero everywhere else on the slit-plane. Here we only use the retarded Green's function as in Eq. (A.16). The field within the slit can now be used to find the diffracted at any point of interest P.

Consider the semi-infinite volume enclosed by surfaces $z = z_s$, $z = +\infty$, $x = \pm\infty$ and $y = \pm\infty$. There is no source within this volume so the volume term in Eq. (2.8) vanishes within this volume. Moreover, the only contribution to the surface term is from the slit-plane as the other parts of the surfaces are at infinity. Therefore, the diffracted field at a point P positioned at $\boldsymbol{r}$ is

$$E(\boldsymbol{r}) = \int\limits_{z=\boldsymbol{r}_s\cdot\hat{\boldsymbol{z}}} \mathrm{d}^2\boldsymbol{r}'\ \hat{\boldsymbol{z}}\cdot\left(G(\boldsymbol{r}',\boldsymbol{r}_f)\nabla' G(\boldsymbol{r},\boldsymbol{r}') - G(\boldsymbol{r},\boldsymbol{r}')\nabla' G(\boldsymbol{r}',\boldsymbol{r}_f)\right), \tag{B.2}$$

which depends only on the field over the area of the slit. This expression can be simplified by adopting the far-field and small slit approximations as discussed in the following subsections.

B.1 Far field approximation

An important property of the Green's function is its symmetry under exchange of arguments, i.e.,

$$G(\boldsymbol{r}_2,\boldsymbol{r}_1) = G(\boldsymbol{r}_1,\boldsymbol{r}_2), \tag{B.3}$$

which follows directly from Eq. (A.16). Also

$$\begin{aligned}\nabla_2 G(\boldsymbol{r}_2,\boldsymbol{r}_1) &= -\frac{1}{4\pi}\,\frac{\mathrm{i}k\mathrm{e}^{\mathrm{i}k|\boldsymbol{r}_2-\boldsymbol{r}_1|}}{|\boldsymbol{r}_2-\boldsymbol{r}_1|} - \frac{\mathrm{e}^{\mathrm{i}k|\boldsymbol{r}_2-\boldsymbol{r}_1|}}{|\boldsymbol{r}_2-\boldsymbol{r}_1|^2}\,\nabla_2|\boldsymbol{r}_2-\boldsymbol{r}_1| \\ &= -\frac{1}{4\pi}\,\frac{\mathrm{e}^{\mathrm{i}k|\boldsymbol{r}_2-\boldsymbol{r}_1|}}{|\boldsymbol{r}_2-\boldsymbol{r}_1|}\left(\mathrm{i}k - \frac{1}{|\boldsymbol{r}_2-\boldsymbol{r}_1|}\right)\,\frac{\boldsymbol{r}_2-\boldsymbol{r}_1}{|\boldsymbol{r}_2-\boldsymbol{r}_1|},\end{aligned} \tag{B.4}$$

which means that $\nabla_1 G(\boldsymbol{r}_2,\boldsymbol{r}_1) = -\nabla_2 G(\boldsymbol{r}_2,\boldsymbol{r}_1)$. The far-field approximation is applied by assuming that $|\mathrm{i}k| >> \frac{1}{|\boldsymbol{r}_2-\boldsymbol{r}_1|}$, which yields

$$\nabla_2 G(\boldsymbol{r}_2,\boldsymbol{r}_1) \approx \mathrm{i}k\ G(\boldsymbol{r}_2,\boldsymbol{r}_1)\,\frac{\boldsymbol{r}_2-\boldsymbol{r}_1}{|\boldsymbol{r}_2-\boldsymbol{r}_1|}. \tag{B.5}$$

With this approximation, Eq. (B.2) simplifies to

$$E(\boldsymbol{r}) = -\mathrm{i}k \int_{\mathcal{S}} \mathrm{d}^2\boldsymbol{r}'\ G(\boldsymbol{r}', \boldsymbol{r}_f) G(\boldsymbol{r}, \boldsymbol{r}')\ \left(\frac{z - z'}{|\boldsymbol{r} - \boldsymbol{r}'|} + \frac{z' - z_f}{|\boldsymbol{r}' - \boldsymbol{r}_f|} \right). \tag{B.6}$$

Note if the point of interest P is far from the slit-plane but very close enough to the line that runs perpendicular to the slit through its center, i.e., $|\boldsymbol{r} - \boldsymbol{r}'| \approx z - z'$, and similarly for the source and the slit, then the expression for the diffracted field reduces to

$$E(\boldsymbol{r}) = -2\mathrm{i}k \int_{\mathcal{S}} \mathrm{d}^2\boldsymbol{r}'\ G(\boldsymbol{r}', \boldsymbol{r}_f) G(\boldsymbol{r}, \boldsymbol{r}'), \tag{B.7}$$

which is the mathematical representation of the Huygens principle which says that every point on the slit can be considered a source of wave.

Further simplification can be made by assuming that the size of the slit is much smaller than the distance between the slit and point P. The quantification of such approximations is done by calculating the Fresnel number for the system which is defined as

$$F = \frac{w^2}{\lambda L}, \tag{B.8}$$

where w is the width of the slit (or the width of the longer side of the rectangle), L is the distance between the center of the slit and the point of interest, P in this case, and

$$\lambda = \frac{2\pi}{k}, \tag{B.9}$$

i.e., the wavelength of the light. When

$$F \ll 1, \tag{B.10}$$

the solution of the Helmholtz equation is called the far-field or Fraunhofer solution.

In the following section, we consider the the small slit approximation to further simplify the solution.

B.2 Small slit approximation

Let $\boldsymbol{r}_s$ be the center of the slit with a width very small compared with its distance from the point of detection such that Eq. (B.10) is satisfied. A position within the area of the slit can be written as $\boldsymbol{r}' = \boldsymbol{r}_s + \boldsymbol{\Delta}_s$. Therefore,

$$G(\boldsymbol{r}', \boldsymbol{r}_f) = -\frac{1}{4\pi} \frac{\mathrm{e}^{\mathrm{i}k|\boldsymbol{r}_s - \boldsymbol{r}_f + \boldsymbol{\Delta}_s|}}{|\boldsymbol{r}_s - \boldsymbol{r}_f + \boldsymbol{\Delta}_s|}, \tag{B.11}$$

where the small slit approximation is applied as $|\boldsymbol{\Delta_s}|/|\boldsymbol{r}_s - \boldsymbol{r}_f| \ll 1$ so that

$$\begin{aligned}
|\boldsymbol{r}_s - \boldsymbol{r}_f + \boldsymbol{\Delta}_s| &= \sqrt{|\boldsymbol{r}_s - \boldsymbol{r}_f|^2 + |\boldsymbol{\Delta}_s|^2 + 2\boldsymbol{\Delta}_s \cdot (\boldsymbol{r}_s - \boldsymbol{r}_f)} \\
&= |\boldsymbol{r}_s - \boldsymbol{r}_f| \sqrt{1 + \frac{|\boldsymbol{\Delta}_s|^2}{|\boldsymbol{r}_s - \boldsymbol{r}_f|^2} + 2\boldsymbol{\Delta}_s \cdot \frac{(\boldsymbol{r}_s - \boldsymbol{r}_f)}{|\boldsymbol{r}_s - \boldsymbol{r}_f|^2}} \\
&\approx |\boldsymbol{r}_s - \boldsymbol{r}_f| \sqrt{1 + 2\boldsymbol{\Delta}_s \cdot \frac{(\boldsymbol{r}_s - \boldsymbol{r}_f)}{|\boldsymbol{r}_s - \boldsymbol{r}_f|^2}} \\
&\approx |\boldsymbol{r}_s - \boldsymbol{r}_f| \left(1 + \boldsymbol{\Delta}_s \cdot \frac{(\boldsymbol{r}_s - \boldsymbol{r}_f)}{|\boldsymbol{r}_s - \boldsymbol{r}_f|^2}\right).
\end{aligned} \tag{B.12}$$

Furthermore, for far-field and small slit

$$\frac{1}{|\boldsymbol{r}' - \boldsymbol{r}_f|} \approx \frac{1}{|\boldsymbol{r}_s - \boldsymbol{r}_f|} \tag{B.13}$$

which results in

$$\begin{aligned}
G(\boldsymbol{r}', \boldsymbol{r}_f) &= -\frac{1}{4\pi} \frac{\mathrm{e}^{\mathrm{i}k|\boldsymbol{r}_s - \boldsymbol{r}_f|}}{|\boldsymbol{r}_s - \boldsymbol{r}_f|} \mathrm{e}^{\mathrm{i}k\boldsymbol{\Delta}_s \cdot \frac{\boldsymbol{r}_s - \boldsymbol{r}_f}{|\boldsymbol{r}_s - \boldsymbol{r}_f|}} \\
&= G(\boldsymbol{r}_s, \boldsymbol{r}_f)\, \mathrm{e}^{\mathrm{i}k\boldsymbol{\Delta}_s \cdot \frac{\boldsymbol{r}_s - \boldsymbol{r}_f}{|\boldsymbol{r}_s - \boldsymbol{r}_f|}}.
\end{aligned} \tag{B.14}$$

Similarly,

$$G(\boldsymbol{r},\boldsymbol{r}') = G(\boldsymbol{r},\boldsymbol{r}_s)\ \mathrm{e}^{-\mathrm{i}k\boldsymbol{\Delta}_s\cdot\frac{\boldsymbol{r}-\boldsymbol{r}_s}{|\boldsymbol{r}-\boldsymbol{r}_s|}}, \tag{B.15}$$

and using this approximation in Eq. (B.6) we get

$$\begin{aligned} E(\boldsymbol{r}) = &-\mathrm{i}k\int_{\mathcal{S}} \mathrm{d}^2\boldsymbol{\Delta}_s\ G(\boldsymbol{r},\boldsymbol{r}_s)\ G(\boldsymbol{r}_s,\boldsymbol{r}_f)\ \mathrm{e}^{-\mathrm{i}k\boldsymbol{\Delta}_s\cdot\left(\frac{\boldsymbol{r}-\boldsymbol{r}_s}{|\boldsymbol{r}-\boldsymbol{r}_s|}-\frac{\boldsymbol{r}_s-\boldsymbol{r}_f}{|\boldsymbol{r}_s-\boldsymbol{r}_f|}\right)} \\ &\times\left(\frac{z-z_s}{|\boldsymbol{r}-\boldsymbol{r}_s|}+\frac{z_s-z_f}{|\boldsymbol{r}_s-\boldsymbol{r}_f|}\right). \end{aligned} \tag{B.16}$$

For a rectangular slit w_x wide along x and w_y along y, the integral is a sinc function and the final expression for the field of the slice is

$$\begin{aligned} E(\boldsymbol{r}) = &-\mathrm{i}kw_xw_y\ \left(\frac{z-z_s}{|\boldsymbol{r}-\boldsymbol{r}_s|}+\frac{z_s-z_f}{|\boldsymbol{r}_s-\boldsymbol{r}_f|}\right)\ G(\boldsymbol{r},\boldsymbol{r}_s)\ G(\boldsymbol{r}_s,\boldsymbol{r}_f) \\ &\times\operatorname{sinc}\left(\frac{kw_x}{2}\left(\frac{\boldsymbol{r}-\boldsymbol{r}_s}{|\boldsymbol{r}-\boldsymbol{r}_s|}-\frac{\boldsymbol{r}_s-\boldsymbol{r}_f}{|\boldsymbol{r}_s-\boldsymbol{r}_f|}\right)\cdot\hat{\boldsymbol{x}}\right) \\ &\times\operatorname{sinc}\left(\frac{kw_y}{2}\left(\frac{\boldsymbol{r}-\boldsymbol{r}_s}{|\boldsymbol{r}-\boldsymbol{r}_s|}-\frac{\boldsymbol{r}_s-\boldsymbol{r}_f}{|\boldsymbol{r}_s-\boldsymbol{r}_f|}\right)\cdot\hat{\boldsymbol{y}}\right), \end{aligned} \tag{B.17}$$

which is the familiar sinc diffraction pattern for rectangular slits.

Appendix C

Slice-to-slice map

The surface term of the formal solution of the Helmholtz equation is used to find the slice-to-slice map as follows. Consider the double-slit setup shown in Fig. 3.2 with only source S_1 switched on. The Helmholtz equation for the field within this boundary is

$$\left(\nabla^2 + k^2\right) E(\boldsymbol{r}) = \delta^3(\boldsymbol{r} - \boldsymbol{r}_{S_1}). \tag{C.1}$$

As the slits are far from the source, the surface term of the formal solution of the Helmholtz equation can be dropped and the field on the plane $z = z_1$ is approximately $G(\boldsymbol{r}, \boldsymbol{r}_{S_1})$ (discussed in the main text in Eq. (3.7)) where $\boldsymbol{r} \cdot z = z_1$, i.e., the field is projected on this plane and hence is a slice of the 3D solution.

The field at another plane, say $z = z_2$ can be calculated from the slice at z_1. For this, consider a semi-infinite volume enclosed by the planes $z = z_1$, $z \to \infty$, $x \to -\infty$, $x \to \infty$, $y \to -\infty$ and $y \to \infty$. This volume includes the double-slit, the source is now excluded, leading to a homogeneous Helmholtz equation within the volume, albeit with complications due to the presence of the slits, whose opaque parts will have some dielectric constant other than one. Because of this the Green's function, say $\tilde{G}(\boldsymbol{r}, \boldsymbol{r}')$ is no longer the free-space Green's function, near the slit plane.

However, this approach yields the slice-to-slice map directly, as the solution at any point within the volume will have contribution only from the slice at z_1 because

the other surfaces are at infinity. Therefore if one defines a propagator

$$\mathcal{P}(\boldsymbol{r},\boldsymbol{r}') \coloneqq \hat{\boldsymbol{z}} \cdot \left(E(\boldsymbol{r}')\nabla'\tilde{G}(\boldsymbol{r},\boldsymbol{r}') - \tilde{G}(\boldsymbol{r},\boldsymbol{r}')\nabla' E(\boldsymbol{r}') \right), \tag{C.2}$$

the field within the volume can be calculated from the slice at z_1 as

$$E(\boldsymbol{r}) = \iint\limits_{z=z_1} \mathrm{d}^2\boldsymbol{r}' \; \mathcal{P}(\boldsymbol{r},\boldsymbol{r}') \; E(\boldsymbol{r}'), \tag{C.3}$$

where the integration is over the plane $z = z_1$. Finally, the slice at z_2 is the projection of the field on the plane $z = z_2$, i.e., $E(\boldsymbol{r})|_{z_2}$.

The basis constructed using Haar scaling functions and the wavelet functions form a discrete orthonormal basis for the slices. This facilitates a matrix representation of the propagator that maps one slice to another. For example, the matrix representation of the free slice-to-slice propagator $\mathcal{P}(\boldsymbol{r}_\perp, \boldsymbol{r}'_\perp; z, z')$ in the new basis is

$$\mathcal{P}_{ij}(z_2, z_1) = \iint \mathrm{d}^2\boldsymbol{r}_\perp \iint \mathrm{d}^2\boldsymbol{r}'_\perp \; g_i(\boldsymbol{r}_\perp; z_2) \; \mathcal{P}(\boldsymbol{r}_\perp, \boldsymbol{r}'_\perp; z_2, z_1) \; g_j(\boldsymbol{r}'_\perp; z_1), \tag{C.4}$$

where $g_i(\boldsymbol{r}; z)$ is a basis function on slice at z and $g_j(\boldsymbol{r}'; z')$ is that on slice at z'. Note that the basis is infinite-dimensional and therefore so is the matrix representation of the free propagator.

Appendix D

Effective signals recorded by the oscilloscope

D.1 Generated signals

Mathematical expressions of the signals generated using an AWG are

$$E_1(t) = A_1 \, \mathrm{e}^{-\frac{1}{2}\frac{t^2}{\sigma^2}} \, \sin(2\pi f t)\,, \tag{D.1a}$$

$$E_2(t;\tau,\phi) = A_2 \, \mathrm{e}^{-\frac{1}{2}\frac{(t-\tau)^2}{\sigma^2}} \, \sin(2\pi f t + \phi)\,. \tag{D.1b}$$

$A_1 = 0.05$ V $= A_2$ are the peaks of the Gaussian envelopes of the two signals. Both signals have identical envelopes with $\sigma = 0.001$ s, and the sinusoidal wave has a frequency $f = 1$ KHz.

D.2 Effective input signals

The frequency range in which the power-splitter has a splitting ratio of 50:50 is well beyond the maximum frequency that the AWG can produce. So, the effective input is generated by up-converting the frequency of the input signal by using a frequency mixer. The frequency of the local oscillator SG signal used for the mixing is $f_L = 1161$ MHz. The up-converted signals, which are used as the input to the

power-splitter, take the form

$$S_1(t) = A_L\ A_1\ \mathrm{e}^{-\frac{1}{2}\frac{t^2}{\sigma^2}}\ \sin(2\pi f t)\ \ \sin(2\pi f_L t + \phi_L)\,, \tag{D.2a}$$

$$S_2(t;\tau,\phi) = A_L\ A_2\ \mathrm{e}^{-\frac{1}{2}\frac{(t-\tau)^2}{\sigma^2}}\ \sin(2\pi f t + \phi)\ \ \sin(2\pi f_L t + \phi_L)\,, \tag{D.2b}$$

where A_L is the amplitude of the signal from the local oscillator and ϕ_L is its phase relative to $V_1(t)$. A 4-port power-divider PD is used to branch the SG signal into 4 channels, two of which are used to up-convert the input signals, and the other two are used to down-convert the output of the power splitter.

D.3 Action of the power-splitter

The power-splitter transforms the effective input signals by the beam-splitter operation. The output signals are

$$S_1'(t;\tau,\phi) = \frac{S_1(t) + S_2(t;\tau,\phi)}{\sqrt{2}}, \tag{D.3a}$$

$$S_2'(t;\tau,\phi) = \frac{S_1(t) - S_2(t;\tau,\phi)}{\sqrt{2}}, \tag{D.3b}$$

where the output signals have frequencies beyond the sensitivity of the oscilloscope, and therefore need to be down-converted.

D.4 Down-conversion of the output signals

The measurement device used is an oscilloscope, two of whose channels are used to measure the two outputs of the power-splitter. However, the oscilloscope has an upper limit to the frequencies that it can measure and therefore, the high frequency output of the power-splitter is down-converted using the SG. After down-conversion

$$E_+(t;\tau,\phi) = A_L\ \sin(2\pi f_L t + \phi_L)\,\frac{S_1(t) + S_2(t;\tau,\phi)}{\sqrt{2}}, \tag{D.4a}$$

$$E_-(t;\tau,\phi) = A_L \ \sin\left(2\pi f_L t + \phi_L\right) \frac{S_1(t) - S_2(t;\tau,\phi)}{\sqrt{2}}, \tag{D.4b}$$

which implies

$$E_+(t;\tau,\phi) = A_L^2 \ \sin^2\left(2\pi f_L t + \phi_L\right) \frac{E_1(t) + E_2(t;\tau,\phi)}{\sqrt{2}}, \tag{D.5a}$$

$$E_-(t;\tau,\phi) = A_L^2 \ \sin^2\left(2\pi f_L t + \phi_L\right) \frac{E_1(t) - E_2(t;\tau,\phi)}{\sqrt{2}}, \tag{D.5b}$$

In general

$$\begin{aligned}\sin^2\left(2\pi f_L t + \phi_L\right) \ \sin\left(2\pi f t + \phi\right) = \frac{1}{2}\sin\left(2\pi f_L t + \phi_L\right)\{&\cos\left(2\pi f_L t - 2\pi f t + \phi_L - \phi\right) \\ &- \cos\left(2\pi f_L t + 2\pi f t + \phi_L + \phi\right)\} \qquad \text{(D.6)} \\ = \frac{1}{4}&\sin\left(4\pi f_L t - 2\pi f t + 2\phi_L - \phi\right) \\ +\frac{1}{4}&\sin\left(2\pi f t + \phi\right) \\ -\frac{1}{4}&\sin\left(4\pi f_L t + 2\pi f t + 2\phi_L + \phi\right) \\ -\frac{1}{4}&\sin\left(-2\pi f t - \phi\right) \qquad \text{(D.7)}\end{aligned}$$

which means that the down-converted signal has very high frequency signals along with the signals that have the frequency of the input signals which we need to filter. Now since the oscilloscope has an upper limit to the frequency that it can measure, it acts as a low-pass filter and measures only the low frequency components, making the effective output

$$E_+(t;\tau,\phi) = \frac{A_L^2}{2}\frac{E_1(t) + E_2(t;\tau,\phi)}{\sqrt{2}}, \tag{D.8a}$$

$$E_-(t;\tau,\phi) = \frac{A_L^2}{2}\frac{E_1(t) - E_2(t;\tau,\phi)}{\sqrt{2}}, \tag{D.8b}$$

and therefore, the oscilloscope only records the signal with the carrier frequency equal to that of the input pulses, giving us an effective beam splitter transformation on the inputs.

Appendix E

Sources of error for HOM experiment

Using the quantum description, the coincidence probability at the output of a (lossless) beam splitter is given by the well known result by Hong-Ou-Mandel,

$$C(\delta\tau) = |T|^4 + |R|^4 - 2\,|T|^2\,|R|^2 \int \mathrm{d}\tau\ \mathrm{Re}\{g(\tau+\delta\tau)g^*(\tau-\delta\tau)\}, \tag{E.1}$$

where, $g(\tau)$ is the fourier transform of $f(\omega)$; $f(\omega)$ is the normalized joint spectral amplitude (JSA) of the two input photons, ω being the difference in the frequency components of the two photons ($\omega = (\omega_2 - \omega_1)/2$). The time delay between the two input photons to the beam splitter is $\delta\tau$. If the two photons are completely indistinguishable, then a balanced beam splitter causes the coincidence probability to drop to zero, i.e, $C(0) = 0$. $C(\delta\tau) = 1/2$ for $\delta\tau \gg \tau_c$, where τ_c is the coherence time of the single photons.

In practice, however, different components may introduce some distinguishability in different degrees of freedom (frequency, polarization, spatial mode, etc.) of the two input photons. Let η be the probability that the input photons retain indistinguishability and ζ the probability both photons fall on the same port of the

beam splitter. Then

$$C(\delta\tau) = (1-\zeta)\left[|T|^4 + |R|^4 - 2|T|^2|R|^2\eta \int \mathrm{d}\tau\ \mathrm{Re}\{g(\tau+\delta\tau)g^*(\tau-\delta\tau)\}\right] + 2\zeta|T|^2|R|^2 \tag{E.2}$$

which is the expression used to fit the coincidence probability curve to the experimental data.

E.1 Theoretical estimate for HOM profile for the quantum experiment

We have plotted coincidence counts vs time delay, taking into account various instrumental errors (Eq. (E.2)). The dominant contributions to these errors are from the non-ideal extinction ratio of the polarizing beam splitter (PBS), imperfect rotation of the half-waveplates and the effect of the interference filter. Ideal PBS transmits only horizontally ($|H\rangle$) polarized light and reflects vertically ($|V\rangle$) polarized light. But in practice this may not happen owing to the imperfect extinction ratios. Similarly, errors in the half-waveplate rotation may introduce distinguishability in polarization. The transmittance of the band-pass filter affects the JSA of the input photons.

The values of these error parameters were obtained from the datasheets of the respective instruments. The PBS has extinction ratios 1000:1 in transmission arm and, 52:1 in the reflection arm. So, $T_H/T_V = 1000$ and $R_V/R_H = 52$, where T_H, R_H represents transmission and reflection probabilities of $|H\rangle$ polarized light through the PBS. T_V and R_V are the transmission and reflection probabilities of $|V\rangle$ polarized light. Probability of both $|H\rangle$ and $|V\rangle$ photons being in any one of the output arm of the PBS (ζ in Eq. (E.2)) is

$$\zeta = T_H T_V + R_H R_V = 0.0201. \tag{E.3}$$

The transmission and reflection coefficients of the fiber beam splitter (FBS) are

$|T|^2 = 0.52, |R|^2 = 0.48$. The Half-waveplate (HWP) rotation should be such that the angle (θ) of the HWP axis w.r.t. the horizontal axis is 45°; in order to make both the photons possess the same polarization. But the HWP rotation has an error of $\pm 1°$, leading to

$$\eta = \sin^2 2\theta = 0.9988. \tag{E.4}$$

The transmission-vs-frequency data $F(\omega)$ for the filter is provided by the manufacturer. With the filter, the joint-spectral-amplitude of the two input photons becomes

$$f(\omega) = F(\omega)\phi(\omega), \tag{E.5}$$

where $\phi(\omega)$ is the joint-spectral-amplitude of the photons without the filter. We have assumed $\phi(\omega)$ to be a Gaussian distribution with standard deviation σ.

In order to compare with the experimental data, we have multiplied a scaling factor (K) to the coincidence probability $C(\delta\tau)$ (coincidence counts=$K \times C(\delta\tau)$). We put values to all relevant parameters, i.e. η, ζ, T, R and fit the function $K \times C(\delta\tau)$ with the experimental data, while taking only K, σ as fit parameters. We get a fit (shown as "Theory" in Fig. 5 in main text) with R-squared 0.9998 for $\sigma = 0.59$ nm, $K = 2301$, resulting in an expected TPCVD of 97.56%.

E.2 Finding a fit to the experimental result

Although the major systematic errors have been taken into account above, there are additional errors that are untraceable, like dispersion and rotation of polarization as the photon passes through different fibres and components, spatial mode mismatch in the two fiber inputs of the FBS, etc. Consequently, the experimental result has a slight deviation from the theoretical estimate. To get a better fit to the data, we use the expression $K \times C(\delta\tau)$ (see Eq. (E.2)) to find a fit with η, ζ, K, σ as fit-parameters.

The "Fit" line in Fig. 5 is a result of such a fit. The best fit, with R-squared 0.9998 was achieved for $\sigma = 0.581$ nm, $K = 2303$, $\zeta = 0.038$, $\eta = 0.9995$, resulting

in a TPCVD of 96.06%.

Appendix F

Confidence intervals for photon counts using bootstrap

The result of the experiment is a graph of coincidence-counts vs actuator-position (which is proportional to the time delay between the input photons). 100 iterations of the experiment were done, which resulted in a sample of 100 values of the coincidence counts for each actuator-position. Consider the sample of coincidence counts $X = \{c_1, c_2, \cdots, c_{100}\}$ at a particular actuator position, say, l. The estimate of the counts is then the mean over X which is the sample mean, i.e., $\bar{c}$. The confidence interval for $\bar{c}$ was then found by employing a statistical bootstrap. The method involves creating a large number of sets by resampling-with-replacement from the original set. The size of the resampled set is the same as that of the original. Let one such resampled set be X^* and its mean $\bar{c}^*$. We define a quantity

$$\delta = \bar{c}^* - \bar{c}. \tag{F.1}$$

Repeating the above step a large number of times, in our case 10,000, we get a sample for δ. To find a 95 percentile confidence interval, we pick the 2.5^{th} and the 97.5^{th} percentile of this sample, $\delta_{0.025}$ and $\delta_{0.975}$. The confidence interval for $\bar{c}$ is then simply, $[\delta_{0.025} + \bar{c}, \delta_{0.975} + \bar{c}]$. We then repeat the bootstrap method for all values of the actuator-positions. These confidence intervals were plotted as the error bars for

the mean value at each actuator position.

Appendix G

The cross-correlation of outputs in a beam splitter

In semi-classical theory of photo-detection [37, 36, 38], the probability of coincident photo-detections is proportional to the intensity-intensity cross-correlation of the outputs, a normalized version of which is

$$C(\tau) := \frac{\int \mathrm{d}\varphi \; p\,(\varphi) \int_{T_{\mathrm{on}}}^{T_{\mathrm{off}}} \mathrm{d}t \, |E_+(t;\tau,\varphi)|^2 \int_{T_{\mathrm{on}}}^{T_{\mathrm{off}}} \mathrm{d}t' \, |E_-(t';\tau,\varphi)|^2}{\left[\int \mathrm{d}\varphi \; p\,(\varphi) \int_{T_{\mathrm{on}}}^{T_{\mathrm{off}}} \mathrm{d}t \, |E_+(t;\tau,\varphi)|^2\right] \left[\int \mathrm{d}\varphi' \; p\,(\varphi') \int_{T_{\mathrm{on}}}^{T_{\mathrm{off}}} \mathrm{d}t \, |E_-(t;\tau,\varphi')|^2\right]}, \quad \text{(G.1)}$$

where E_+ and E_- are the output pulses when the input pulses have a time delay τ between them and a relative phase φ. The phase φ fluctuates with a probability distribution $p(\varphi)$ and, T_{on} and T_{off} are detector on and off times respectively. The delay τ plays the role of a distinguishability parameter between the two input pulses. The cross-correlation is a measure of the fourth-order interference between the two outputs. For a 50:50 beam splitter, $C(\tau)$ shows a variation dependent on the shape of the pulse. If the probability distribution $p(\varphi)$ is uniform over the interval $[0, 2\pi)$, i.e.,

$$p(\varphi) = \frac{1}{2\pi}, \quad \text{(G.2)}$$

the curve shows a visibility of 0.5. A detailed analysis of this cross-correlation with classical pulses is discussed in [41].

If the distinguishability parameter is the angle of polarization θ between the two input pulses instead of time-delay τ, the cross-correlation of the intensities can be redefined as in Eq. 5.2, where the time-delay between the input pulses is zero. For a 50:50 beam splitter, $C(\theta)$ shows a sinusoidal variation as shown in Fig. 5.2, for uniformly randomized phase as in Eq. (G.2).

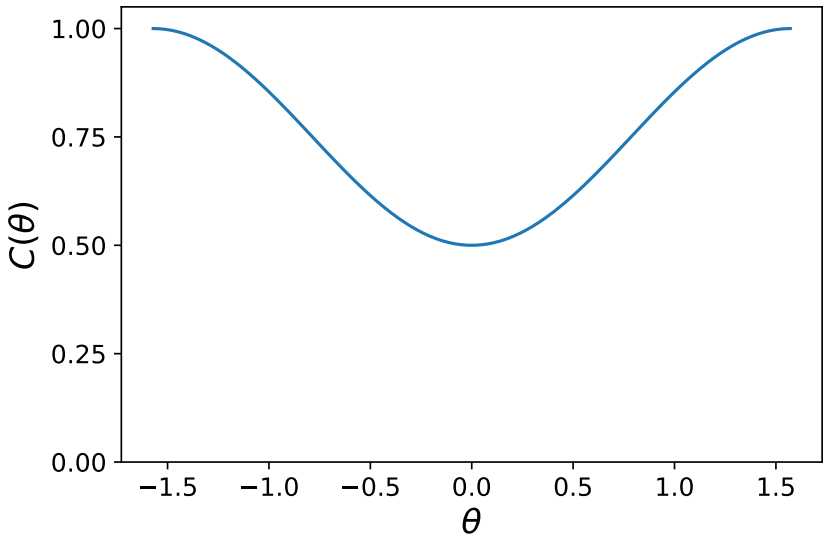

Figure G.1: The cross-correlation function plotted as a function of the relative polarization angle θ, which is the distinguishability parameter. The correlation is minimum when both the sources are indistinguishable, i.e., $\theta = 0$, and maximum when they are completely distinguishable, i.e., $\theta = \pi/2$. The plot has been generated using Eq. (5.2) for a regular cubic 50:50 beam splitter with two identical input pulses having zero delay between them. When the distinguishability parameter is θ the shape of the pulses does not affect the correlation.

The equation that fits the data in the plot of Fig. 5.2 is

$$C_{\text{fit}}(\theta) = 0.75 - 0.25\cos 2\theta, \tag{G.3}$$

which has a visibility of 0.5.

As $C(\tau)$ and $C(\theta)$ are dependent on the probability distribution of the phase φ, the visibility of the curves can exceed 0.5, with an appropriate choice of the probability distribution. For some distribution, the visibility can reach 1, classically

[41]. The variation of the correlation as a function of the distinguishability parameter is used as a signature of a beam splitter, which the double-slit setup, as is discussed in this work, also exhibits.

Appendix H

The implementation of the phase shifter in MZI

The phase shifter in the double-slit MZI is modelled as a medium of thickness t and with refractive index n. Within the medium the Green's function (and hence the propagator) will change to

$$G(\boldsymbol{r}, \boldsymbol{r}'; n) = -\frac{1}{4\pi} \frac{\mathrm{e}^{\mathrm{i}nk|\boldsymbol{r}-\boldsymbol{r}'|}}{|\boldsymbol{r}-\boldsymbol{r}'|}, \tag{H.1}$$

where the refractive index of the medium causes a change in the propagation constant resulting in bending of light and a change in the phase. The thickness of the medium is small enough that the effect can be approximated by an extra phase

$$\alpha = \frac{2\pi}{\lambda}(n-1)t, \tag{H.2}$$

imparted to the field and the net effect is captured by simply multiplying the output at port D_2 by $\mathrm{e}^{\mathrm{i}\alpha}$.

Bibliography

[1] E. Knill, R. Laflamme, and G. J. Milburn. A scheme for efficient quantum computation with linear optics. *Nature*, 409(6816):46–52, 2001.

[2] P. Kok, W. J. Munro, K. Nemoto, T. C. Ralph, J. P. Dowling, and G. J. Milburn. Linear optical quantum computing with photonic qubits. *Rev. Mod. Phys.*, 79:135–174, Jan 2007.

[3] M. Genovese and P. Traina. Review on qudits production and their application to quantum communication and studies on local realism. *Adv. Sci. Lett.*, 1(2):153–160, 2008.

[4] L. Neves, G. Lima, J. G. Aguirre Gómez, C. H. Monken, C. Saavedra, and S. Pádua. Two-photon high-dimensional spatial entanglement: Theory and experiment. *Mod. Phys. Lett. B*, 20(01):1–23, 2006.

[5] B. E. A. Saleh, M. C. Teich, and B. E. Saleh. *Fundamentals of Photonics*, volume 22. Wiley, New York, NY, 1991.

[6] Christopher G. *Introductory Quantum Optics*. Cambridge University Press, Cambridge, 2004.

[7] J. C. García-Escartín and P. Chamorro-Posada. Universal quantum computation with the orbital angular momentum of a single photon. *J. Opt.*, 13(6):064022, apr 2011.

[8] A. Mair, A. Vaziri, G. Weihs, and A. Zeilinger. Entanglement of the orbital angular momentum states of photons. *Nature*, 412(6844):313–316, 2001.

[9] G. Molina-Terriza, J. P. Torres, and L. Torner. Twisted photons. *Nat. Phys.*, 3:305 EP –, 05 2007.

[10] G. F. Calvo, A. Picón, and A. Bramon. Measuring two-photon orbital angular momentum entanglement. *Phys. Rev. A*, 75:012319, Jan 2007.

[11] M. Malik, M. O'Sullivan, B. Rodenburg, M. Mirhosseini, J. Leach, Martin P. J. L., Miles J. P., and R. W. Boyd. Influence of atmospheric turbulence on optical communications using orbital angular momentum for encoding. *Opt. Express*, 20(12):13195–13200, Jun 2012.

[12] Z. Xiao, R. N. Lanning, M. Zhang, I. Novikova, E. E. Mikhailov, and J. P. Dowling. Why a hole is like a beam splitter: A general diffraction theory for multimode quantum states of light. *Phys. Rev. A*, 96:023829, Aug 2017.

[13] D. Ghosh, T. Jennewein, P. Kolenderski, and U. Sinha. Spatially correlated photonic qutrit pairs using pump beam modulation technique. *OSA Contin.*, 1(3):996–1011, Nov 2018.

[14] G. P. Thomson and A. Reid. Diffraction of cathode rays by a thin film. *Nature*, 119(3007):890–890, 1927.

[15] C. Davisson and L. H. Germer. Diffraction of electrons by a crystal of nickel. *Phys. Rev.*, 30:705–740, Dec 1927.

[16] H. Rauch, W. Treimer, and U. Bonse. Test of a single crystal neutron interferometer. *Phys. Lett. A*, 47(5):369 – 371, 1974.

[17] H. Rauch and S. A. Werner. *Neutron Interferometry: Lessons in Experimental Quantum Mechanics, Wave-particle Duality, and Entanglement; 2nd ed.* Oxford University Press, Oxford, 2015.

[18] D. W. Keith, M. L. Schattenburg, Henry I. Smith, and D. E. Pritchard. Diffraction of atoms by a transmission grating. *Phys. Rev. Lett.*, 61:1580–1583, Oct 1988.

[19] D. W. Keith, C. R. Ekstrom, Q. A. Turchette, and D. E. Pritchard. An interferometer for atoms. *Phys. Rev. Lett.*, 66:2693–2696, May 1991.

[20] I. Dhand, A. Khalid, H. Lu, and B. C. Sanders. Accurate and precise characterization of linear optical interferometers. *J. Opt.*, 18(3):035204, feb 2016.

[21] C. K. Hong, Z. Y. Ou, and L. Mandel. Measurement of subpicosecond time intervals between two photons by interference. *Phys. Rev. Lett.*, 59:2044–2046, Nov 1987.

[22] M. Born and E. Wolf. *Principles of Optics: Electromagnetic Theory of Propagation, Interference and Diffraction of Light; 6th ed.* Pergamon, Oxford, 1980.

[23] J. D. Jackson. *Classical Electrodynamics*. Wiley, New York, NY, 3rd ed. edition, 1999.

[24] B. Hall. *Lie Groups, Lie Algebras, and Representations: An Elementary Introduction; 2nd ed.* Graduate texts in mathematics. Springer, Cham, 2015.

[25] N. Y. Vilenkin. Special functions and the theory of group representations, ams translations of math. *Mo, ogr*, 22, 1968.

[26] W. Miller. *Lie Theory and Special Functions*. Math. Sci. Eng. Academic Press, New York, NY, 1968.

[27] J. D. Talman. *Special Functions: A Group Theoretic Approach*. Mathematical physics monograph series. Benjamin, New York, NY, 1968.

[28] M. Reck, A. Zeilinger, H. J. Bernstein, and P. Bertani. Experimental realization of any discrete unitary operator. *Phys. Rev. Lett.*, 73(1):58, 1994.

[29] A. Bouland and S. Aaronson. Generation of universal linear optics by any beam splitter. *Phys. Rev. A*, 89:062316, Jun 2014.

[30] P. Hariharan. *Basics of Interferometry*. Academic Press, San Diego, CA, 1992.

[31] G. B. Arfken and H.-J. Weber. Mathematical methods for physicists. 1972.

[32] G. Kaiser. *A Friendly Guide to Wavelets.* Modern Birkhäuser Classics. Springer, Boston, 2011.

[33] S. G. Mallat and G. Peyré. *A Wavelet Tour of Signal Processing: The Sparse Way ; 3rd ed.* Elsevier, Burlington, MA, 2009.

[34] A. Haar. Zur theorie der orthogonalen funktionensysteme. *Mathematische Annalen*, 69(3):331–371, Sep 1910.

[35] R. Loudon. *The Quantum Theory of Light; 3rd ed.* Oxford Univ. Press, Oxford, 2002.

[36] L. Mandel, E. C. G. Sudarshan, and E. Wolf. Theory of photoelectric detection of light fluctuations. *Proc. Phys. Soc.*, 84(3):435, 1964.

[37] L. Mandel. Fluctuations of photon beams and their correlations. *Proc. Phys. Soc.*, 72(6):1037, 1958.

[38] Leonard Mandel and Emil Wolf. *Optical Coherence and Quantum Optics.* Cambridge Univ., Cambridge, 1995.

[39] S. Sadana, B. C. Sanders, and U. Sinha. Double-slit interferometry as a lossy beam splitter. *arXiv preprint arXiv:1906.07450*, 2019.

[40] G. Strang. *Linear Algebra and Its Applications.* Thomson, Brooks/Cole, 2006.

[41] S. Sadana, D. Ghosh, K. Joarder, A. N. Lakshmi, B. C. Sanders, and U. Sinha. Near-100% two-photon-like coincidence-visibility dip with classical light and the role of complementarity. *Phy. Rev. A*, 100(1):013839, 2019.

[42] O. Gobert, P. M. Paul, J. F. Hergott, O. Tcherbakoff, F. Lepetit, P. D 'Oliveira, F. Viala, and M. Comte. Carrier-envelope phase control using linear electro-optic effect. *Opt. Express*, 19(6):5410–5418, Mar 2011.

[43] C. Feng, J. F. Hergott, P. M. Paul, X. Chen, O. Tcherbakoff, M. Comte, O. Gobert, M. Reduzzi, F. Calegari, C. Manzoni, M. Nisoli, and G. Sansone. Complete

analog control of the carrier-envelope-phase of a high-power laser amplifier. *Opt. Express*, 21(21):25248–25256, Oct 2013.

[44] J.-F. Hergott, O. Tcherbakoff, P.-M. Paul, Ph. Demengeot, M. Perdrix, F. Lepetit, D. Garzella, D. Guillaumet, M. Comte, P. D'Oliveira, et al. Carrier-envelope phase stabilization of a 20 w, grating based, chirped-pulse amplified laser, using electro-optic effect in a linbo 3 crystal.

[45] D. M. Pozar. *Microwave engineering*. John Wiley & Sons, 2009.

[46] F. M. Dekking, C. Kraaikamp, H. P. Lopuhaä, and L. E. Meester. *A Modern Introduction to Probability and Statistics: Understanding why and how*. Springer Science & Business Media, 2005.

[47] M. H. Rubin, D. N. Klyshko, Y. H. Shih, and A. V. Sergienko. Theory of two-photon entanglement in type-ii optical parametric down-conversion. *Phys. Rev. A*, 50:5122–5133, Dec 1994.

[48] P. G. Kwiat, A. M. Steinberg, and R. Y. Chiao. Observation of a "quantum eraser": A revival of coherence in a two-photon interference experiment. *Phys. Rev. A*, 45:7729–7739, Jun 1992.

[49] D. N. Klyshko. Quantum optics: quantum, classical, and metaphysical aspects. *Physics-Uspekhi*, 37(11):1097–1122, nov 1994.

[50] D. N. Klyshko. Observable signs of nonclassical light. *Physics Letters A*, 213(1):7 – 15, 1996.

[51] W. E. Lamb. Anti-photon. *Applied Physics B*, 60(2):77–84, Feb 1995.